

**High Resolution Transmission
Electron Microscopy Investigations of
FePt and *Au* Nanoparticles**

Diploma Thesis

of

Dmitry Tyutyunnikov

at the Department of Physics

University Duisburg-Essen

August, 2010

Contents

Kurzfassung	1
Abstract	3
1 Introduction	5
2 Basics	7
2.1 The principal setup of TEM	7
2.2 HRTEM Imaging	10
2.3 Improvement of resolution by aberration correction	21
2.4 Image simulations	27
3 Experimental Techniques	31
3.1 Preparation of the samples	31
3.2 Microscopes	34
3.3 Exit Wave Reconstruction (EWR)	35
3.3.1 Acquisition of focal series in TEM	35
3.3.2 EWR by using TrueImage	37
3.3.3 Peaks Determination	42
3.4 Image simulations	44
3.4.1 Modeling of nanoparticles	44
3.4.2 QSTEM software	44
4 Analysis of surface relaxation in $Fe_{45}Pt_{55}$ nanoparticles	47
4.1 Reconstruction of amplitude and phase from focal-series	47
4.2 Determination of positions of atomic columns	51
4.3 Calculation of interplane distances and estimation of errors	52

4.4	Results and Discussions	54
5	Clarification of the structure of $Fe_{45}Pt_{55}$ nanoparticles on the base of simulations	63
5.1	Building of the model	63
5.2	Simulations of the phase image	65
5.3	Results and discussions	66
6	Analysis of morphology and structure of gold nanoparticles	75
6.1	Analysis of HRTEM and phase images of gold nanoparticles	75
6.2	Tilting experiments with gold nanoparticles	83
6.3	Dynamical structural transformations of gold nanoparticles under electron beam	86
7	Conclusion	91
A	Appendix	95
A.1	Generator - software	95
A.2	cfg - format	99
A.3	Microscope Titan 80-300 TEM	99
A.4	Microscope Tecnai F20 Supertwin	100
	Bibliography	103
	Acknowledgements	109

Kurzfassung

Die Struktur der chemisch ungeordneten $Fe_{45}Pt_{55}$ und auch katalytischen Au Nanopartikel wurde mit Hilfe der hochaufgelösten Transmissionselektronenmikroskopie (High Resolution Transmission Electron Microscopy, HRTEM) bestimmt. Die Strukturuntersuchungen wurden mit einem neuenartigen Mikroskop durchgeführt, das mit dem speziellen Korrektor für Objektivlinsen ausgerüstet ist. Durch dieses Bauteil ist man in der Lage sowohl die Öffnungsfehler als auch die Aberrationen der höheren Ordnungen zu korrigieren. Mit der gerätespezifischen Korrektur der restlichen Aberrationen ist es möglich die Auflösung zu verbessern und folglich die Analyse der mikroskopischen Abbildungen zu vereinfachen. Um die Auflösung zu vergrößern und die Abbildungsartefakte zu reduzieren wird die spezielle Methode der *Exit Wave Reconstruction* (EWR) [1] eingesetzt. Die Phasenabbildung der Austrittswelle wurde aus der Defokussierung rekonstruiert. Danach wurde die Phasenabbildung für die Analyse der Struktur des Kristallgitters der Nanopartikel verwendet.

Die Analyse von kleinen chemisch präparierten $FePt$ Partikeln zeigt die intrinsische Ausdehnung der Gitterkonstante bis zu 4.4% im Vergleich zum bulk $FePt$. Die Ausdehnung der äußeren Atomebenen $\{111\}$ und $\{100\}$ wegen der Oberflächenrelaxation kann bestätigt werden. Die Größe der Oberflächenrelaxation für verschiedene Atomlagen ist gleich innerhalb der Fehlergrenzen und beträgt ca. 6%. Für die Verifikation der Ergebnisse wurden Kontrastsimulationen durchgeführt. Die atomistischen Modelle der Nanopartikel wurden durch eine selbst programmierte Software erstellt. Durch dieses Programm kann man die Atomkoordinaten der Partikel verschiedener Strukturen und Morphologien generieren. Das Modell des amorphen Kohlenstofffilms wurde auch für Simulationen verwendet. Es wurde gezeigt, dass die kleinen Abweichungen der Maxima der Intensität ($\approx 2.8\%$) im Phasenbild auf den amorphen Kohlenstofffilm zurückzuführen ist. Die Simulationen wurden sowohl für ungekippte, als auch ein bisschen aus der Zonenachse gekippte Nanopar-

tikel durchgeführt. Es wurde gezeigt, dass die Kippung die chemische Empfindlichkeit (Z-Kontrast) des Phasenbildes reduziert.

Die HRTEM und die Phasenbilder der kleinen dekahedrischen Gold-Nanopartikel wurden in meiner Diplomarbeit analysiert. Die experimentellen Bilder wurden mit den simulierten verglichen. Der Vergleich zeigt, dass die dekahedrischen Gold-Nanopartikel zusätzliche $\{110\}$ Kristallflächen besitzen müssen, die senkrecht zu 5-zähligen Symmetrieachsen liegen. Das bedeutet, dass die pyramidenförmigen symmetrischen Teile des Dekaeders im Fall der Gold-Nanopartikel abgeschnitten werden müssen. Der Abschneidungsgrad wurde gleich $R = 54\%$ abgeschätzt. Eine wissenschaftliche Gruppe hat schon den gleichen Effekt für größere Nanopartikel veröffentlicht [2]. Die Ergebnisse der Kippungsexperimente zeigen für diese Nanopartikel den Wert von $R = 34\%$. Die großen Gold-Nanopartikel mit der durchschnittlichen Größe von 50 nm zeigen hauptsächlich die reguläre Gestalt. Diese Tatsache weist darauf hin, dass das Erscheinen der $\{110\}$ Kristallflächen der Größeneffekt ist.

Ich stelle auch einige Ergebnisse über das dynamische Verhalten der Gold-Nanopartikel im Elektronenstrahl des Mikroskops dar und diskutiere über mögliche Ursachen.

Abstract

The structure of chemically disordered $Fe_{45}Pt_{55}$ and also catalytic Au nanoparticles were determined by means of High Resolution Transmission Electron Microscopy (HRTEM). The structure studies were performed with the advanced microscope equipped with a special spherical aberration corrector for objective lenses. With hardware correction of residual aberrations it is possible to enhance the resolution and therefore to make the analysis of images more simple. In order to increase further the resolution and reduce imaging artifacts the special technique *Exit Wave Reconstruction* (EWR) [1] was used. Phase image of electron wave function reconstructed from focal-series was used for analysis of lattice structure of nanoparticles.

The analysis of small chemically prepared $FePt$ particles shows the overall expansion of lattice parameter up to 4.4% in comparison with bulk $FePt$. The expansion of outmost layers due to the surface relaxation of $\{111\}$ and $\{100\}$ planes is also confirmed. The value of surface relaxation is equal for different planes within error bar and amounts $\approx 6\%$. For verification of results image simulations were carried out. The atomic models of nanoparticles were built by using special software written for this work. This program allows us to generate particles of different morphologies and structures. The model of amorphous supporting carbon film was also used for simulations. It was shown that the small shift of maxima of the intensity ($\approx 2.8\%$) in the phase image can be originated from amorphous carbon. The simulations were carried out for untilted as well as slightly tilted nanoparticles out of the zone-axis. It was shown that the tilting decreases chemical sensitivity (Z-contrast) of the phase image.

HRTEM micrographs and phase image of small decahedral gold nanoparticles were analyzed in this diploma work. The experimental images were compared with simulated ones. The analysis shows that decahedral Au nanoparticles should have

additional $\{110\}$ crystallographic facets perpendicular to the five-fold symmetry axis. It means that the pyramidal symmetrical parts of the decahedrons in case of Au nanoparticles are truncated. The degree of truncation was estimated to be $R = 54\%$. One group reported the same truncation for bigger nanoparticles [2]. The results of tilting experiments gives a value of $R = 34\%$. Big gold nanoparticles with average size of 50 nm have presumably regular shape without truncation. This fact allows us to attribute the appearance of $\{110\}$ facets to a size effect.

Also some results concerning the dynamical behavior of Au nanoparticles under electron beam irradiation are shown and possible reasons are discussed in this thesis.

1 Introduction

Nowadays the nanoparticles are the center of many research effort due to their unique optical, mechanical, magnetic and also catalytic properties different from bulk material. The nanoparticles of different shapes and chemical compositions are currently used as functionable materials for their implementation on different kinds of devices. In my diploma work I investigated two different systems: *FePt* and *Au* - nanoparticles. Both systems were synthesized using wet-chemistry method which becomes more attractive and dominant in nano-industry.

Since the discovery of the first hard drive for storage of digital information the capacity of those devices have increased exponentially. In current hard drives small magnetic domains are used for storage of information units. However during the last decades scientists try to use small highly crystalline magnetic nanoparticles for the storage of information. If they succeed to arrange these nanoparticles regularly on the substrate the highest possible data density can be achieved. *FePt* nanoparticles are prominent candidate for this purpose. The magnetic properties of these nanoparticles are strongly determined by their structure. Due to the progress in aberration-corrected transmission electron microscopy nowadays it is possible to carry out structural investigations with unprecedented resolution. In order to reduce imaging artifacts by analysis of micrographs the special technique called *Exit Wave Reconstruction* was used in the current work. The *FePt* nanoparticles can have different morphologies depending on their synthetic parameters. The magnetic anisotropy strongly depends on the shape of nanoparticles. Also the observed expansion of lattice parameter and break of crystal symmetry at the surface should have big impact on magnetic properties. The close inspection of lattice structure together with image simulations was performed in this thesis.

The *Au* nanoparticles attract increasing interest due to their variety of applications. The unusual optical properties and high chemical activity made them the

model system to investigate wide-range phenomena like self-assembly, catalysis, phase transfer, crystal growth and plasmonics [3]. Recently new synthetic techniques enabled the control over the size and morphology of these nanoparticles [4]. It is even possible to create very complicated structures like icosahedral or decahedral. The optical and catalytic properties of these nanoparticles essentially depend on the shape enclosed by crystallographic facets. The reason of this dependence is the difference in surface energies for different facets. In this diploma thesis the morphological and structural studies of decahedral gold nanoparticles of different sizes were performed. The influence of electron irradiation on the sample in the microscope and in particular crystal structure is still unclear and remains a very hot topic for the microscopy community. In my diploma thesis I will present some micrographs of Au nanoparticles showing their increased chemical activity under electron beam. I will give also possible physical explanations for the observed phenomena.

2 Basics

2.1 The principal setup of TEM

All structural and morphological investigations in this work were carried out with high-resolution transmission electron microscope (HRTEM). In the following chapter principal setup of this instrument as well as main imaging modes will be explained. I'll also touch upon a subject how it's possible to enhance the resolution by correction of aberrations of lenses. A full description of TEM and different contrast mechanisms can be found in the corresponding literature ([5–8]).

Transmission Electron Microscope is a special kind of electron microscope for imaging of different objects. In contrast to other microscopes the electrons in TEM pass through and interact with atoms of the sample. Due to this interaction the electrons are being scattered. The final image is very complicated interference pattern of incident and diffracted beams. Nowadays with state-of-the-art microscopes it's possible to achieve resolution of 0.08 nm. For most powerful microscope TEAM (Transmission Electron Aberration-corrected Microscope, National Center of Electron Microscopy, Berkley Lab) this value amounts 0.05 nm.

The principal setup of TEM is similar to one of light microscope. The sample is illuminated with the light (with electrons in case of TEM). The image of the sample is then magnified by means of projection lenses and represented on a canvas (screen). However in TEM electromagnetic lenses are used in case of glass lenses to guide the electron beam through the microscope. The principal setup of TEM is illustrated on the figure 2.1. Different parts of the microscope contribute to image formation: illumination (FEG, Condensor Lenses C1 and C2), image formation due to objective lenses, projection system (projective lenses) and image acquisition (CCD).

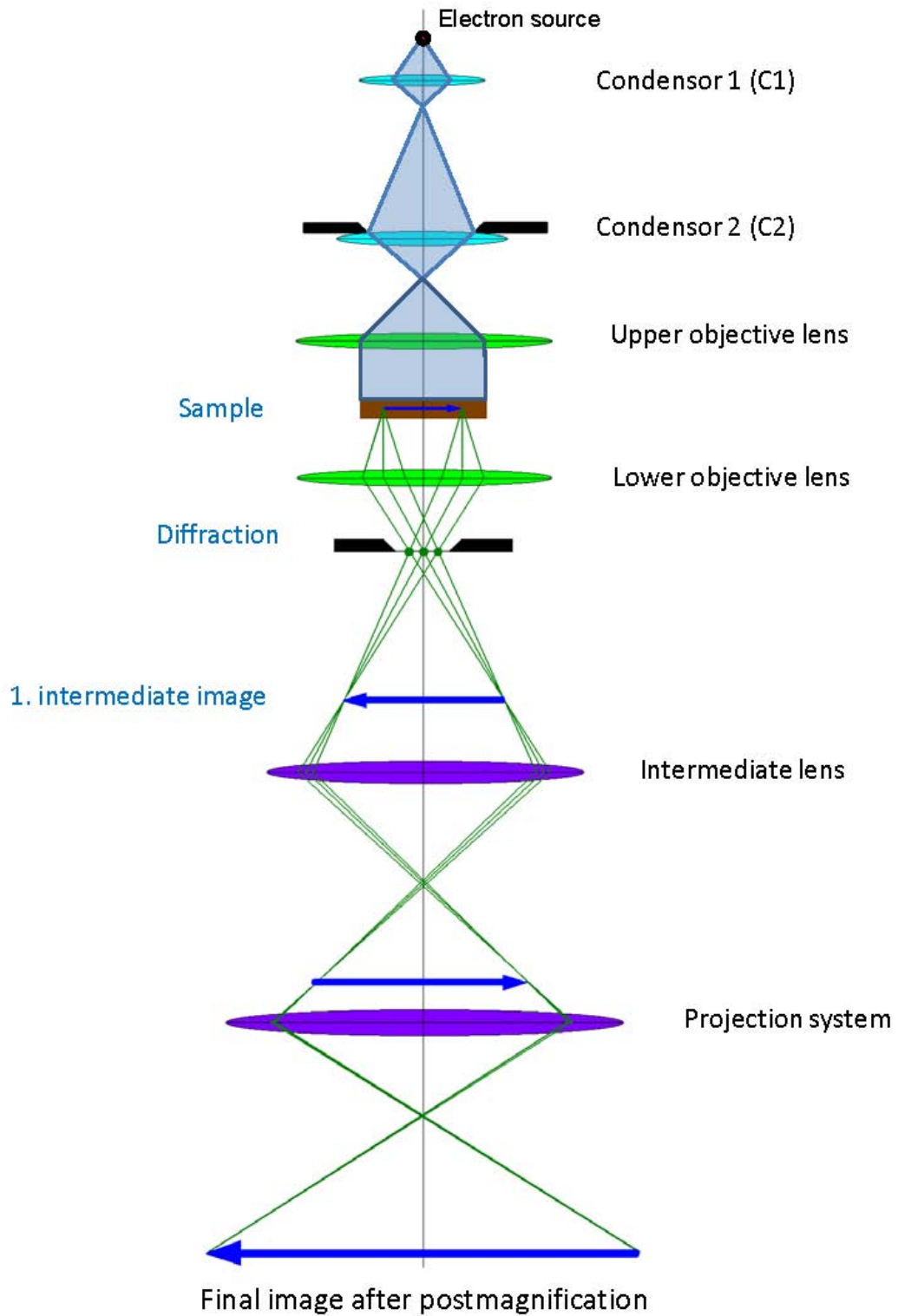


Figure 2.1: The principal setup of TEM

The illumination system is situated in the top part of the microscope and consists of an electron source and condenser lenses (C1 and C2). The illumination system takes the electrons from the source and transfers them to the sample in the form of a parallel or convergent beam. Usually the following electron sources are used: thermionic sources like LaB_6 or tungsten sources and field emission gun (FEG). All of them have some advantages and disadvantages. However nowadays modern microscopes are normally equipped with FEG, because this source produces a very bright electron beam at a low operating temperature and has a very long lifetime.

After the electron source we have a system of condenser lenses. These lenses are used in order to form the electron beam which illuminates the sample. By changing the focal distance of the condenser lenses we can create a parallel or convergent illumination. The parallel beam is usually used in traditional TEM. The convergent beam is typical for STEM mode (Scanning TEM), because one needs to illuminate every point of the sample. Here the most important parameter is the semi-convergence angle α . It also plays a very important role in image simulations.

Objective lenses of the microscope are used for image formation. After propagating through the objective lens, all electron beams from the sample are focused at the image plane. Here one uses an objective aperture in order to exclude electrons at high scattering angles. In HRTEM mode usually no objective apertures are used. The objective lenses define the quality of imaging and in that way the resolution of the microscope. The real lenses suffer from different aberrations. The most important one is spherical aberration C_s .

The projection system of the microscope consists of an intermediate lens and projection lenses. By changing the strength (i.e. the focal distance) of the intermediate lens it's possible to switch between diffraction and imaging modes. If the back focal plane of the objective lenses corresponds to the object plane of the intermediate lens we can obtain diffraction on the viewing screen. In imaging mode we readjust the intermediate lens so that its object plane is the image plane of the objective lens. The projection lenses are used for post-magnification of the image. In HRTEM the highest magnification can be 10^6 or even higher. The final image is recorded with a CCD.

2.2 HRTEM Imaging

Contrast Transfer Function

In order to describe mathematically the imaging process in TEM the contrast transfer function (CTF) is introduced. The microscope transforms each point of the specimen into some extended region. Since each point of the specimen can be different it's possible to describe it with function $f(x, y)$. Here we consider very thin sample, so the properties does not change too much in z-direction. The extended region can be described with another function $g(x, y)$. The process of contrast transfer in real space can be described by function $h(x, y)$ which is called „blurring“ or *point – spread function*. Mathematically the image formation can be expressed as convolution of functions $f(x, y)$ and $h(x, y)$:

$$g(\mathbf{r}) = \int f(\mathbf{r}')h(\mathbf{r} - \mathbf{r}')d\mathbf{r}' = f(\mathbf{r}) \otimes h(\mathbf{r}) \quad (2.1)$$

The convolution in real space is quite complicated task. In reciprocal space the convolution can be expressed by simple multiplication. According to the Fourier theorem each function can be represented as a sum of harmonic functions. The function $g(\mathbf{r})$ can be rewritten in corresponding way:

$$g(\mathbf{r}) = \sum_{\mathbf{g}} G(\mathbf{g})exp(i\mathbf{g} \cdot \mathbf{r}) \quad (2.2)$$

\mathbf{g} is two dimensional vector in reciprocal space. $|\mathbf{g}|$ is also called spatial frequency and referred to the periodicity in real space. Higher $|\mathbf{g}|$ correspond to higher spatial frequencies and smaller space distances. In any case high resolution requires high spatial frequencies. New function $G(\mathbf{g})$ is representation of $g(\mathbf{r})$ but in reciprocal space. In the same way we can define two other Fourier transforms:

$F(\mathbf{g})$ - Fourier transform of specimen function $f(\mathbf{r})$

$H(\mathbf{g})$ - Fourier transform of *point – spread function* $h(\mathbf{r})$

Real-space convolution can be replaced by simple multiplication in Fourier-space. So $G(\mathbf{g})$ can be written like this:

$$G(\mathbf{g}) = F(\mathbf{g})H(\mathbf{g}) \quad (2.3)$$

The function $H(\mathbf{g})$ shows how the contrast information is transferred through the microscope. Therefore it is called *Contrast Transfer Function*. This function is very useful for understanding of different phenomena in microscope. Following factors contribute to the CTF: apertures, envelope functions and aberration of lenses. All these phenomena can be described mathematically:

$$H(\mathbf{g}) = A(\mathbf{g})E(\mathbf{g})T(\mathbf{g}) \quad (2.4)$$

Aperture function $A(\mathbf{g})$ is equal to 1 for electrons which pass through the aperture and 0 otherwise:

$$A(\mathbf{g}) = 1, \text{ if } |g| \lambda \leq \sin(\alpha) \quad (2.5)$$

$$A(\mathbf{g}) = 0, \text{ if } |g| \lambda > \sin(\alpha) \quad (2.6)$$

The function $T(\mathbf{g})$ is called coherent transfer function and is written as:

$$T(\mathbf{g}) = \exp(-i\chi(\mathbf{g})) \quad (2.7)$$

where the argument of exponent $\chi(\mathbf{g})$ is so-called the aberration function. Considering only defocus Δf and spherical aberration C_s , it is given:

$$\chi(\mathbf{g}) = \pi\Delta f\lambda\mathbf{g} + \frac{\pi}{2}C_s\lambda^3u^4 \quad (2.8)$$

where λ - wavelength of electrons, Δf - defocus of objective lenses, C_s - coefficient of spherical aberration. On the figure 2.2 one can see deformation of wavefront and beam displacements happening upon defocusing and spherical aberration.

In general the aberration function has following form:

$$\chi(g, \phi) = \frac{2\pi}{\lambda} \sum \frac{a_{mn}}{m} (\lambda g)^m \cos[n(\phi - \phi_{mn})] \quad (2.9)$$

, where polar notation (g, ϕ) of wavevector \mathbf{g} is used, ϕ_{mn} - direction of anisotropic aberrations, a_{mn} - aberration coefficient [9]. It describes in terms of $\frac{2\pi}{\lambda}$ the phase shift of electron wave from perfect spherical wavefront caused by aberration of lenses. This general case is illustrated on figure 2.3.

More detailed information about aberrations and its correction will be described in the next chapter.

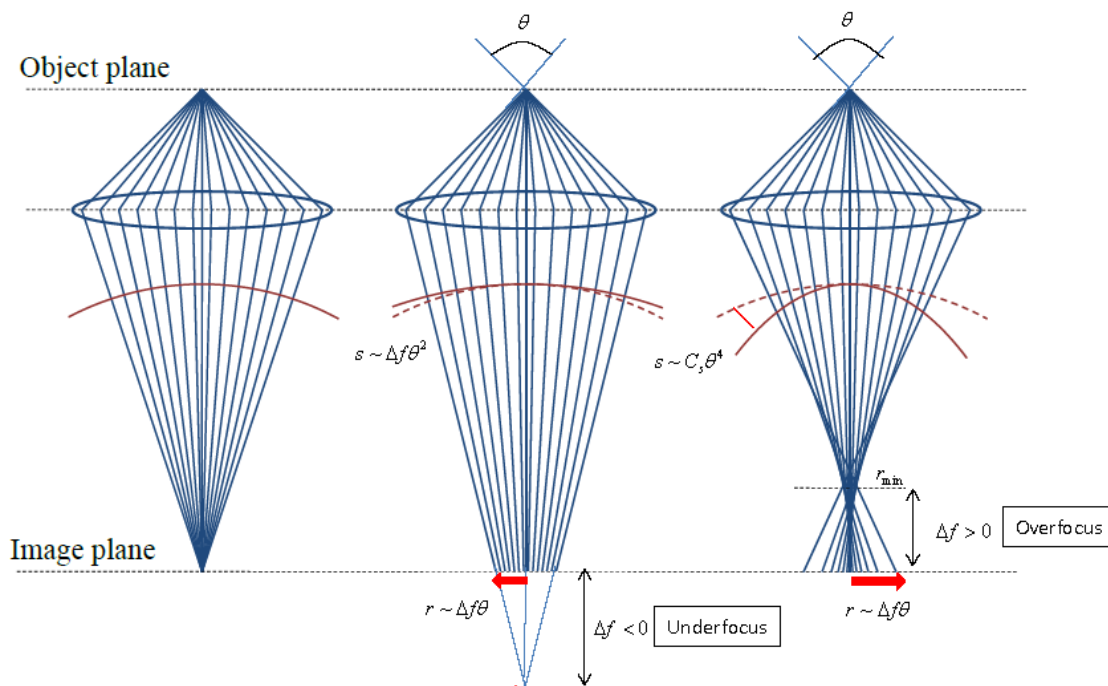


Figure 2.2: Illustration of beam displacements and deformation of wavefront by traveling of electrons through objective lens. On the left hand side the perfect case is illustrated. Electrons emitted from one point of the object are gathered at one point in image plane. By underfocusing the electrons gather under image plane. The phase shift of electrons depends from diffraction angle θ and defocus value. By spherical aberration the resulting wavefront is more strongly curved than the ideal spherical wave. The electrons paths far away from optical axis are bended stronger. The lateral image-plane displacement of beam paths is indicated by r . The focus spread caused by spherical aberration can be characterized by Gaussian distribution.

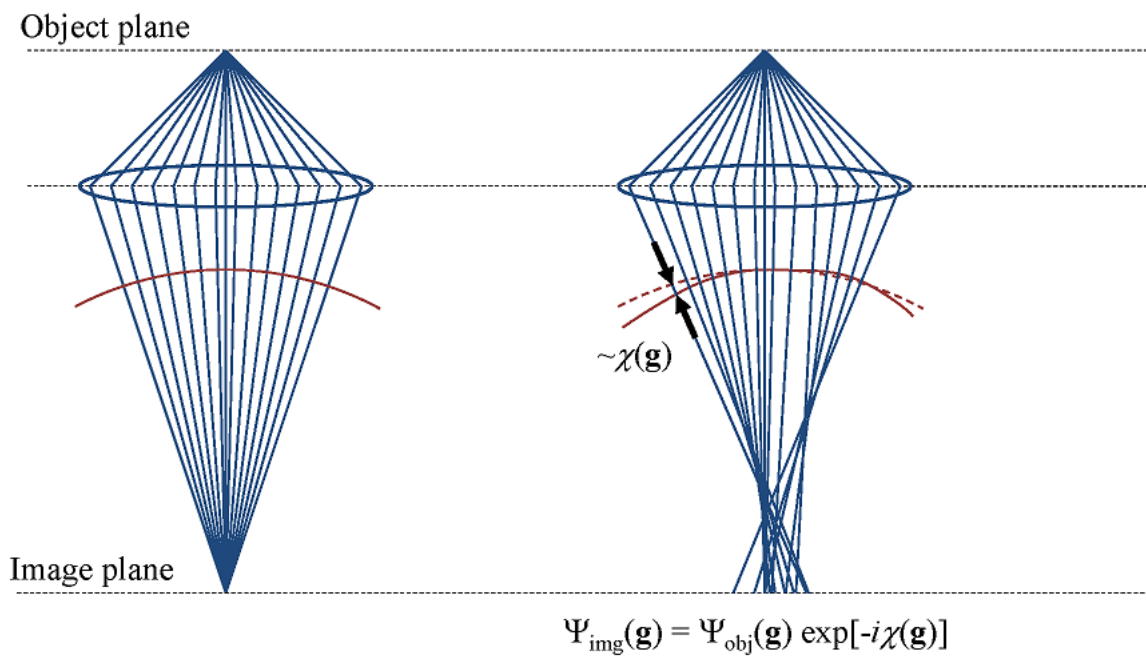


Figure 2.3: General case of aberrations of objective lenses. On the left hand side the paths of electrons in perfect lenses. On the right hand side distortion of wavefront of constant phase in comparison with perfect spherical front. The phase shift is denoted as aberration function

In TEM we very often deal with assumption which is called weak-phase-object-approximation technique (WPOA). The sense of this method is that for thin samples the phase of electron wave changes only slightly. Therefore the phase should depend linearly on the thickness of the specimen. This approximation yields for exit-wave function:

$$f(x, y) = 1 + i\sigma V_t(x, y)t \quad (2.10)$$

, where σ is the interaction constant, $V_t(x, y)$ - projected potential within specimen of thickness t . The phase change of electron wave is equal to the term $\sigma V_t(x, y)t$. Detailed derivation of this expression can be found in [5]. The projected potential is continuous along the direction of the incident beam and strongly peaked at the position of atomic columns. Accordingly the phase maxima occur at atomic column positions.

Now it's possible to rewrite equation 2.1 within WPOA:

$$\Psi(x, y) = (1 + i\sigma V_t(x, y)) \otimes h(x, y) \quad (2.11)$$

Function $h(x, y)$ can be represented as $\cos(x, y) + i\sin(x, y)$, then $\Psi(x, y)$ becomes:

$$\Psi(x, y) = 1 - \sigma V_t(x, y) \otimes \sin(x, y) + i\sigma V_t(x, y) \otimes \cos(x, y) \quad (2.12)$$

The intensity is given by:

$$I = \psi\psi^* = |\Psi|^2 \quad (2.13)$$

and multiplying this and neglecting terms in σ^2 , because it's small, one obtains following dependence:

$$I = 1 + 2\sigma V_t(x, y) \otimes \sin(x, y) \quad (2.14)$$

One can make conclusion that in WPOA only imaginary part contributes to $T(\mathbf{g})$, therefore one can use $T(\mathbf{g}) = 2\sin(\chi(\mathbf{g}))$. Now the contrast transfer function can be rewritten in these terms:

$$T(\mathbf{g}) = A(\mathbf{g})E(\mathbf{g})2\sin(\chi(g)) \quad (2.15)$$

On the figure 2.4 one can see examples of CTF plotted for *Tecnai F20 ST* microscope of different defoci settings by using the program CTF Explorer [10] and ElmiX [11].

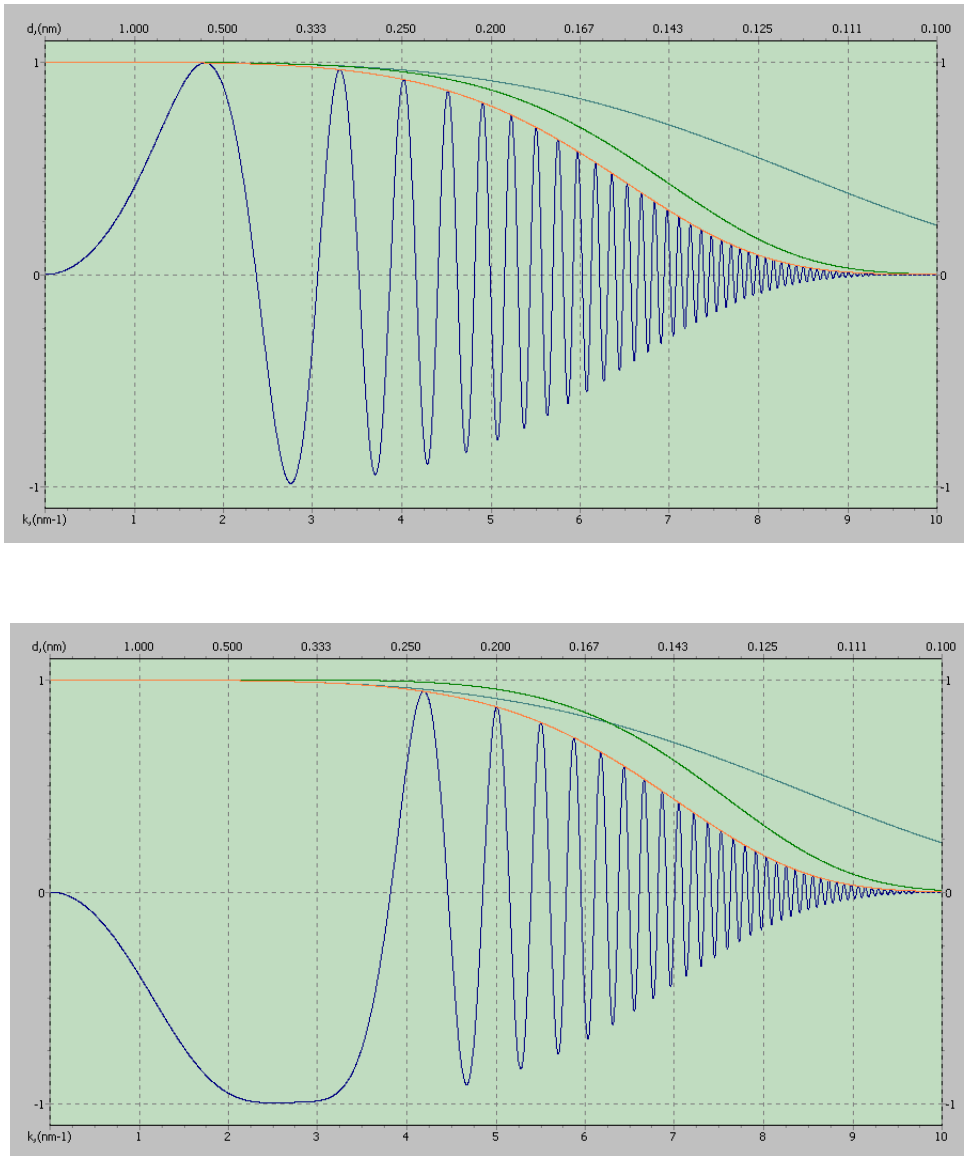


Figure 2.4: Contrast transfer functions plotted for *Tecnai F20 ST* microscope by using different defocus settings: $\Delta f = 50, -55$ nm. Green and blue curves represent spatial and temporal damping envelopes respectively. Yellow curve is combination of both envelopes. The contrast transfer is plotted both for real spacings and for reciprocal spatial frequencies. At low frequencies by overfocus one has positive contrast and negative contrast by underfocus. At high frequencies the CTF shows very strong oscillations. It results in delocalization of information

As one can see the contrast transfer function exhibits strong oscillatory behavior. It consists of number of „bands“ where it's almost constant which means good transmission properties. The passbands are separated by „gaps“ (zeros) where no transmission occurs. When $T(\mathbf{g})$ is negative, positive phase contrast results, meaning that atoms would appear dark against a bright background and vice versa. The first crossover of CTF with g - axis is called point-to-point resolution and refers to the minimum separation between two adjacent points.

Different factors contribute to CTF. One of them is damping envelope or attenuation of the wave. The simple reason of this phenomena is that the microscope is incapable to image the finest object's details. The mathematical form of damping function is very complex. In general it's product of following components:

$$E_T(\mathbf{g}) = E_c(\mathbf{g})E_s(\mathbf{g})E_d(\mathbf{g})E_v(\mathbf{g})E_D(\mathbf{g}) \quad (2.16)$$

Each component is individual envelope function responsible for corresponding partial coherence effect:

- $E_c(\mathbf{g})$: for non-monochromatic source
- $E_s(\mathbf{g})$: for finite size of source and therefore spread of angles from the probe (spatial damping envelope)
- $E_d(\mathbf{g})$: for specimen drift (can be determined from drift measurement)
- $E_v(\mathbf{g})$: for specimen vibration (so far it is not really clear how to measure it)
- $E_D(\mathbf{g})$: for the detector (because of image discretization by acquisition with CCD)

With sufficiently small drift and vibrations the most important contribution to contrast transfer are chromatic aberration envelope $E_c(\mathbf{g})$ and spatial coherence envelope $E_s(\mathbf{g})$. By multiplication of both these envelopes with contrast transfer function one gets effective transfer function:

$$T_{eff}(\mathbf{g}) = T(\mathbf{g})E_c(\mathbf{g})E_s(\mathbf{g}) \quad (2.17)$$

These damping functions can be considered like virtual aperture in the back focal plane of objective lenses. It means that higher-order passbands (high spatial frequencies) are suppressed. On the figure 2.4 envelope functions are shown as solid colored lines confining rapidly oscillating CTF.

The spatial damping envelope $E_s(\mathbf{g})$ is determined by spatial coherence of the source, which is linked to its finite size and energy spread. This damping function is determined by aberrations of the imaging system and has a Gaussian distribution:

$$E_s(\mathbf{g}) = \exp \left[- \left(\frac{\alpha}{2\lambda} \right)^2 \left(\frac{\partial \chi(\mathbf{g})}{\partial \mathbf{g}} \right)^2 \right] = \exp \left[- \left(\frac{\pi\alpha}{\lambda} \right)^2 (C_s \lambda^3 g^3 + \Delta f \lambda g)^2 \right] \quad (2.18)$$

, where α - semi-convergent angle characterizing this envelope. For high α we should expect decrease in resolution. However for aberration-corrected microscope this term can be neglected.

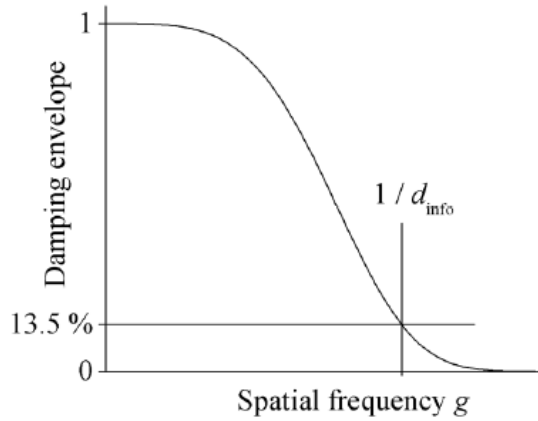


Figure 2.5: Partial temporal coherent envelope

The damping envelope caused by chromatic aberration is also known as temporal damping envelope and has the form:

$$E_c(\mathbf{g}) = \exp \left[-\frac{1}{2}(\pi\lambda\delta)^2 g^4 \right] \quad (2.19)$$

Here δ - is defocus spread due to chromatic aberration:

$$\delta = C_c \left[4 \left(\frac{\Delta I_{obj}}{I_{obj}} \right)^2 + \left(\frac{\Delta E}{V_{acc}} \right)^2 + \left(\frac{\Delta V_{acc}}{V_{acc}} \right)^2 \right]^{\frac{1}{2}} \quad (2.20)$$

, where $\frac{\Delta I_{obj}}{I_{obj}}$ and $\frac{\Delta V_{acc}}{V_{acc}}$ are the instabilities in the high-voltage power and objective lenses current. $\frac{\Delta E}{V_{acc}}$ describes the energy spread of electron gun. The temporal damping envelope is displayed on figure 2.5.

The damping properties of this envelope defines very important quantity of the microscope - information limit ρ . Usually it is determined through the spatial frequency $g_{info} = 1/\rho$ where the contrast drops down to $1/e^2 \approx 13.5\%$ of the unattenuated signal. The information limit is also very important quantity for exit-wave reconstruction. In exit-wave reconstruction the resolution can be enhanced up to the information limit.

Extending thickness range of WPO

The WPO approximation is quite limited by the thickness of the sample. Usually one speaks about WPOA if the thickness of the specimen does not exceed one quarter of extinction length. This important parameter describes Pendellösung behavior of electron beam by propagation through the sample [12]. Above this value dynamical effects are dominant. However the thickness range of this method can be extended by small tilts of the crystal out of the zone-axis. This effect was at first time intensively investigated by O'Keefe [13] by image simulations. The origin of this phenomena is illustrated on image 2.6.

The electrons scatter from the projected potential. For untilted sample all potentials along atomic column are superimposed. So the projected potential is very high. Slight tilt of the crystal out of the zone-axis changes the projected potential. The projected potential becomes lower in the direction of electron beam. For tilted sample the potential peak is much lower, therefore the scattering is less dynamic. As one can see from eq. 2.10 the amplitude of exit-wave function linearly depends from the phase which is proportional to the product of potential V_p and sample thickness. The intensity of atomic columns remains the same since this product does not change. Tilting the sample lowers the projected potential and increases the thickness range of WPO.

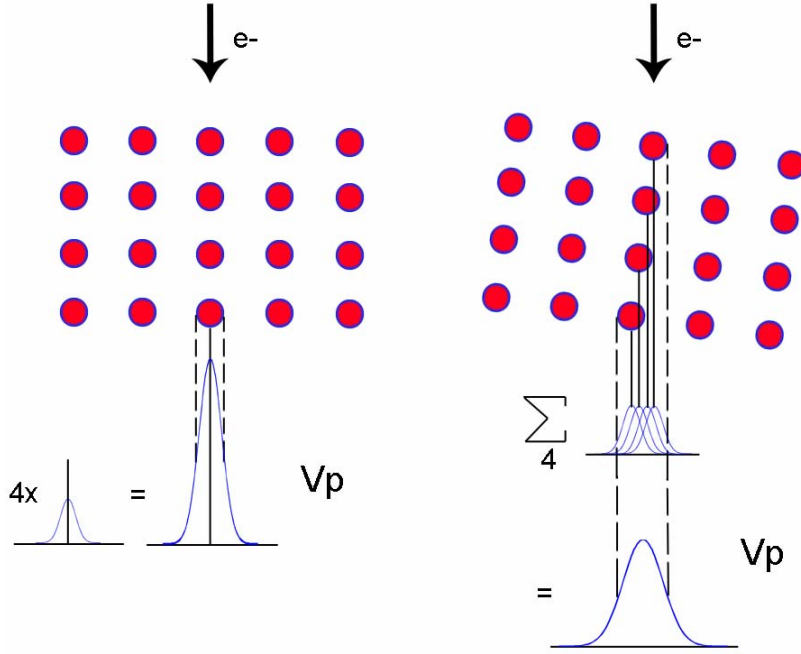


Figure 2.6: The effect of crystal tilt on scattering of electrons. The small tilt of the crystal out of the zone-axis lowers projected potential, hence scattering becomes more kinematic (single scattering)

Optimum defoci conditions for imaging

As it was already shown the CTF exhibits many reversals and gaps. This results in big delocalization and image interpretation becomes very difficult. An optimum contrast transfer would require a CTF, which takes only two values: +1 or -1 for all spatial frequencies. However it's not realistic in terms of real experiment. One of solutions to optimize contrast transfer is to extend the region of CTF without oscillations towards higher spatial frequencies. It can be achieved by varying the defocus value as can be seen from eq. 2.8. Thereby it's possible to keep the value of aberration function close to $\pm\frac{\pi}{2}$ (depending from the sign of C_s) and thus the value of CTF close to the ± 1 . This special defocus value is called Scherzer defocus:

$$Z_s = -\left(\frac{4}{3}C_s\lambda\right)^{1/2} \quad (2.21)$$

By this defocus setting the point-to-point resolution is maximum and defines point-to-point resolution of the microscope.

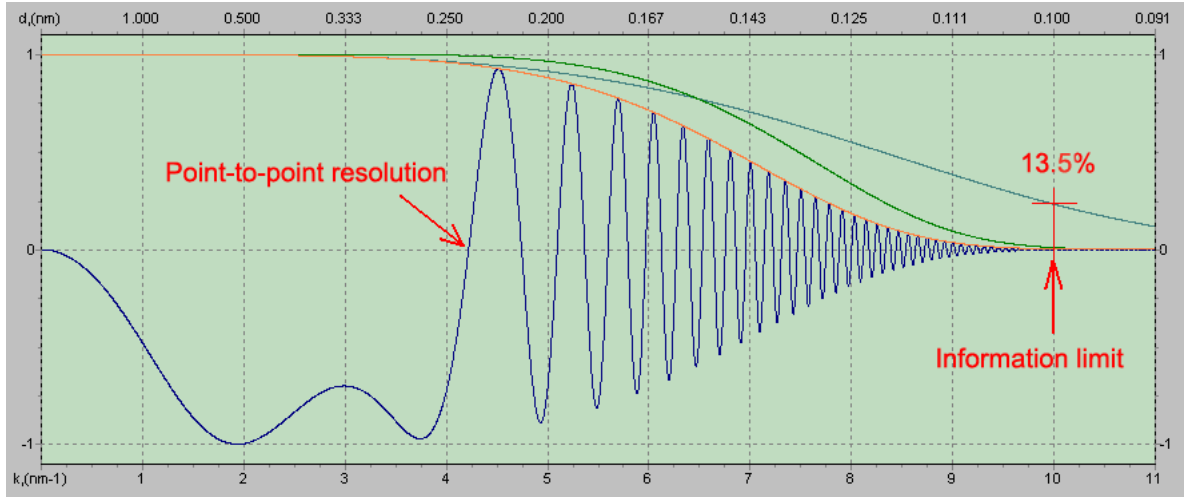


Figure 2.7: CTF plotted for Tecnai F20 ST microscope. The defocus corresponds to the Scherzer defocus and equals to -67.2 nm. The spatial damping envelope is represented with green solid curve and temporal damping envelope with blue curve. The damping by high spatial frequencies due to the spatial coherence is higher than the damping due to the chromatic aberration

$$g_s = \left(\frac{3}{16}C_s\lambda^3\right)^{-1/4} \quad (2.22)$$

The CTF at this defocus is displayed on figure 2.7. Another idea to optimize the imaging conditions is to distribute all oscillations of CTF homogeneously from 0 up to the highest spatial frequency g_{max} determined by information limit. Mathematically these strong oscillations originate from a significant gradient of aberration function $\frac{\partial\chi}{\partial g}$. The gradient of aberration function is linked to the beam displacements and therefore to the point-spread function. By searching of optimum conditions we try to minimize it. The explicit evaluation yields an optimum defocus condition:

$$Z_{opt} = -\frac{3}{4}C_s\lambda^2g_{max}^2 \quad (2.23)$$

This defocus setting is also known as Lichte defocus or defocus of least confusion. Usually focal-series acquisition for exit-wave reconstruction is made near Lichte defocus.

2.3 Improvement of resolution by aberration correction

The resolution of the microscope can be dramatically improved by correction of aberrations of lenses. In order to enhance the resolution and make images more interpretable modern generation of microscopes are equipped with special correctors. By using these correctors it's possible to compensate different aberrations as 2-fold astigmatism, spherical aberration, axial coma and even aberrations of higher orders. One distinguishes two different types of correctors: C_c - correctors for correction of chromatic aberration and C_s - correctors for correction of aberrations of objective lenses. The microscopes appointed with these special constructs are usually designated as aberration-corrected microscopes. There are different techniques used for estimation of aberrations. Among all of them one marks out hardware correction, software correction and image simulations. As I have said already hardware correction is performed during the acquisition by special correctors. If one has reconstructed exit-wave function of the specimen the aberrations can be revealed and compensated by special software. The qualitative analysis of aberrations can be also carried out by comparison of experimental images with simulated ones. In this chapter I'll explain main ideas what underlie measurement and correction of aberrations of objective lenses. However I did not have an aim to explain everything as detailed as possible. More full information about hardware correction and also correction algorithms can be found in corresponding sources [14, 15].

On the figure 2.8 one can see photograph and typical scheme of hexapole corrector. The idea to correct aberrations of lenses by using multipole elements were first suggested by O. Scherzer in 1947 and then realized by H. Rose in 1990 by way of double hexapole correctors.

Actually there are many different techniques for correction of aberrations including image correlations, evaluation of reconstructed wave functions and also diffractogram analysis. In this chapter I'll concentrate on last method. The evaluation of aberrations by acquisition of images presented in my diploma thesis was made also on the base of diffractogram analysis. The correction of aberrations is usually done

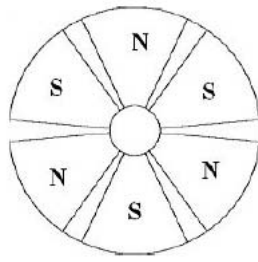


Figure 2.8: C_s corrector

on amorphous material for example carbon. On the figure 2.9 on can see image of amorphous material with corresponding FFT image.

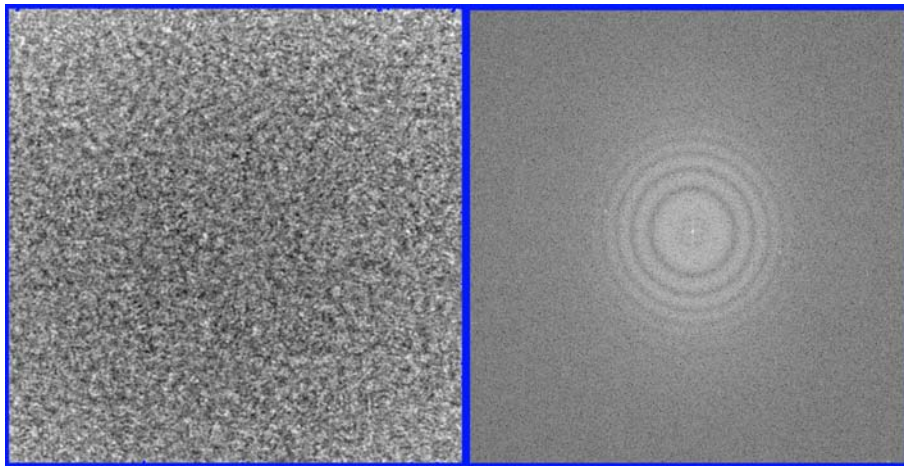


Figure 2.9: Image of amorphous carbon thin film with corresponding power spectrum

The film of amorphous carbon situates out of focus therefore we see several rings on diffractogram. For big defocus values these rings begin to converge to the center of FFT image. For image in focus these rings almost disappear. These typical ring pattern for amorphous materials was discovered and investigated at the first time by F.Thon [16]. The intensity of power spectrum of this image can be expressed in this way:

$$D(\mathbf{g}) = |I(\mathbf{g})|^2 \sim \sin^2[\chi(\mathbf{g})] \quad (2.24)$$

From this dependence one can see that dark and bright rings on power spectrum correspond to bands and gaps of CTF. Since the contrast transfer function is determined by aberrations of imaging system from analysis of diffractograms it is possible to calculate the value of defocus, 2-fold astigmatism, C_s and even aberrations of higher orders.

Small 2-fold astigmatism usually can be detected by the eye. If experimental image has small 2-fold astigmatism then rings (also known as Thon rings) on diffractogram will have elliptical form (see figure 2.10). It's possible to use these diffractograms for correction of astigmatism, since the perfectly stigmatized image has circular symmetry. For correction of 2-fold astigmatism in the microscope usually one uses stigmator.

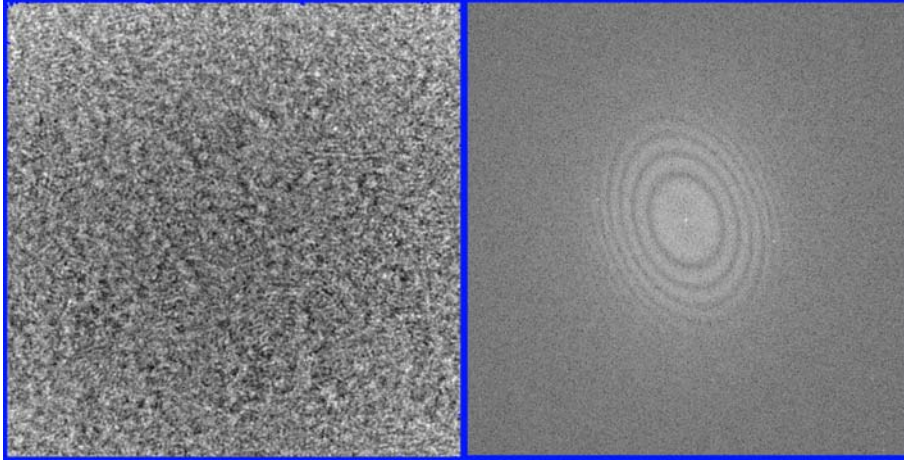


Figure 2.10: Image of amorphous material with 2-fold astigmatism and corresponding power spectrum

For small values of defocus and 2-fold astigmatism it's possible to determine them by measuring the radii of dark and bright rings. The bright rings correspond to $\sin(\chi(g)) = 1$ and dark rings correspond to $\sin(\chi(g)) = 0$. So we have two possible cases:

$$\text{dark rings : } \chi(g) = \frac{n\pi}{2}, n - \text{odd} \quad (2.25)$$

$$\text{bright rings : } \chi(g) = \frac{n\pi}{2}, n - \text{even} \quad (2.26)$$

By substitution of these values in equation 2.8 one gets:

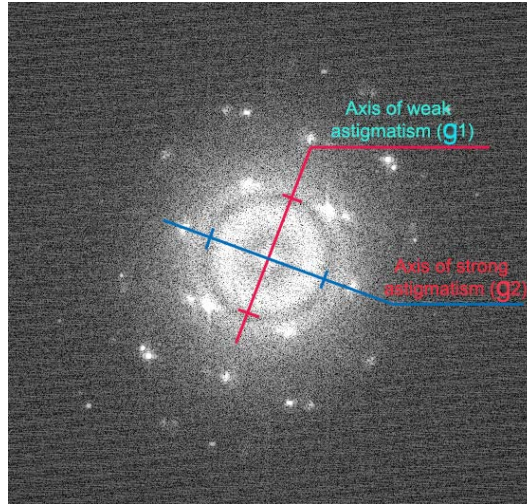


Figure 2.11: FFT of one HRTEM image from focus series ser-22

$$\frac{n}{g^2} = 2\Delta f\lambda + Cs\lambda^3g^2 \quad (2.27)$$

For estimation of defocus it's better to use first dark ring than the first bright ring. For first dark ring $n = 2$. For aberration corrected microscopes the second term can be neglected (in this case the typical values for C_s are of the order of tens of μm). So now we can express the value of defocus:

$$\Delta f = \frac{1}{\lambda g^2} \quad (2.28)$$

Because of 2-fold astigmatism we have so called directed defocus. The largest and smallest axle of elliptical rings are known as axis of weak and strong astigmatism (g_1 and g_2 correspondingly, see figure 2.11). On the image above axis of strong astigmatism seems to go through two reflexes which is occasional situation. In general it's not the case. The values of g_1 and g_2 are measured from the origin of FFT image to the radius of first dark ring. The directed defocus can be characterized with two values:

$$Z_1 = \frac{1}{\lambda g_1^2}, Z_2 = \frac{1}{\lambda g_2^2} \quad (2.29)$$

And finally the defocus and 2-fold astigmatism can be calculated as average and difference of these both values respectively.

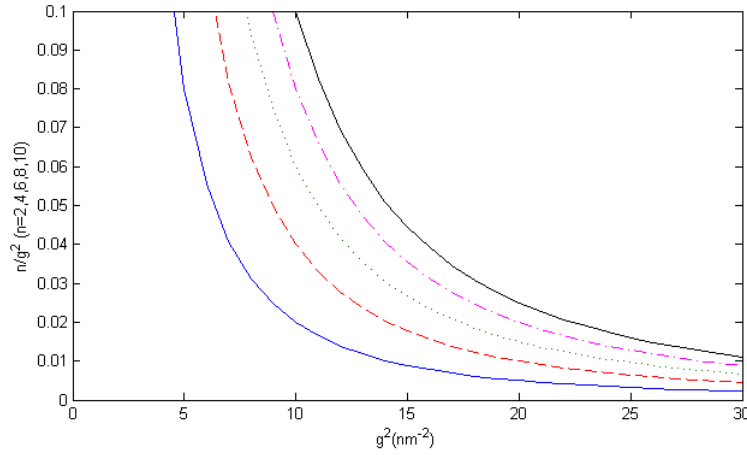


Figure 2.12: Hyperboles of n/g^2 vs. g^2 used for estimation of Δf and C_s . Hyperboles are plotted for dark rings in diffractogram for $n=2,4,6,8,10$.

$$Z = \frac{Z_1 + Z_2}{2} \quad (2.30)$$

$$A = \frac{|Z_1 - Z_2|}{2} \quad (2.31)$$

This simple analysis is quite important for exit-wave reconstruction by estimation of starting defocus. The estimation of C_s is more complicated. For none aberration-corrected microscopes one should take it into account C_s by determination of positions of rings. Here one needs at least two bright or two dark rings. By plotting nu^{-2} versus u^2 in equation 2.27 one obtains straight line with slope $C_s\lambda^3$, and with an intercept on the nu^{-2} axis of $2\Delta f\lambda$. More precise analysis was suggested by Krivanek (1976) and can be achieved by plotting hyperbolas for each particular value of n versus n^2 (see figure 2.12). Then the experimental points can be put on these hyperbola. By linear fitting of points one can calculate value of C_s for any microscope and Δf .

This method is quite useful however this simple diffractogram analysis is not enough to reveal aberrations of odd orders and also higher-order aberrations. In order to extract the information about higher-order aberrations one usually acquires diffractograms by tilted illumination. By tilting it's possible to reveal the asymmetric aberrations which remain concealed in the on-axis image. In this method so called Zemlin tableau is used.

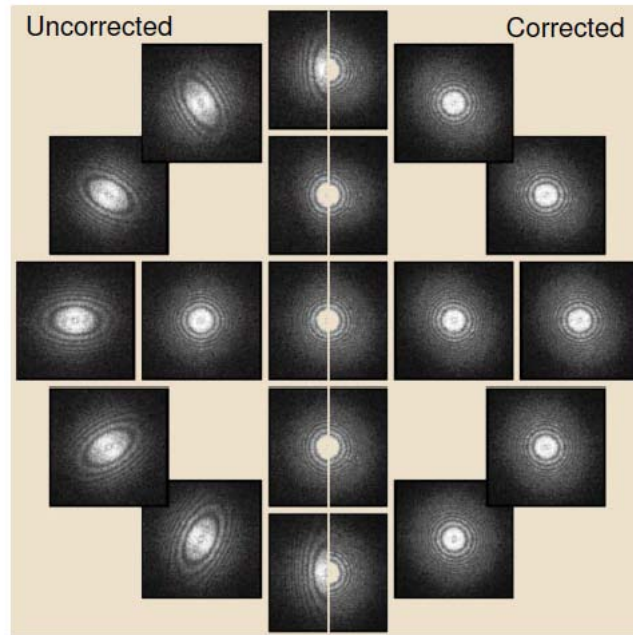


Figure 2.13: Zemlin tableau: series of diffractograms acquired by different tilting angles around the optical axis. On the left hand side series of images before aberration correction, on the right hand side - after aberration correction

Mathematically the effect of beam tilting can be expressed in this way:

$$\chi(\mathbf{g}) \implies \chi(\mathbf{g} + \mathbf{t}) \quad (2.32)$$

, where t - the plane component of wavevector of tilted beam. This transformation can be evidently expanded on the base of equation 2.9. Afterwards one gets the system of linear equations which describes relationship between aberration coefficients of on-axis and tilted beams. By using inverse transformation it's possible to extract even aberrations of 6th-order. For assessing of quality of correction two dimensional CTF is used (see figure 2.14).

For HRTEM measurements the standard Zemlin tableau consisting of 18 images is used. However for imaging in STEM mode usually enhanced tableau is applied where 3 images are taken for each tilt angle. The aberration correction is sensitive to many factors. For each magnification mode aberration correction should be made separately. Therefore all measurements presented in this work were made only in Mh - mode. It's better to do aberration correction away from crystalline materials, because Bragg reflections in FFT from crystalline can produce effect of local order

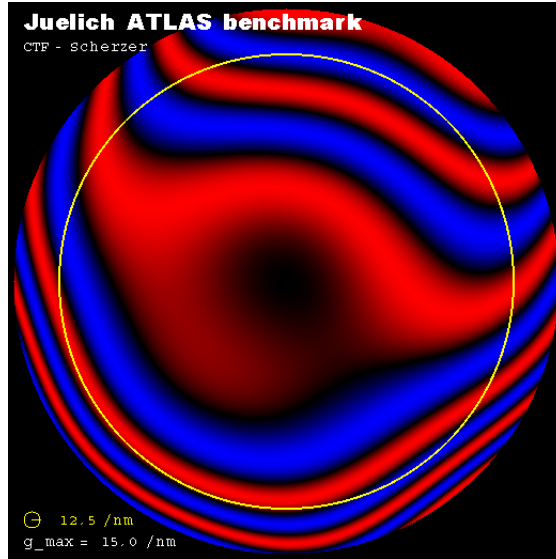


Figure 2.14: 2-dimensional CTF plotted for Scherzer defocus.

which can influence the correction algorithm. If one has amorphous material with different thickness some part of Thon rings can disappear which also complicates the correction. There are also a lot of many factors contributing to the correction.

2.4 Image simulations

The image simulations is very useful to investigate the structure of materials. Simulated image depends from microscope parameters as aberrations of lenses and properties of electron source. The object geometry and orientation in respect to the electron beam can influence as well. Also image simulations can help to understand better multiscattering effects in the specimen.

The quantum mechanical behavior of electrons propagating through the crystal is governed by the Schrödinger equation:

$$\left[-\frac{\hbar^2}{2m} \nabla^2 - eV(\vec{r}) \right] \psi(\vec{r}, t) = E\psi(\vec{r}, t) \quad (2.33)$$

, where $\psi(\vec{r}, t)$ - complex wave function of electrons, E - energy of electrons, e and m - charge and mass of electrons, $-eV(\vec{r}, t)$ - is the potential of electrons inside the crystal. In TEM the electrons are accelerated up to very high energies. The acceleration voltage U varies from 80kV up to 1250 kV (Max Plank Institute,

Stuttgart, 1990). By these high energies already relativistic effects should be taken into consideration. The Schrödinger equation is not relativistic one. However by image simulations one often use compromise and substitute relativistic wavelength and mass into eq. 2.33. More correct solution can be given by relativistic Dirac equation. However its quite difficult to deal with mathematically.

Two main methods to calculate image of transmission electron microscope:

- The Bloch-wave approach
- The multislice approach

The first method was at first time proposed by Fujimoto (1978) and Kambe (1982). By using this approach the electron wave function is written as a sum of Bloch waves, which have the periodicity of the lattice and satisfy the Schrödinger equation. The advantage of this method is analytical solution. However this method gives quite good approximation only for perfect crystals. For simulation of images of defects and quasicrystals usually multislice method is used.

The multislice method was first described by Cowley and Moodie [17] and later expanded by Goodman and Moodie [18]. The idea of multislice method is to divide the specimen into many slices which are normal to the incident beam. One projects the slice onto a plane between slices (bottom, top or middle) giving projected potential for this slice. It is called phase grating. Then we let our electron beam propagate through the slice sequence interacting with projected potential. Afterwards the phase and amplitude for scattered electron waves are calculated for each slice. The last slice gives us exit-wave function of the specimen.

Essentially the multislice method can be described by equation assuming very thin slices:

$$\psi(x, y, \Delta z) \approx p(x, y, \Delta z) \otimes [t(x, y, z)\psi(x, y, z)] \quad (2.34)$$

, where $p(x, y, z)$ - is propagator function, $t(x, y, z)$ - transmission function (it's Fourier transform is also called phase-grating function). Approximation means that we assume very thin slices. $t(x, y, z)$ and $p(x, y, z)$ are given by:

$$t(x, y, z) = \exp \left[i\sigma \int_z^{z+\Delta z} V(x, y, z') dz' \right] \quad (2.35)$$

$$p(x, y, \Delta z) = \frac{1}{i\lambda\Delta z} \exp \left[\frac{i\pi}{\lambda\Delta z} (x^2 + y^2) \right] \quad (2.36)$$

$$P(k, \Delta z) = FT(p(\vec{r}, \Delta z)) = \exp[-i\pi\lambda k^2 \Delta z] \quad (2.37)$$

For iterative calculation the equation 2.34 should be discretized. If each slice is labeled with n then from eq 2.34 follows:

$$\psi_{n+1}(x, y) = p_n(x, y, \Delta z_n) \otimes [t_n(x, y)\psi_n(x, y)] \quad (2.38)$$

For numerical solution of this equation it is very convenient and time efficient to use Fast Fourier Transformation (FFT). Then equation 2.38 can be rewritten as:

$$\psi_{n+1} = FT^{-1}\{P_n(k_x, k_y, \Delta z_n)FT[t_n(x, y)\psi_n(x, y)]\} \quad (2.39)$$

However by derivation of this equation we don't take into account aberrations of the imaging system. One can consider the aberrations of objective lenses by adding phase shift to the wave-function. If one consider only defocusing and spherical aberration the phase shift is given by eq. 2.8. However in modern software packages one can include also damping of high frequencies by *chromatic aberration/temporal coherence* or *beam divergence/spatial coherence*. More detailed information and also examples of multislice simulations can be found in [19].

3 Experimental Techniques

3.1 Preparation of the samples

In my diploma thesis I investigated two different systems: chemically disordered $Fe_{45}Pt_{55}$ and Au nanoparticles. $Fe_{45}Pt_{55}$ nanoparticles have presumably cubic morphologies with average size of 8 nm. I've also analyzed Au NPs with Decahedron morphologies of 3 different average sizes: 3-5 nm, 10 nm and 60-70 nm. Both $Fe_{45}Pt_{55}$ and Au NPs were prepared by organometallic synthesis. $Fe_{45}Pt_{55}$ nanoparticles were prepared by Prof. Sun and his coworkers from IBM T.J.Watson Research Center. The detailed preparation procedure can be found in the article [20]. Au nanoparticles of different sizes were prepared according to three different methods. The synthesis was done by Miguel Comesana-Hermo.

- $Fe_{45}Pt_{55}$ nanoparticles

Originally 6.9 nm $Fe_{50}Pt_{50}$ nanocubes were synthesized by decomposition of $Fe(CO)_5$ in oleic acid and by adding of benzyl ether/octadecene solution of $Pt(acetylaceton)_2$. The nanoparticles were synthesized by lower temperature than usually. The shape was controlled by addition of oleic acid. Different ratio of Fe and Pt atoms in the nanoparticles can be achieved by varying amount of introduced precursors.

- 3-5 nm Au NPs

The NPs of this diameter were synthesized according to the recipe described by Jane and coworkers in [21]. The NPs were prepared as citrate-capped by the reduction of $HAuCl_4$ with sodium borohydride. First of all the water solution containing $HAuCl_4$ as a precursor and tri-sodium citrate was prepared in a conical bottle. After addition of $NaBH_4$ solution the original solution turns

brown red which was evidence of formation of nanoparticles. The solution during the addition should be kept by low temperature. Therefore the bath containing water with ice was prepared.

- 10 nm Au NPs

These NPs were synthesized according to the recipe provided in the work [2] by reduction of *AuCl* with the tert-butylamine borane(TBAB) complex in the presence of oleylamine in THF at room temperature. The solution was prepared in two steps. In the first step THF was dissolved in *AuCl* and oleylamine mixing with a vortex. Afterwards solution of TBAB was added in THF. After addition of TBAB the solution becomes dark brown which means formation of small seeds. At this stage the size of seeds was approximately 5 nm. In the second step some *AuCl* and oleylamine in different proportion was added in order to activate seeds growing. The final seeds solution was adjusted by magnetic stirring.

- 60-70 nm Au NPs

The NPs were synthesized by the method based on polyol process. More detailed information about the synthesis can be found in the work of D. Seo in [22]. By varying amount of reactants different nanocrystals of different polyhedral morphologies including decahedra can be synthesized by this method.

After preparation the solutions were stirred in microtiter in order to achieve homogeneous dispersion and without agglomerates. After that the nanoparticles were deposited on the TEM grids. I used $5\mu\text{l}$ pipette from Eppendorf to drop some solution on TEM grids. After that I let the solution to dry out at room temperature. To fix the sample and to deposit the nanoparticles only on one side of TEM grid, special self-closing anti-capillary tweezers from DUMONT© were used. These tweezers were specially designed for handling of TEM grids. The solutions of nanoparticles were quite saturated. In order to reduce the concentration the part of solution of FePt NPs was diluted with hexane to make it almost transparent. The original solution of Au NPs had saturated red color. To decrease the concentration of Au NPs the solution was diluted with distilled water until it took weak reddish hue. In order to remove the rest of solution directly from TEM grid special filter paper was used.

However with aqueous solution of Au NPs it is not recommended. If one tries to touch the water drop with filter paper then almost the whole drop will be absorbed.

For HRTEM measurements I used normal TEM grids (S160-3 with copper-grid covered with carbon film on one side) as well as ultra-high resolution carbon TEM grids. The second ones were especially designed for HRTEM measurements with highest possible resolution. Because of very thin supporting carbon film it's possible to reduce dramatically the signal from amorphous material and to enhance the contrast of crystal part. For my measurements I used two different specifications: STEM150Cu and STEM100Cu. These two types of TEM grids differ in thickness of amorphous carbon film. For STEM150Cu the thickness amounts less than 15 nm and for STEM100Cu even less than 10 nm.

After preparation the samples were examined in TecnaiF20 microscope. Imaging of the samples in SA magnification mode shows monodisperse distribution of NPs. On the pictures of FePt nanoparticles one could also recognize locally self-assembly because of magnetic interactions. First testing of samples shows quite big amount of organic solvents on the sample. One can easily recognize the presence of contamination by focusing electron beam on some part of amorphous material. These area becomes dark due to chemical reactions induced by electron beam. It is not acceptable for HRTEM imaging and focal acquisition. In order to reduce the amount of solvents on the samples plasma cleaning was carried out. This procedure was made with commercial Model 1020 of plasma cleaner from Fishline© (see figure 3.1).

For cleaning procedure mixture of argon and oxygen gases was used. The duration of plasma cleaning was set to 10 s in order to prevent the damage of carbon film. The results of cleaning procedure are shown on figure 3.2. Two top dark spots marked with blue ellipses were made before plasma cleaning by focusing electron beam on some area of sample for 3 and 9 minutes respectively. The bottom right spot marked with red ellipse was made after plasma cleaning by focusing electron beam for 9 minutes. The plasma cleaning and posterior characterization was made without removing the TEM grid from the holder. For that the CompuStage of the microscope allows to save current position on the sample and go back if necessary. The comparison of these spots shows efficiency of plasma cleaning to increase the quality of samples.



Figure 3.1: Plasma cleaner Model 1020 from Fishline ©

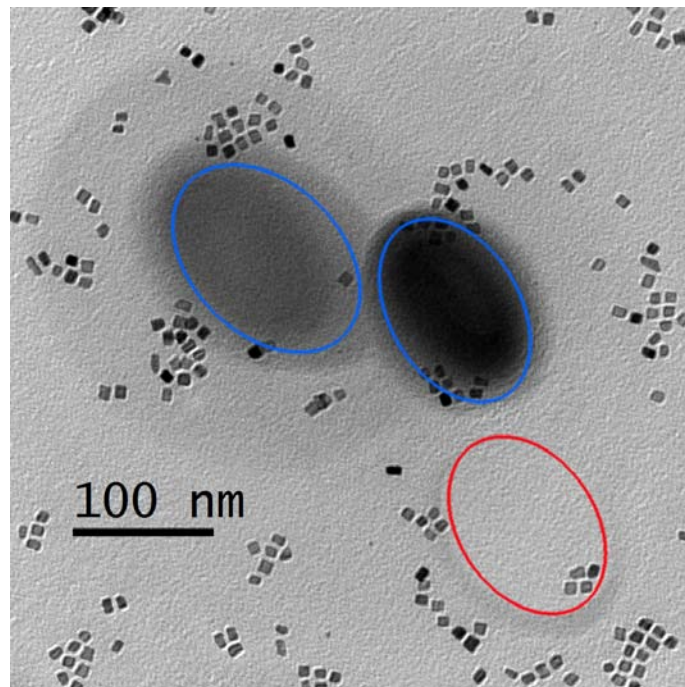


Figure 3.2: Results of plasma cleaning

3.2 Microscopes

I used three different microscopes. *Tecnai F20* in Duisburg-Essen university was used for pre-characterization of the samples and also for tilting experiments with gold nanoparticles. For focal-series acquisition and HRTEM imaging aberration-corrected

microscope *Titan 80–300 TEM* in Ernst-Ruska-Centre in Forschungszentrum Jülich was used. And also *Philips CM12* microscope was used for carrying out of tilting experiments. All these microscopes are shown on the pictures. More detailed information about main characteristics and operation modes of these microscopes can be found in Appendix.



Figure 3.3: Tecnai F20 microscope in Duisburg-Essen university (left) and Titan 80-300 TEM microscope in Ernst-Ruska Centre in FZ Jülich

3.3 Exit Wave Reconstruction (EWR)

3.3.1 Acquisition of focal series in TEM

Exit-wave reconstruction (EWR) is one of the main techniques I used in my diploma thesis. This special method of characterization of materials was proposed by Peter Schiske as early as 1968. Since then this method has been developed and now it is widely used in materials science [1]. The goal of this method is to retrieve the complex exit-wave function of the investigated specimen. More detailed information about this method and especially mathematical background can be found in [23]. In general EWR can be considered like the inversion of the imaging process



Figure 3.4: Philips CM12 microscope in Duisburg-Essen university

in the microscope. There are several advantages of this method in comparison with conventional HRTEM imaging. First of all the reconstructed wave function is more complete than any HRTEM image recorded in the microscope. The exit-wave function contains amplitude and phase information about the specimen whereas phase information is lost during normal imaging. The reconstructed exit-wave function is free from imaging artifacts including aberrations of lenses. This fact allows us to interpret the results without reference on current microscope conditions. The next more important advantage of EWR technique is enhancement of resolution. By using EWR it's possible to reduce delocalisation effects and non-linear artifacts and consequently to enhance the resolution up to the maximum possible value: information limit of the microscope.

The exit-wave reconstruction is also known in microscopy science as focal-series reconstruction. The reconstruction procedure is illustrated on the figure 3.5. In general it consists of two different parts: experimental and computational part. In the experimental part we acquire series of atomically resolved images of the same area by using CCD camera. The acquisition is automatically controlled by computer. A series of images is acquired with different defoci of objective lenses. Usually during the

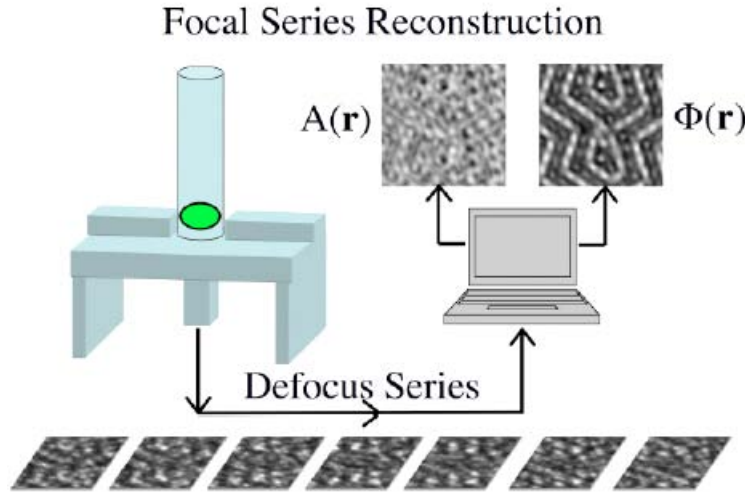


Figure 3.5: Focal-series reconstruction

measurement in Ernst-Ruska centre we acquired series of 22 images with defocus step 2 nm. For reconstruction procedure *TrueImage Professional* software was used which requires at least 10 images. The focus step was set to 2 nm. The images were acquired from underfocus toward overfocus. It was reasonable because the perfect image in the series characterized by Lichte defocus [5] situated in overfocus. After focal-series acquisition Zemlin-tableau was recorded. Aberrations were measured in order to monitor it's evolution.

3.3.2 EWR by using TrueImage

For EWR I used professional version of commercial program TrueImage. In professional version it's possible to perform posterior correction of residual aberrations for reconstructed wave function. All images should be saved in dat-files according to the following format: *filename_xxx.dat*. It's simple data binary file without header and 2 bytes per pixel. However there is also possible to save the whole focal-series in special **.ebn*-format. This format was designed especially for handling the data for EWR. However it requires some additional plugins for data conversion. The images in *Titan*-microscope were recorded with UltraScan 1000P CCD with resolution of 2048x2048 pixels. TrueImage uses following dimensions of reconstruction area 768x768, 1024x1024, 1280x1280 pixels. Usually I used two last sizes. Drift compensation algorithm implemented in TrueImage requires reconstruction area dimensions

to be smaller than the whole image size. The main interface of TrueImage software is shown on the figure 3.6.

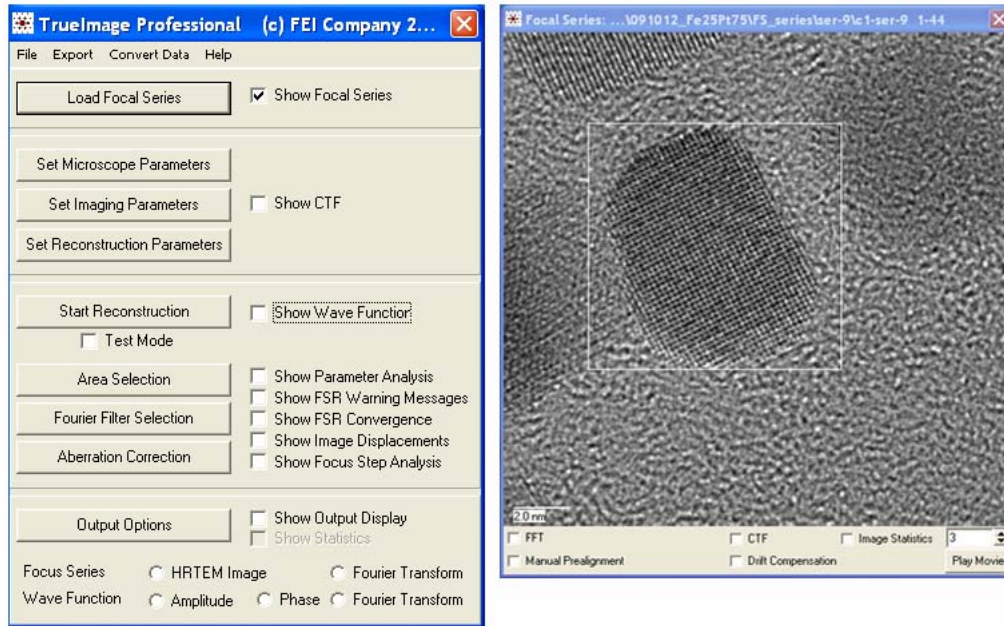


Figure 3.6: The main interface of program TrueImage

After loading of focal series it can be displayed in graphical window. In this window we could also select the reconstruction area. Afterwards reconstruction parameters should be set.

On the figure 3.7 one could see three panels with microscope, imaging and reconstruction parameters.

Microscope parameters

- high tension (in kV)
- spherical aberration C_s (in mm)
- focus spread or information limit (in nm)
- MTF (Modulation Transfer Function of CCD) at Nyquist Freq. (dimensionless parameter, for reconstructions I used 0.05, 1 for simulated images).

Imaging parameters

- Sampling rate or discretization of the image (in nm/px); this value should to be taken from calibration table for different magnifications.

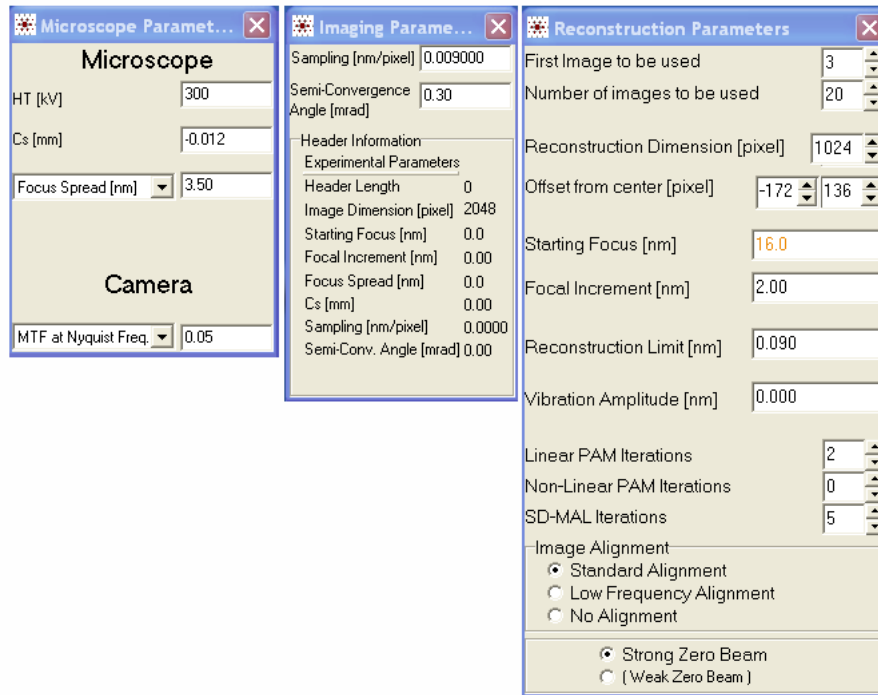


Figure 3.7: Different panels of TrueImage with reconstruction parameters

- Semi-Convergence angle α (characterize Gaussian distribution of electron beam, measured in mrad)

The value of C_s was taken from subsequent aberration measurements. For this reason we used standard Zemlin tableau consisting of 18 images of amorphous material recorded by beam tilting angle of 18 and 36 mrad.

Reconstruction parameters

- First image to be used: first image from focal-series to be used for reconstruction
- Number of images to be used: number of images to be used for reconstruction (maximum value - 20, minimum value - 10)
- Reconstruction dimension: dimensions of reconstructed area (in pixel)
- Offset from the center: pixel coordinates of the middle of reconstructed area
- Starting defocus: defocus value of first image in focus-series used for reconstruction (in nm). For underfocus this value should be negative and for overfocus

should be positive. It's better to estimate starting defocus from the first image if it was recorded in big underfocus or from the last image if it was acquired in big overfocus by subtracting number of images multiplied by focal step size. Simple procedure how to estimate starting defocus was described in „Basics“ .

- Focal increment: focus step used for reconstruction (in nm). Negative focal increment means the images are recorded from overfocus to underfocus.
- Reconstruction limit: numerical algorithm retrieves all spatial frequencies up to the reconstruction limit (nm). This value should be close to the information limit of the microscope. For all reconstructions I used a value of 0.09 nm.
- Vibration amplitude: consider mechanical vibrations during acquisition (usually set to 0)
- Linear PAM iterations: maximum number of PAM (Paraboloid method) iterations (usually set to 0)
- Non-linear PAM iterations: number of non-linear PAM iterations (usually 0)
- SD-MAL iterations: Number of nonlinear iterations for comparison of simulated images with experimental focal-series. Nonlinear maximum-likelihood algorithm (MAL) is used.
- Image alignment: the method of cross-correlation between subsequent images in focal-series to compensate drift. Low-frequency alignment is quite effective for big thermal drift. For simulations no alignment is used.
- Strong Zero Beam: is assumed if the zero-beam amplitude is larger than $\sqrt{1/2}$ (for the image the mean intensity is normalized to 1). For all reconstructions I used this option.

After setting all parameters reconstruction can be started. The reconstruction is accomplished with a tandem combination of a noise-improved linear inversion scheme followed by an iterative nonlinear procedure called maximum-likelihood (MAL) scheme. In the last step the raw wavefunction reconstructed by linear method is slightly modified. From the modified wave function the series of 92 images by different defocus is simulated and compared with experimental series. Afterwards the

assessment of reconstruction procedure follows. If one has „Poor correlation between simulated images and experimental data“ means the reconstruction failed, if „Info loss due to step size variations “ or „Info loss due to focal instability“ the reconstruction was successful. On the figure 3.8 one could see typical subsequent focal-series analysis.

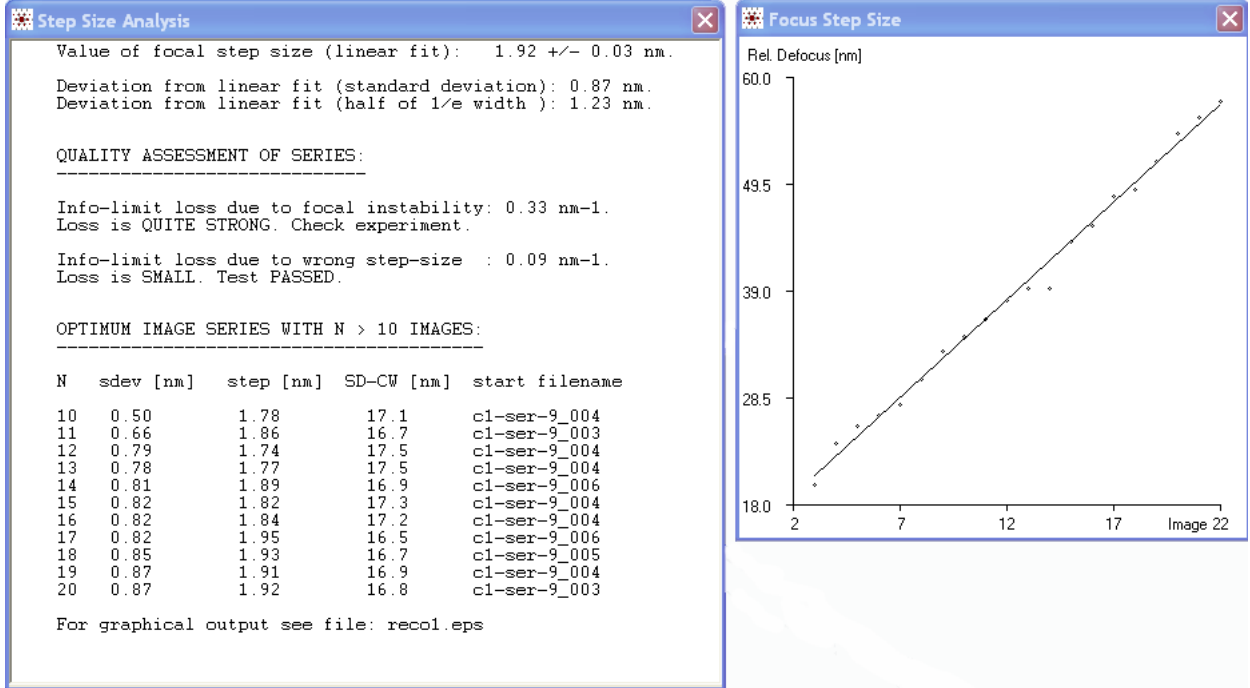


Figure 3.8: Focal-series analysis for assessment of quality of reconstruction

From the linear fit of relative defocus we could observe focal jumps. The program automatically calculates the optimum focal-series with corrected focal step size.

The next very important step of EWR is correction of so-called residual aberrations. This step should be made in order to enhance the quality of reconstructed wavefunction. These aberrations can arise some problems for two reasons: first of all not all of them can be sufficiently well corrected by an hardware corrector. Second, the aberrations are not stable in time and can degrade already after a few minutes after correction. In comparison with an image, a wavefunction allows direct compensation of residual aberrations. The initially reconstructed wavefunction Ψ_R is given by:

$$\Psi_R(\mathbf{g}) = \Psi_O(\mathbf{g}) \exp(-i\chi_R(\mathbf{g})) \quad (3.1)$$

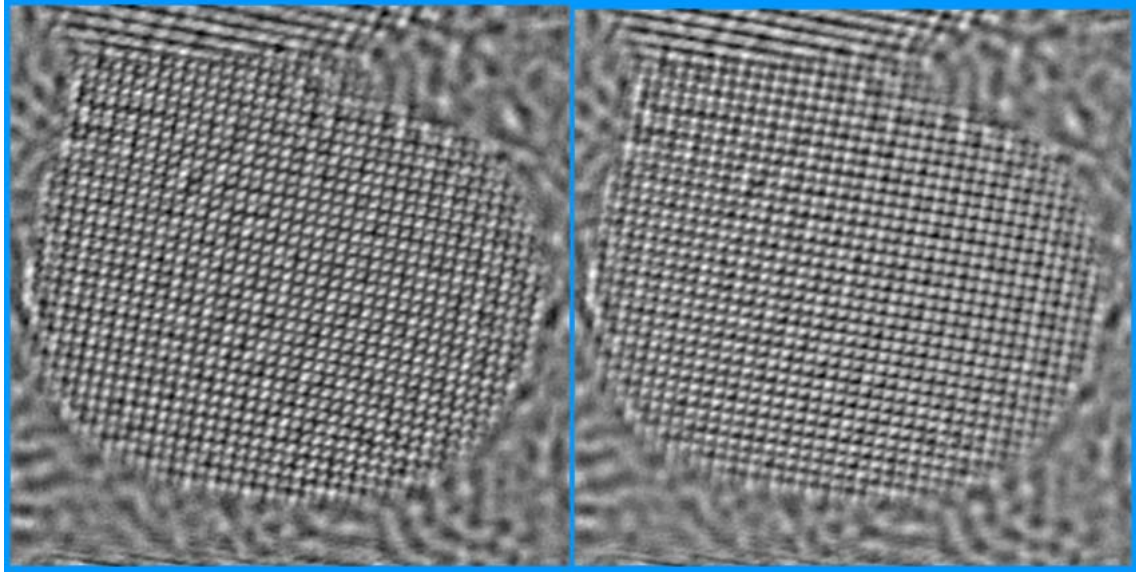


Figure 3.9: Comparison of phase image before and after correction of residual aberrations

which can be inverted towards the object wavefunction Ψ_O by multiplying with complex-conjugate phase transfer function $exp(i\chi_R(\mathbf{g}))$:

$$\Psi_O(\mathbf{g}) = \Psi_R(\mathbf{g})exp(i\chi_R(\mathbf{g})) \quad (3.2)$$

In TrueImage it's possible to correct defocus, Coma-aberration, 2- and 3-fold astigmatism. Defocus and 2-fold astigmatism can be corrected automatically by minimizing real part of wavefunction and thereby enhancing contrast of phase image. However it does not guarantee the best result. The best way is to correct all aberrations independently by making *aberration – movie* (f.e. for 2-fold astigmatism: select the amplitude of aberration and change the direction with some angle step). The coma-aberration can be recognized from the tails coming from the image of atomic columns. Once aberrations are known, they can be corrected by a so called numerical phase-plate defined by $\chi_R(\mathbf{g})$. On the figure 3.9 one can see results of this correction.

3.3.3 Peaks Determination

For exact measurement of interplane distances one needs to know exactly the positions of maxima of intensity. For this purpose I used Peak-Pairs Analysis (PPA)

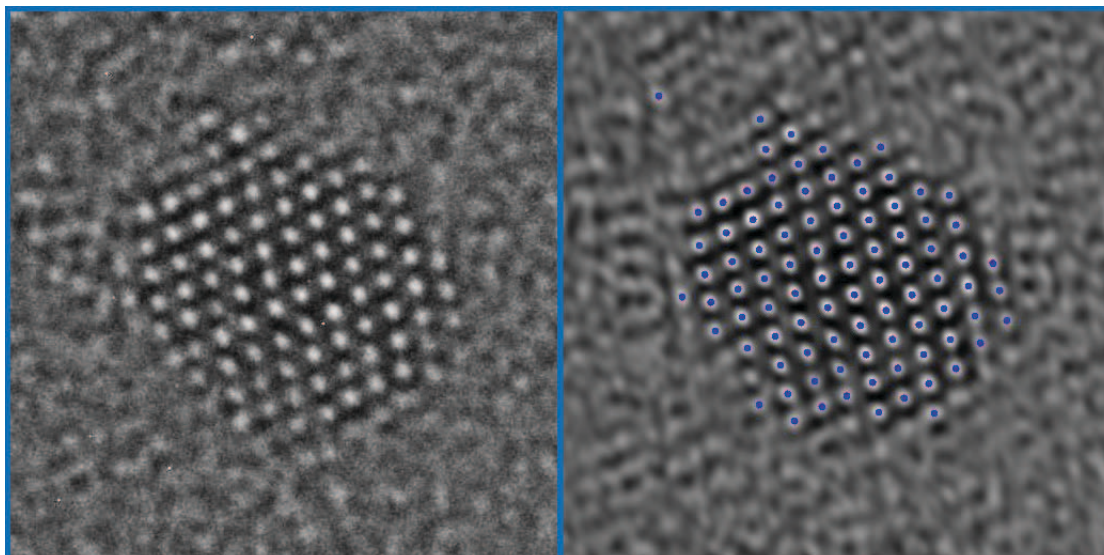


Figure 3.10: HRTEM image of Au nanoparticle on the left and Bragg filtered image of the same nanoparticle with positions of maxima of intensity

software designed for high-resolution peak measurement and strain mapping analysis. Detailed information about this method can be found in [24]. PPA uses real-space approach for detection of maxima of intensity since there are another methods like Geometric Phase Analysis calculated in Fourier Space. On the figure 3.10 one could see HRTEM image of small gold nanoparticle together with Bragg filtered image with pinpointed positions of atomic columns.

Before analysis of lattice points the image should be prepared. The HRTEM image usually has very low signal-to-noise ratio. This noise can result in large number of sharp local maxima which can complicate the analysis. In order to reduce noise Bragg filtering is implemented in the program. First of all Power Spectra need to be calculated. After applying circular masks around the spots corresponding to crystalline material and making inverse transformation the noise can be considerably reduced. However this filtering produces some undesirable artifacts like „ghost“ atoms and shift of maxima. More detailed analysis of these effects I'll give in „Results and Analysis“ section. In order to find peaks of intensity one needs to define threshold value and also minimum peak distance. The program calculates local maxima (8-neighbourhood) on a pixel basis and also refined maxima at sub-pixel resolution. Sub-pixel resolution is achieved by fitting a 2D quadratic function and calculating analytically the maxima.

3.4 Image simulations

3.4.1 Modeling of nanoparticles

For modeling of nanoparticles I used special software „Generator“. The program was written by myself in mathematical package MATLAB and then compiled as stand-alone application. The main goal of this program is to generate atomic coordinates of nanoparticles of different morphologies and structures for HRTEM simulations. However this software can be also useful just for visualization of different structures. Models used for simulations presented in the current work were modeled by using this software. The program has intuitive graphical user interface which makes modeling easier and quicker. The detailed information about usage of this software can be found in Appendix. Examples of some codes implemented in Generator can be found in MATLAB Central User Community in File Exchange section. Geometrical analysis of some structures with molecular dynamics simulations can be found in these articles [25] and [26].

3.4.2 QSTEM software

All simulations presented in this work were made by using QSTEM software. This program was written by Christoph Koch from Max Plank Institute of Metals Research and can be downloaded free of charge from his website [27]. QSTEM stands for Quantitative Scanning Transmission Electron Microscopy. However this program offers wide possibilities for simulation of HRTEM images. The program uses multi-slice approach for calculation of projected potentials and wave functions of electrons.

In order to carry out the simulation first of all one needs to create data file containing the coordinates of the model. QSTEM uses special format of files with extension *.cfg. This file was originally created for AtomEye atomistic configuration viewer for visualisation of complex molecular structures. Short description of this format and most important parameters can be found in Appendix.

On the figure 3.11 one can see main interface of QSTEM. The main interface was divided into several panels where it's possible to set different parameters of simulation. After creating the data file with atomic coordinates the model can be loaded and displayed in the main graphical window of the program. In the graphical

window one can see the model enclosed into the simulation box and divided into slices. In the section „Slicing“ it’s possible to set the number of slices and potential offset. Potential offset means the shift of calculated projected potential relative to the slice slab. The thickness of the slice is calculated automatically from the number of slices and dimensions of the simulation box.

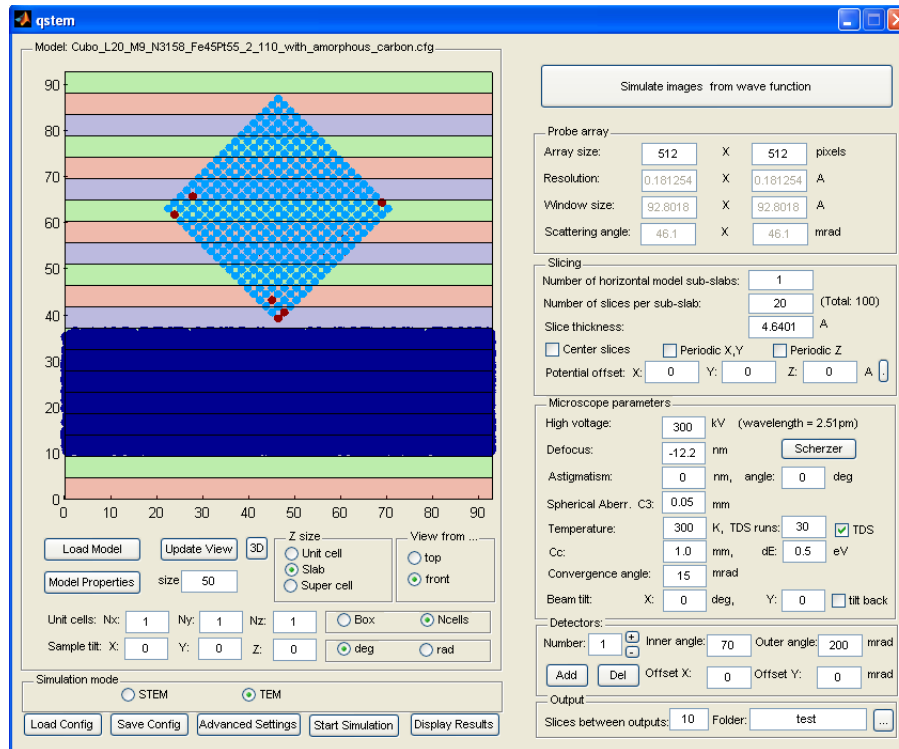


Figure 3.11: Main interface of QSTEM program

To perform simulations along different zone axes and also investigate contrast-transfer effects due to the tilting of the sample one can rotate sample along different axes.

Simulations can be performed in different modes: STEM and TEM. By switching between these two options the interface of the program is adapted to specific simulation mode. By STEM simulations presumably inelastically scattered electrons contribute to the formation of the final image.

In „Probe array“ - section one can define size of probe array which is actually equal to the resolution of the final image. The resolution or discretization rate of the final image is calculated automatically as a ratio of size of simulation box and the size of probe array. The parameter „Scattering angle“ defines maximum value of wave

vector of scattered electrons contributing to the formation of the final image. This parameter has the meaning of aperture function due to the probe discretization.

In the section „Microscope parameters“ it's possible to set different parameters of imaging system. For quantitative comparison of simulated images with experimental ones these parameters should be close to experimental conditions as possible. For simulations I used parameters taken from the table of technical characteristics of *Titan 80-300* microscope (see Appendix). All these parameters especially defocus of objective lenses are necessary for simulations of HRTEM images. However the program have special modul „imagSim“ which possesses a lot of different possibilities of simulating the final image from calculated wave function. In the output field it's possible to define number of slices between outputs and also output directory. In the standard simulation mode the program calculates wave function for predefined slices, diffraction pattern and it's representation in real space.

4 Analysis of surface relaxation in $Fe_{45}Pt_{55}$ nanoparticles

4.1 Reconstruction of amplitude and phase from focal-series

In this chapter I'm going to focus on analysis of crystal structure of chemically disordered $Fe_{45}Pt_{55}$ nanoparticles. Here I will introduce new method of measuring of interplane distances and estimation of errors. This method is more accurate in comparison with common „linescan“ method described in [28]. The estimation of lattice parameter and surface relaxation was carried out.

In section „Experimental techniques“ I investigated chemically prepared $Fe_{45}Pt_{55}$ nanoparticles. $Fe_{45}Pt_{55}$ nanoparticles with average size of 8 nm have cuboctatru-nated shape. The nanoparticles were oriented predominantly along $\langle 100 \rangle$ direction parallel to the viewing direction. It was the most favorable position since the nanoparticles possess very flat (100) - facets. The orientation of nanoparticles along $\langle 110 \rangle$ - direction is less advantageous. In this orientation the nanoparticle has wedge-like shape which makes them mechanically unstable (see 3-dimensional model of NP in the next chapter). The nanoparticles itself were quite stable under electron beam irradiation and suitable for focal-series reconstruction. Focal-series acquisition of several nanoparticles in different orientations was carried out.

Another important advantage of EWR in comparison with conventional HRTEM imaging bases on the fact that displacements of atomic columns in common image can be due to the local changes in thickness [29, 30]. The contrast of atomic columns can change from bright to black with a sample thickness. Moreover the lattice spacing can change with a thickness and can be even larger close to the periphery of the

nanoparticle. These effects are pure imaging artifacts and has nothing to do with the real lattice change in nanoparticles because of physical reasons. For nanoparticles with cuboctahedral shape this problem arises. The cuboctatruncated nanoparticles exhibit very strong thickness variations due to their morphology. M.José Yacamán [31] has suggested to study the roughness of small Pt nanoparticles by local change of lattice spacing. The problem becomes more complicated since the contrast strongly depends on the defocus of objective lenses. The phase image is free from these artifacts since the projected potential i.e. phase strongly peaked at atomic positions. Additionally image simulations were performed to compare with the experimental results.

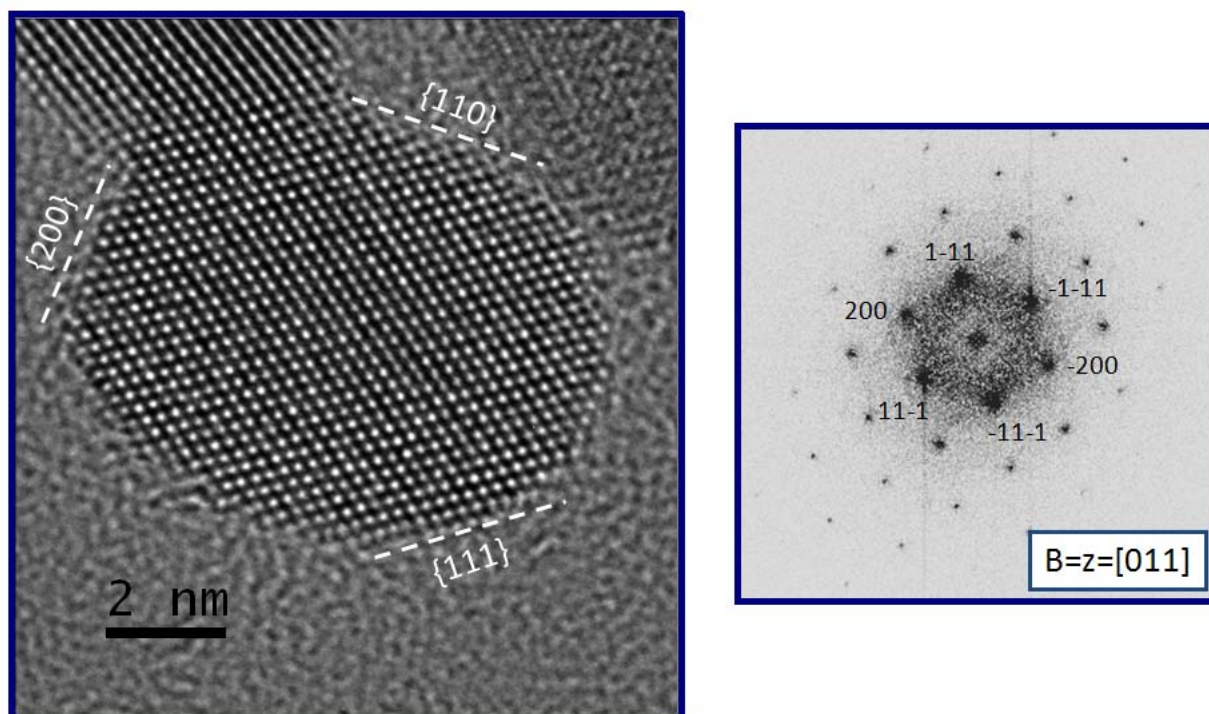


Figure 4.1: HRTEM image of FePt NP from focal series ser-22. The image was acquired close to the Lichte defocus. Different planes were indexed on the base of diffractogram (left). The contrast of diffractogram was inversed in order to enhance the visiability of Bragg reflexes.

Figures 4.1 and 4.2 show the HRTEM images of nanoparticles with corresponding FFT images. EWR and plane spacing analysis was performed on these nanoparticles. The nanoparticle from the series ser-22 is in $[011]$ zone-axis orientation, displaying

$\{111\}$ and $\{200\}$ facets. The nanoparticle from ser-29 is oriented along $[100]$ -zone axis, displaying $\{200\}$ -facets. The $\{111\}$ -facets become invisible in this orientation. In order to index different crystallographic planes the diffractogram was compared with corresponding diffraction map for fcc structure. Diffraction maps for different structures including fcc, hcp and bcc can be found in [8]. From the analysis of relative distances between reflexes and also angles the orientation of nanoparticle was determined. Analysis of intensities of reflexes shows that the nanoparticle is slightly tilted out of the zone-axis.

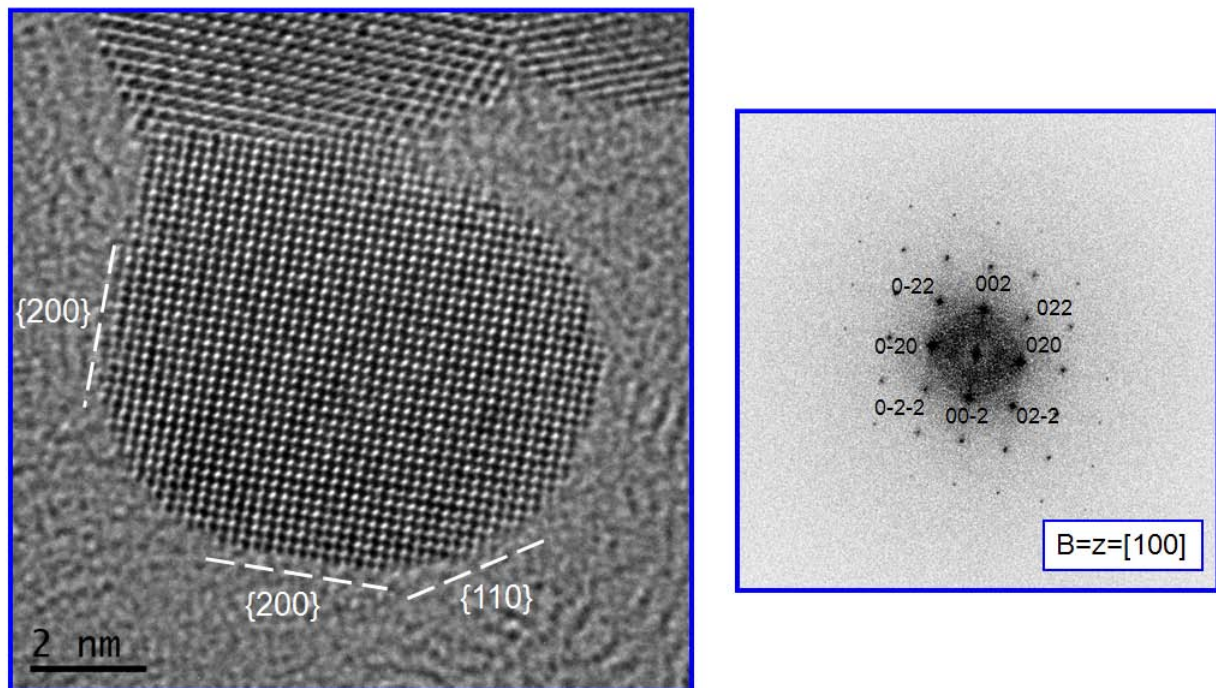


Figure 4.2: HRTEM image of FePt NP from focal series ser-29. The image was acquired in underfocus and by negative spherical aberration which makes the atoms appear as dark spots.

The formation of $L1_0$ structure with alternating layers of Fe and Pt atoms leads to the tetragonal distortion of the lattice (fct structure). The $L1_0$ phase can be formed in Fe_xPt_{1-x} alloys with close stoichiometric ratio of contributing components. In the case of $L1_0$ structure one should observe the (100) and (110) diffraction spots in diffractogram. For fcc structure they are extinguished due to the structure symmetry. However the careful analysis of intensities does not reveal the presence of additional

reflexes. Also the diffraction measurements on large ensemble of nanoparticles does not show any proof of $L1_0$ ordering.

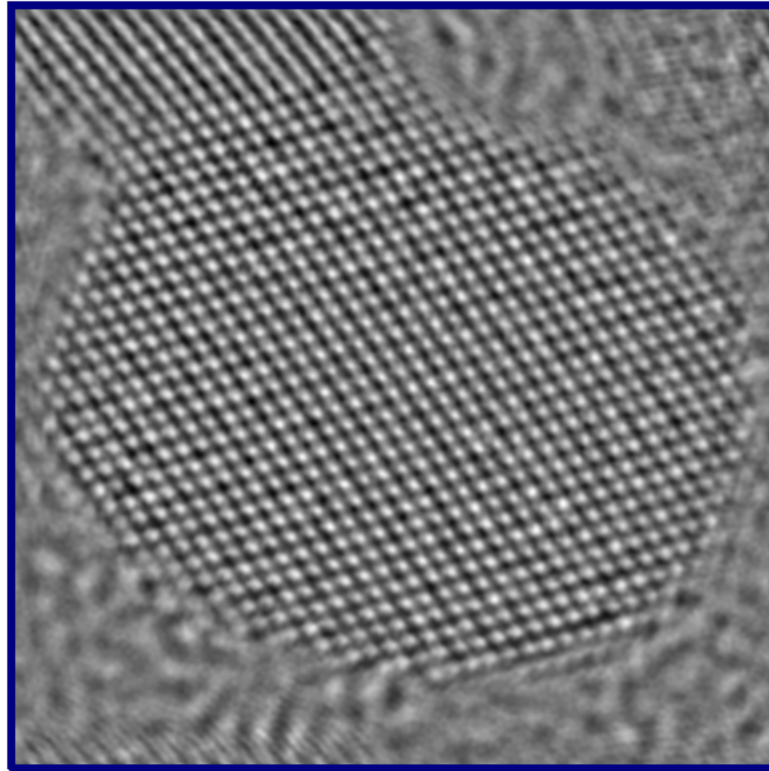


Figure 4.3: Reconstructed phase image from ser-22.

The focal-series were acquired under optimum microscope conditions. The measured value of spherical aberration was estimated to $-16.7\mu m$. The focal-series were recorded in Mh-magnification mode (1100 kx). The corresponding image discretization (sampling rate) was equal to $0.009064 nm/px$. The usual reconstruction of wave function with 20 images failed because of strong focal instabilities. During the focal acquisition of ser-29 the nanoparticle began to rotate at the end of focal series. The new reconstruction with corrected step size and only 13 images for ser-22 and 10 images for ser-29 was performed. The reconstructed phase image is displayed on figure 4.3. The small drift during the acquisition was corrected by Drift Compensation algorithm implemented in *TrueImage* software. Small fringes on the bottom right part of the phase image are artifacts of this algorithm. These fringes originate from the lattice image of nanoparticle from the top right part. At the end the residual aberrations were estimated and compensated.

4.2 Determination of positions of atomic columns

For analysis of interplane distances the reconstructed phase image was used. The positions of atomic columns were measured by using PPA software. First of all the Bragg filtering was applied. On the image 4.4 one can see power spectrum of phase image with circular masks. The Bragg filtered image is calculated as inverse FFT from the area surrounded with masks.

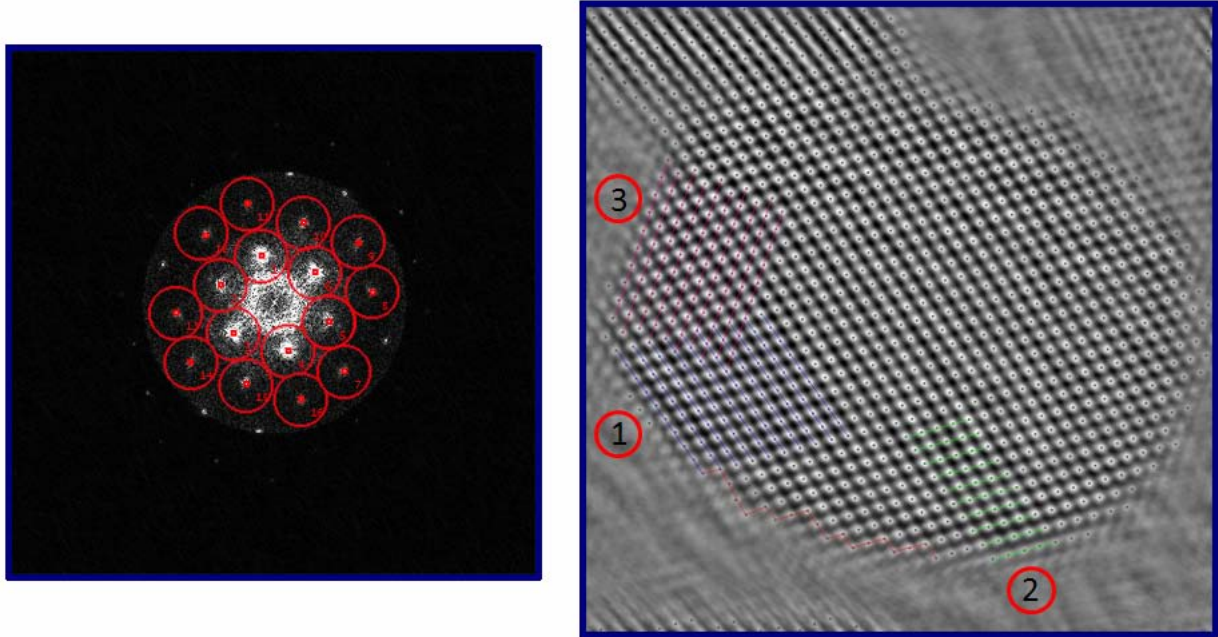


Figure 4.4: Power spectrum of phase image with filtering mask. All reflexes are enumerated. The central prominent area with high contrast on power spectrum correspond to the spatial frequencies reconstructed by EWR. The highest spatial frequency on the boundary of this area relates to the reconstruction limit. Crystalline reflexes just on this boundary were discarded by analysis. Some reflexes beyond the reconstruction limit are artifacts. They are not present if FFT of complex wave function is calculated. Bragg filtered phase image with pinpointed positions of atomic columns (right). Different facets used for analysis of surface relaxation are enumerated. For calculation of interplane distances the planes indicated with different colors were used. The red line shows typical *saw – tooth* atomic structure of $\{110\}$ -surface.

By filtering one can reduce noise. But on the other hand filtering produces some additional artifacts, i.e. the appearance of some „ghost“ atoms. By analysis of plane

spacing these spots were not regarded from comparison with experimental phase image. However interplane distances by sufficiently big masks should not be affected. Small shift of atomic columns due to the strain distribution or surface effects causes the shift of reflexes in Fourier space. By using of masks with relatively big area this shift should be included into calculation.

4.3 Calculation of interplane distances and estimation of errors

The analysis of plane spacings was carried out by using *Curve Fitting Toolbox* implemented in MATLAB. The interplane distances were calculated in the following way. First of all the atomic coordinates with sub-pixel resolution (0.01 px) were loaded. The points belonging to each crystallographic plane were excluded graphically. Afterwards these points were approximated with a linear regression, for example $y(x) = p_1 * x + p_2$. The parameters of fit were saved for further analysis. Then the parameters of the line perpendicular to the first plane were calculated. The slope of this line is $p_1^* = -\frac{1}{p_1}$, where p_1 - the slope of first fit (the first fit correspond to the outmost layer). To calculate the second parameter the crossover close to the middle of the plane was selected ($p_2^* = y - p_1^*x$, where (x,y)-coordinates of crossover). The line intersects the planes in some points. The coordinates of these crossovers can be easily calculated from the set of equations:
$$\begin{cases} p_1^*x_i + p_2^* = p_1^i x_i + p_2^i \\ y_i = p_1^i x_i + p_2^i \end{cases}$$
. Afterwards the plane spacings can be calculated subsequently as distances between these intersections. Finally interplane distances calculated in pixel units need to be multiplied with sampling rate (nm/px). This method is shown illustratively on the figure 4.5.

As a merit of error deviations of atomic columns from linear fit were used. For assessment of deviations root mean squared error was used (RMSE). As can be seen from figure 4.5 two subsequent planes contribute to the error of interplane distance. The resultant error was calculated from the law of error propagation.

There are several reasons of deviations of atomic columns from the perfect crystal structure. In the next chapter it will be shown that relative deviations up to 2.8% can originate from amorphous background. Local variations of chemical composition can

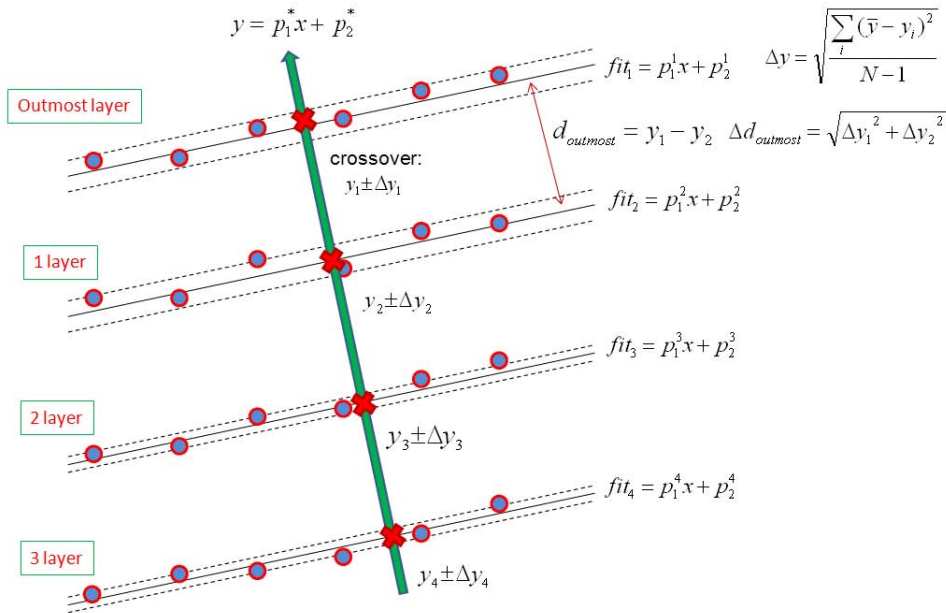


Figure 4.5: To the measurement of interplane distances and error estimation

also result in distortion of the lattice. The phase image shows us only two dimensional projection of the lattice. In other words the image of atomic column is averaged over all atoms in the column. Three dimensional atomic structure of material can be only revealed from different projections. Also some residual aberrations for example axial coma can „falsify“ the real atomic positions.

By measuring interplane distances I assumed that the fitting lines are approximately parallel. However it is far from reality. As it will be shown that noticeable deviations from parallelism become apparent already ten layers away from measured plane. Approximation of atomic positions with sub-pixel resolution is only mathematical trick to enhance the precision. The highest spatial frequencies of the object are simply damped due to resolution of CCD detector characterized by Nyquist frequency (half of reciprocal sampling rate). Also the rescaling of images towards decrease of sampling interval has no physical sense. Just simple substitution of pixel-resolution to the errorbar of plane spacing seems not to solve the problem because of pixel anisotropy. Summarizing all these ideas more careful analysis should be carried out in order to get real estimate of error.

4.4 Results and Discussions

Figure 4.6 shows interplane distance measured for different facets of nanoparticle from ser-22. The measured planes are shown on the figure 4.4. The atoms on the edges of nanoparticle belong to different crystallographic planes. They were excluded from calculation. For (111) as well as for (200) facets one can observe the expansion of lattice spacings close to the surface. For (111) - facet enumerated as 1 this increase can be identified only for outmost layer. Since for other planes no significant deviations can be observed. One can also observe unexpected jump of plane spacing for layer with number 5. This jump obviously situates outside of error range. Most probable explanation of this behavior would be Pt-rich layers. If one counts from the outmost layer the layers 5 and 6 should be Pt-rich. The Pt enriched layers comes to the expansion of plane spacing and apparently to distortion of the lattice. The big error bar for outmost layer can be observed almost for all measurements. There could be several explanations of this effect. From the one side atomic columns on the edge exhibit very low contrast. From mathematical point of view the uncertainty in positioning of maximum increases. On the other side the surface atoms are more active in comparison with the atoms inside the nanoparticle. Therefore the thermal fluctuations can smear out the real positions of atoms.

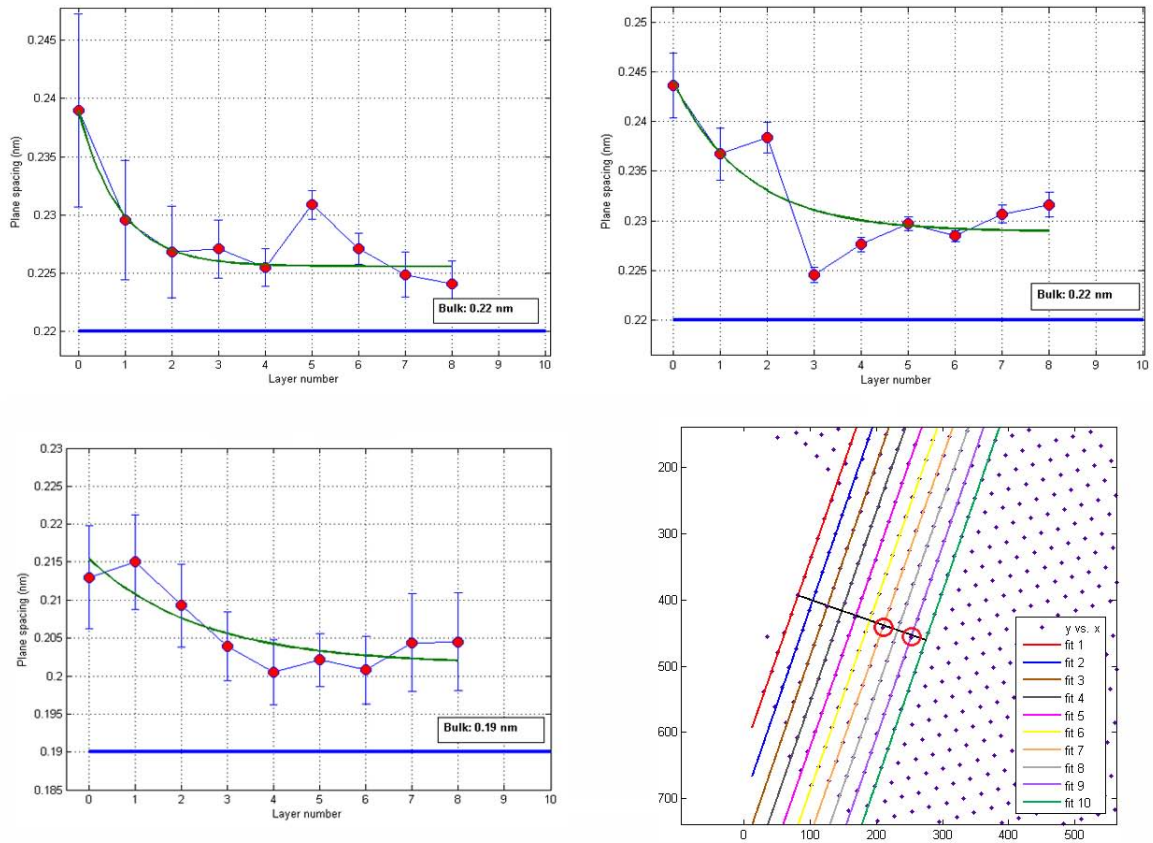


Figure 4.6: Measured interplane distances for different crystallographic facets of nanoparticle from ser-22. Top left and right graphs belong to facets 1 and 2 ((111) - planes, see figure 4.4) correspondingly. The bottom left graph was measured on facet 3 ((200) - planes). The layer marked with number 0 designates outmost layer. Solid blue lines represent bulk values of interplane spacing for corresponding planes. Fitting with exponential function $y = a \cdot \exp(-b \cdot x) + c$ is shown with green line. The bottom right figure shows lattice spacing analysis for facet 3. Blue points correspond to atomic positions. The fitting lines are represented with different colors. The black line is perpendicular to the first fit with intersection in the middle of the plane. Red circles indicate deviations of this line from the crystallographic direction. This implies that the planes are not really parallel.

This effect is very pronounced on the image 4.7. Afterwards the measured values of plane spacings were compared with those for bulk material. For cubic structure interplane distances can be calculated in the following way:

$$d_{hkl} = \frac{a}{\sqrt{h^2 + k^2 + l^2}} \quad (4.1)$$

, where a - lattice parameter, (h,k,l) - miller indexes of corresponding plane. As a lattice parameter for bulk $FePt$ alloy the value of 3.81 nm was taken [28]. The corresponding values for different planes are indicated on figures 4.6 and 4.8 with solid lines. Apparently one can see two different effects: increase of lattice parameter for outmost layers and overall increase of lattice parameter in comparison with bulk. The values of surface relaxation and lattice expansion in comparison with bulk were quantitatively estimated as follows:

$$\delta_s = \frac{d_{max,hkl} - d_{hkl}}{d_{hkl}}, \quad \delta_{bulk} = \frac{d_{hkl} - d_{hkl,bulk}}{d_{hkl,bulk}} \quad (4.2)$$

, where d_{max} is maximum measured plane spacing, d_{hkl} - mean value calculated for data points where plane spacing is almost constant (saturation region), $d_{hkl,bulk}$ - bulk value for corresponding plane on basis of 4.1. All values are given in the table 4.4.

ser-22	δ_s	δ_{bulk}
facet 1 (111)	5.3%	3.2%
facet 2 (111)	6.5%	4.0%
facet 3 (200)	6.1%	6.4%
ser-29	δ_s	δ_{bulk}
facet (200)	12.2%	4.1%

Table 4.1: Calculated values of surface relaxation and expansion of lattice parameter

For facets 1 and 2 the values of surface relaxation differ almost in 1%. This difference can be due to small residual 2-fold astigmatism presented in the image. 2-fold astigmatism results in small distortion of the image in different directions. The increase of plane spacing can be calculated as averaged value for both (111) - facets. It results in $5.9 \pm 0.6\%$. It is comparable with the value measured for (200)-facet. No

significant difference in surface lattice spacings of different crystallographic planes is observed. However for ser-29 this value is extraordinary high and results in 12.2%. In order to clarify this „strange“ behaviour more detailed error analysis was carried out. The measured surface relaxation is determined by the error of d_{hkl} . As it was already mentioned the error for outmost plane spacing can be relatively big. As one can note from eq. 4.2 δ_s depends from $d_{max,hkl}$ and d_{hkl} . The maximum value of uncertainty estimated by using the method of error propagation gives the deviations of 6.6%. From this it follows that surface relaxation is the same for both nanoparticles. Analysis of another facets for nanoparticle from ser-29 does not reveal any detectable increase of lattice parameter for outmost layers.

It was already proposed that the spacing between the shells decreases exponentially with shell numbers [32]. This dependence was shown for *FePt* icosahedron nanoparticles. According to this idea the fitting of spacing for different planes was carried out. As a theoretical model the exponential function $a \cdot \exp(-b \cdot x) + c$ was used. The goodness of fit was estimated by means of adjusted R-square. Quite good match of theoretical model with experimental data was confirmed for facet 1 (111) from ser-22 and facet (200) from ser-29. For other facets the proposed approximation does not give any good match. The reason could be high strain density because of inhomogeneous distribution of *Fe* and *Pt* atoms. For facet 1 (111) the fitting curve is $d_{111}(n) = 0.2256 + 0.01339 \cdot e^{-n/0.88}$. The exponential function has strong increase only for two outmost layers and achieves saturation already for third layer. This constant value gives us for (111) - spacing the value of 0.2256nm. It results in 6% expansion of lattice in comparison with icosahedron structure (0.2113nm). From the graph 4.8 one can see small layerwise oscillations of spacing for layers 1-6. This oscillations are typical for bulk materials. However the calculation of interplane distances through the nanoparticle can not confirm this phenomena. The errorbar exceeds the magnitude of these oscillations.

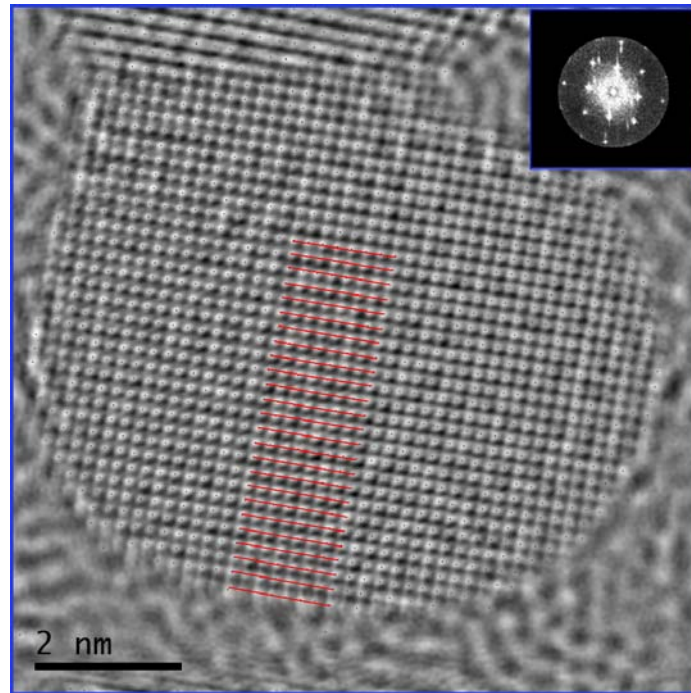


Figure 4.7: Reconstructed phase image from focal series ser-29. The estimated positions of atomic columns are shown. The inset in the left top corner is FFT of complex wave function. The planes emphasized with solid red lines were used for analysis of surface relaxation.

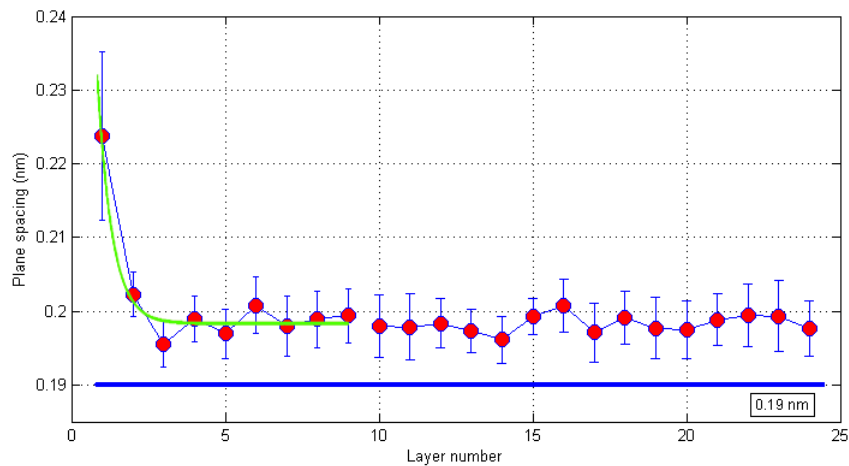


Figure 4.8: Measured interplane distances for (200)-planes through the nanoparticle from ser-29. Blue line correspond to the bulk value. Green line is fitting curve.

The lattice parameter was also measured by means of linescans. The goal was to estimate more precisely the overall lattice expansion. The linescans used for analysis are shown on the pictures 4.9. The measured values are included in the tables 4.2 and 4.3. The lattice expansion up to 4.4% in comparison with bulk is observed.

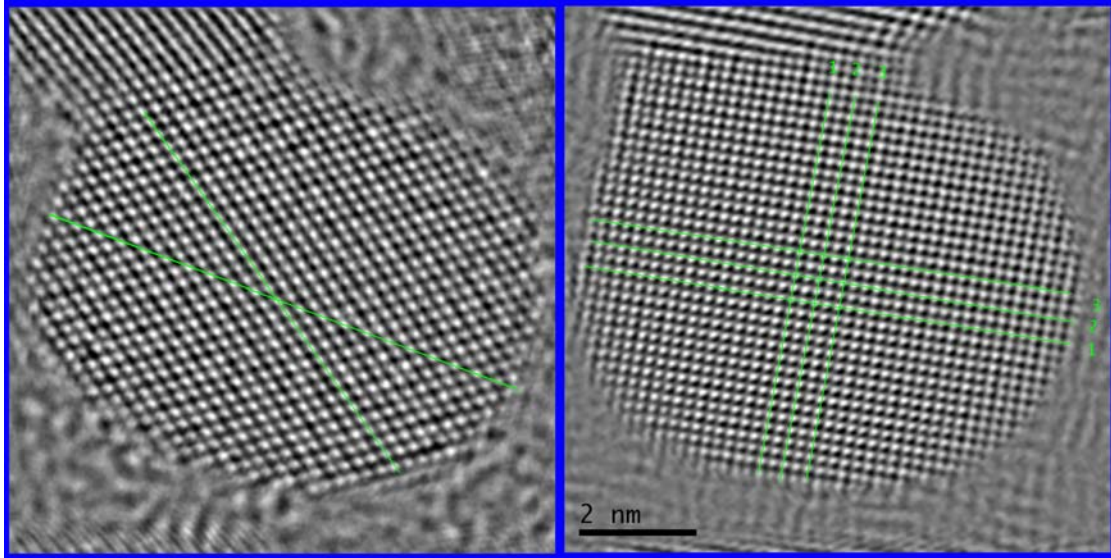


Figure 4.9: Analysis of phase images by means of linescans. Linescans are shown with green color. For particle from ser-29 (right) different linescans are enumerated. The scalebar belongs to both images.

	Δd (px)	d (plane spacing, nm)	a (nm)
linescan 1 (111)	27.17	0.1331	0.3994 ± 0.0164
linescan 2 (100)	44.40	0.3996	0.3996 ± 0.0115
\bar{a}			0.3995 ± 0.0100

Table 4.2: Lattice parameter measured for different directions by means of linescans (ser-22)

The exit-wave function is formed by dint of transmission of electron wave through the crystal. The image of atomic columns is averaged over all atoms in the column. Every shift of atoms from the crystal order contribute to the final phase image. The phase image gives us only two dimensional projection of crystal lattice. However surface relaxation is three dimensional effect. The expansion of lattice parameter for outmost layers was observed for (111) as well as (200) crystallographic facets. On

	Δd (px)	d (plane spacing, nm)	a (nm)
linescan 1 (200)	21.98	0.1978	0.3956 ± 0.0208
linescan 2 (200)	21.95	0.1976	0.3951 ± 0.0166
linescan 3 (200)	21.93	0.1974	0.3947 ± 0.0175
linescan 1 (020)	22.06	0.1986	0.3971 ± 0.0102
linescan 2 (020)	22.03	0.1983	0.3966 ± 0.0235
linescan 3 (020)	22.06	0.1985	0.3971 ± 0.0135
\bar{a}			0.3960 ± 0.0072

Table 4.3: Lattice parameter measured for different directions by means of linescans (ser-29)

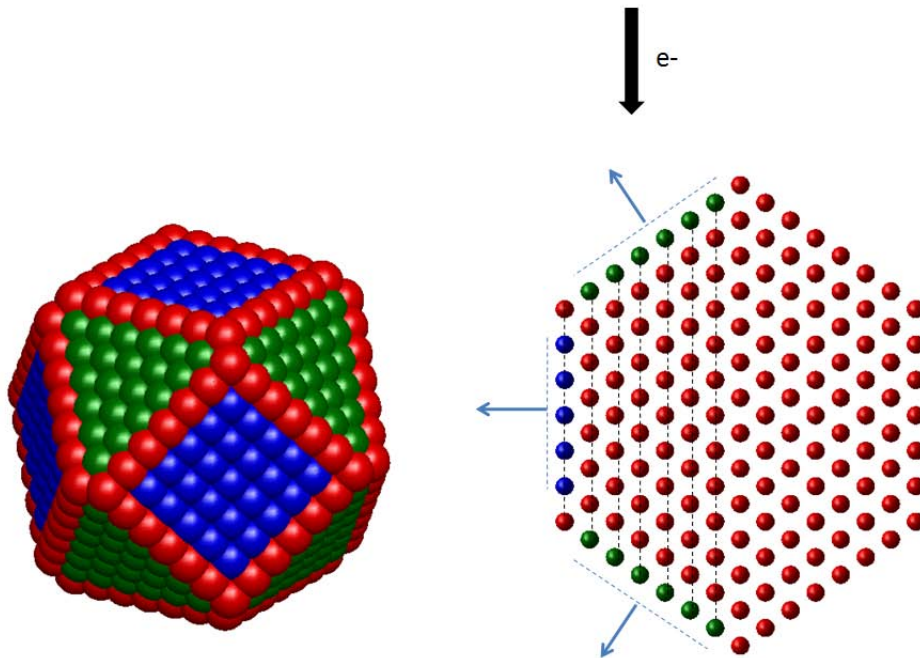


Figure 4.10: Surface relaxation in three dimensions. On the left hand side is the model of perfect cuboctahedron (fcc). (100) and (111) facets are shown with blue and green color respectively. Edges are displayed with red color. On the right hand side is projection of this model along (110) direction. The electron beam propagates top-down. The surface expansion is illustrated with arrows. Atomic columns along electron beam are displayed with dashed lines.

two dimensional projection the contributions from different facets are intermixed. This effect is elucidatory explained on the figure 4.10. From this orientation the average positions of atomic columns are shifted towards (100) plane. In this regard the real magnitude of surface relaxation for (100) planes should be bigger. In this connection only tomography can shed the light on surface structure of nanoparticles. Unfortunately the tomography with atomic resolution is not possible so far [33].

5 Clarification of the structure of $Fe_{45}Pt_{55}$ nanoparticles on the base of simulations

5.1 Building of the model

In order to compare the experimental results with image simulations, we built the atomic structure models of various nanoparticles. Images show only two dimensional projection of nanoparticle through direction of electron beam propagation. Thereby three dimensional shape of nanoparticle always leaves room for assumptions. Additional focus-series reconstructions along different crystallographic directions can cast light upon atomically resolved three dimensional structure of nanoparticle. However $Fe_{45}Pt_{55}$ nanoparticles usually are cuboctahedrons elongated along $\langle 100 \rangle$ - direction. On the picture 5.1 one can see perspective projection of 3-dimensional view of nanoparticle used for simulations. On the picture 5.2 the view along direction of propagation of electron beam is shown. The model was visualised by AtomEye atomistic configuration viewer.

The whole model is enclosed in simulation box which is shown with solid black color. The model of nanoparticle was created as fcc-cluster with cuboctahedral shape by using algorithm implemented in Generator-software. I used cuboctatruncated shape of fcc-cluster. For building of the current model I used two parameters [34]. The first parameter L describes the size of fcc-cluster and equals the number of unit cells along three perpendicular directions commensurate with lattice parameter. By building of the current model I set L to 20. The second parameter M describes degree of truncation. In other words by changing this parameter one can define how

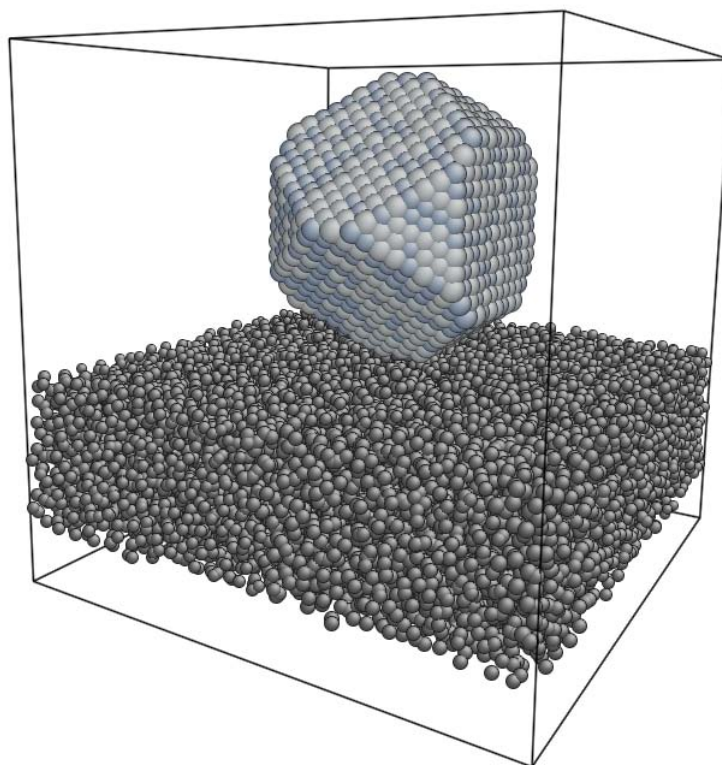


Figure 5.1: 3d-view on the model of nanoparticle used for simulations

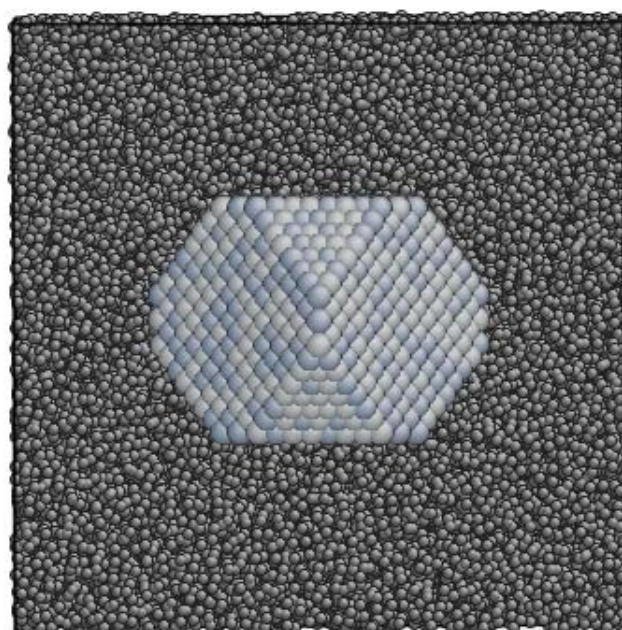


Figure 5.2: 3d-view on the model along electron beam propagation direction

many planes of fcc-cluster are truncated perpendicular to the $\{111\}$ - direction. The nanoparticle consists of 1411 iron atoms and 1746 Pt atoms. The iron and platina atoms were distributed randomly in nanoparticle in proportion of 45% to 55%. In 3d-view of nanoparticle the iron and platina atoms are represented with different colors. For building of the model of Cuboctahedron the bulk value of lattice parameter $a = 3.81 \text{ \AA}$ was used. Finally the nanoparticle was rotated in order to match the $[110]$ - crystallographic direction with the z-axis of supercell or simulation box. In this case the z-axis of simulation box correspond to the direction of propagation of electron beam.

In order to make the simulations more realistic the model of amorphous material was built. The model of amorphous material was built according to the recipe provided in the article [35]. First of all I created the slab populated with carbon atoms according to the structure of diamond. The thickness of the slab was equal to 2.5 nm and the length and the width of the slab match the dimensions of supercell box. The lattice parameter of this structure was recalculated in order to match the density of amorphous material ($\approx 2.0 \text{ gr/sm}^3$, [36]). In order to get the amorphous structure the order in the final atomic model should be destroyed by random shift of atomic coordinates. By small displacements we should still observe some order in the final structure. In order to see how big should be this displacement in order to get really amorphous structure I performed simulations only with the slab of amorphous carbon. By maximum displacement of three fourth of bonding length (0.186 nm) the order in the final simulated image dissappear. In this case one can observe typical „speckle“ pattern as in experimental images of amorphous film. Another possibility to get this „speckle“ is to increase the thickness of amorphous material by relative small random displacements of atoms. But in this case the simulation time increases as well. Overall the model contains 25329 atoms. The slab of amorphous material contains 22172 carbon atoms.

5.2 Simulations of the phase image

For simulations with multislice method I used 70 equal slices, so the thickness of one slice correspond to one half of bonding length ($\approx 1.32 \text{ \AA}$). The size of

probe array corresponding to the resolution of simulated image was equal to the resolution of experimentally reconstructed phase image (1024x1024). The dimensions of simulation box were adjusted to the sampling rate of experimental image ($Resolution X, Y = \frac{Size\ of\ Sim.\ Box}{1024} \approx sampling\ rate_{exp} \approx 0.009nm/px$).

The microscope parameters were selected close as possible to experimental conditions ($U = 300kV$, $C_s = -13\mu m$, $C_c = 1.28mm$, $\Delta E = 0.3eV$ $a = 0.1mrad$). The final phase image was simulated from the wave function corresponding to the last slice. The phase image was simulated by Scherzer defocus conditions and by using objective aperture. The size of objective aperture was adjusted to the reconstruction limit of experimental focus series (0.09 nm).

In order to investigate the effect of crystal tilt on positions and intensities of atomic columns the simulations with tilted model were carried out. The software does not use „slice shifting“ based on inclining of propagator functions between slices. Therefore the complete model was tilted in simulation box. The rotating axis lied in-plane and parallel to [001]-direction of nanoparticle. The nanoparticle was inclined by 5, 10 and 15 mrad with respect to the z-axis of simulation box.

5.3 Results and discussions

On the picture 5.3 one can see simulated phase image of the nanoparticle. The atomic columns in the middle of nanoparticle seem to have low contrast in comparison with atomic columns close to the edge of nanoparticle. This contrast reversal can originate from dynamic behavior of scattered electron beam. In the direction of electron beam propagation the nanoparticle has wedge-like shape. It means that the thickness increases from the edge to the middle part. On the edge the model has only one atom whereas in the central part atomic columns consist of maximum 17 atoms which correspond to the thickness of approx. 4.77 nm. By large thicknesses atomic columns approach extinction length out of the linear approach. In this case the WPO approximation is not valid any more and one should take multiscattering effects into consideration. The WPOA application range can not be estimated directly from simulated phase image because it's strongly depends on local composition of elements. However the thickness range to which WPO approximation is still valid

can be extended by small crystal tilts. On the figure 5.4 the simulated phase image by 15 mrad ($\approx 0.85^\circ$) tilt out of the zone-axis is displayed.

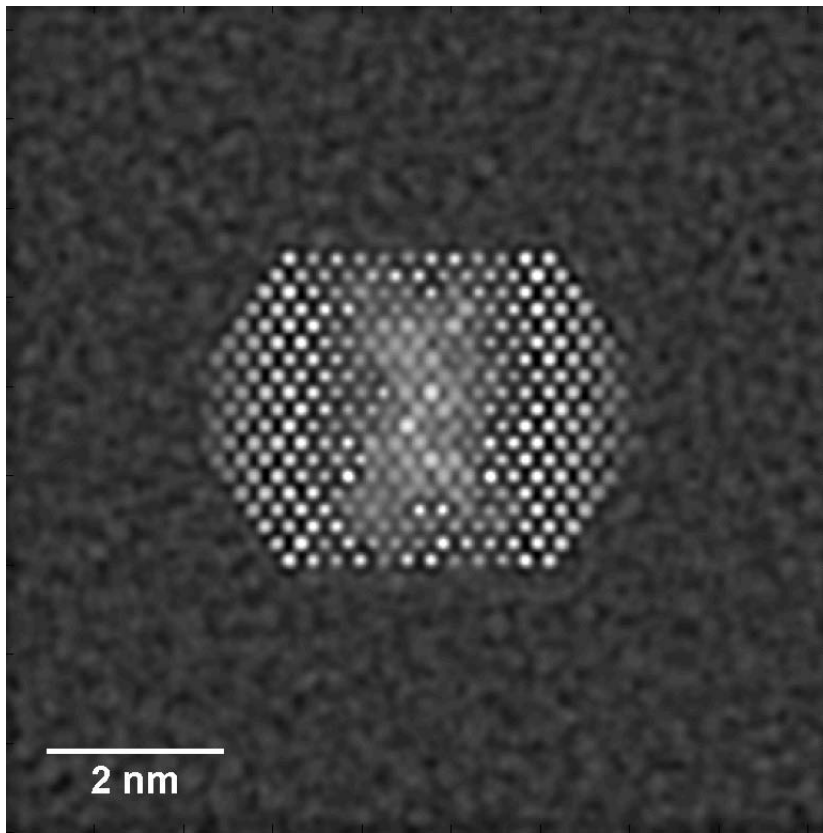


Figure 5.3: Simulated phase image

By tilting of the model the atomic columns in the middle got higher contrast as against the untilted sample. It is the most probable explanation, why in the phase image reconstructed from focal-series ser-22 this typical contrast reversal is not really expressed. Nevertheless it's quite common situation that all atomic columns look approximately the „same“ . Only in very rare cases it's possible to find nanoparticle where atomic columns exhibit contrast reversal with thickness variations. On the picture 5.5 is one of this seldom cases. Why the nanoparticles very frequently look a little bit tilted? There are several reasons for that. The surface of supporting carbon film has always some height variations. Moreover under long exposures the carbon film can „flow“ under the nanoparticle and change the local structure. The thermal drift can have dramatic influence on the orientation of nanoparticle. It's especially crucial by focal-series acquisition. The nanoparticle in $[110]$ -orientation should be

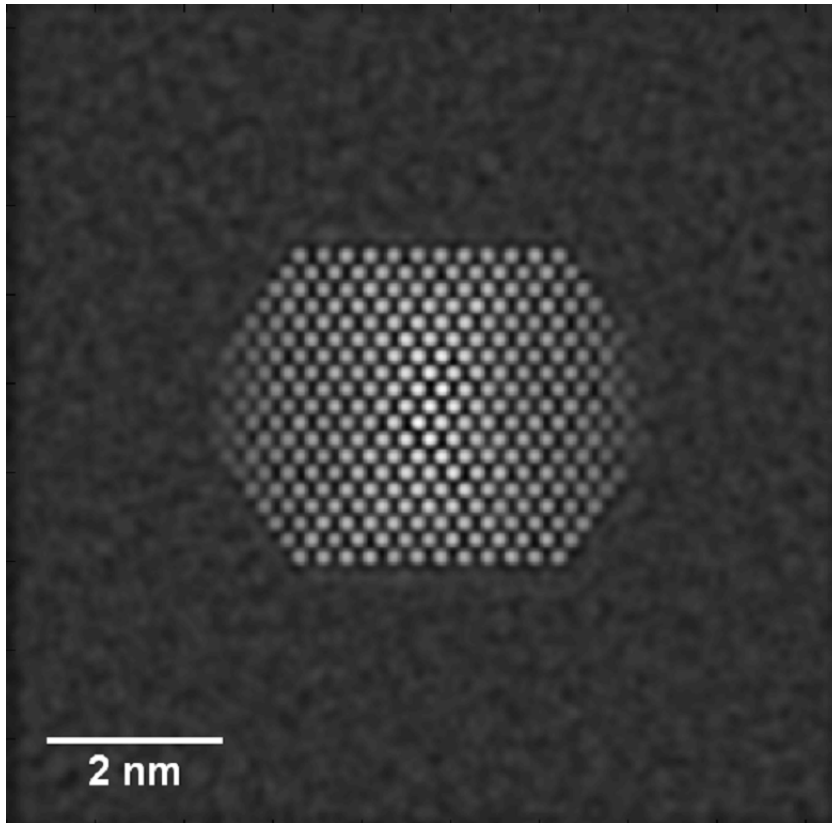


Figure 5.4: Simulated phase image of the model tilted by 15 mrad along the rotation axis parallel to $[001]$ crystallographic direction

extremely unstable in this regard. As one can see from figure 5.1 the nanoparticle is „sitting“ only on several atoms and can be easily tilted.

In simulated phase image (figure 5.3) one can see that neighboring atomic columns exhibit different contrast. Even atomic columns which have the same amount of atoms show different intensities. This contrast difference can have origin of different chemical composition of atomic columns i.e. Z-contrast. In other words the atomic column with higher Z-number should also possess higher contrast. In order to verify these results the mapping for each atomic column with integrated Z-number was carried out. The part of simulated phase image together with Z-map are displayed on the figure 5.6. The spots numbered as 1 and 3 have less prominent phase maxima in comparison with spots 3 and 4. However first pair of maxima correspond to atomic columns with larger Z-number (on the figure Z-number correspond to color from color scheme). This behaviour is no longer in accordance with weak-phase-object approximation (WPOA). However for columns marked from 5 to 9 one can

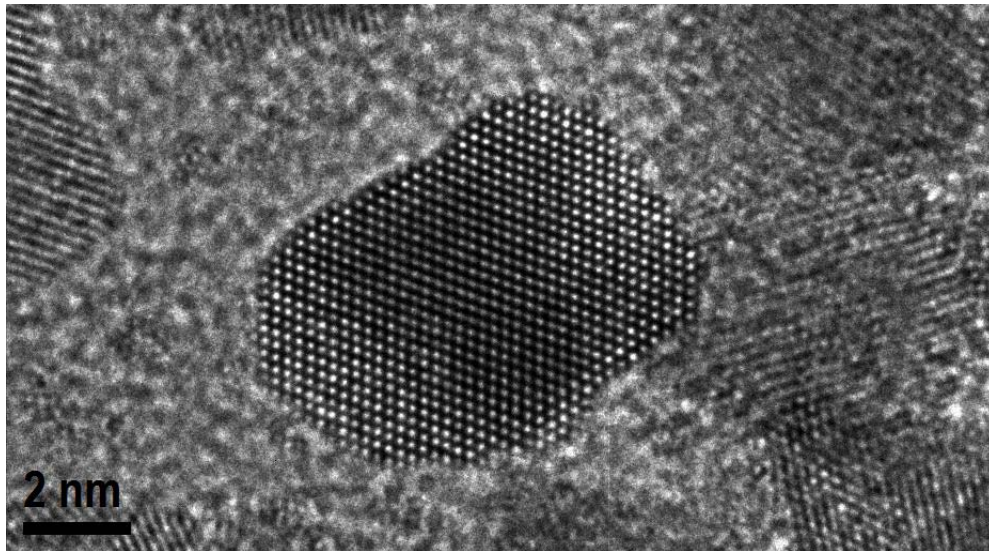


Figure 5.5: HRTEM micrograph of $Fe_{52}Pt_{48}$ nanoparticle recorded in National Center of Electron Microscopy (NCEM). Individual atomic columns show typical contrast variations from negative to positive contrast due to extinction behavior of electron beam. The nanoparticle situates very close to the zone axis [110] which makes contrast inversion very expressed. For usual HRTEM images as for phase images this effect should be observed as well. It can be argued with the fact, that within the framework of WPOA the intensity is still proportional to the phase of exit-wave. The micrograph was kindly provided by Zi-An Li (Universität Duisburg-Essen)

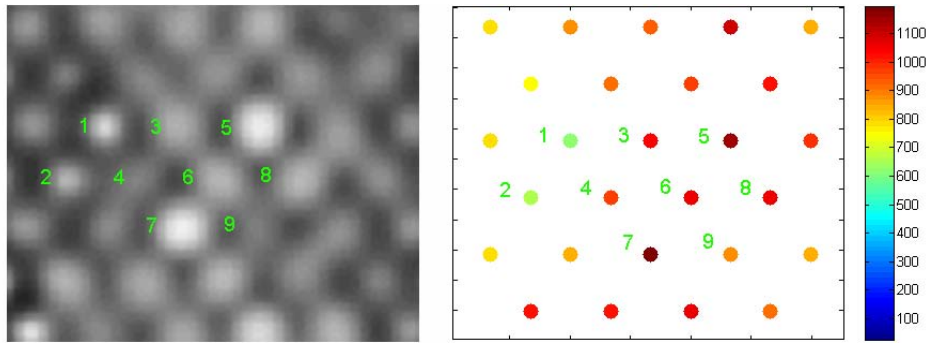


Figure 5.6: Z-mapping. On the left hand side the central part of simulated phase image. On the right hand side z-map. The positions of atomic columns are marked with different colors corresponding to their integrated Z-number. The colormap used for mapping is also provided. The colormap is calibrated in Z-number. The direct comparison can reveal some discrepancy between intensities and Z-number.

see completely different situation. The maxima of intensities seem to correlate with Z-number distribution. In order to clarify this „strange“ behaviour the simulation of the same nanoparticle but without amorphous film was carried out. The repeated comparison of column intensities with Z-map does not reveal any correlation. It means that observed coincidence was occasional and was produced by amorphous layer.

For tilted sample the contrast between neighboring atomic columns decreases. This effect is illustrated on the figure 5.7. From linescans it is clear that the chemical sensitivity of phase image decreases by slight tilts out of the zone-axis. This fact demands to proceed experiments under very stable conditions. The focal-series acquisition by usual 1s exposure takes approx. half a minute. During this time the motion of nanoparticle is constantly occurring. And it makes analysis of phase image very complicated. However the exit-wave reconstruction with reduced number of images (2 or 3 images) can help on this point.

After simulation the positions of atomic columns were determined. By using Bragg filtering the area covered by circular masks in Fourier space was selected big enough to reduce filtering artifacts. The positions of maxima of intensities were defined from fitting of bright spots with quadratic function with sub-pixel resolution. Afterwards the positions of projected atomic columns were compared with positions of estimated ones. Figure 5.8 shows zoom in part of simulated image near the edge of

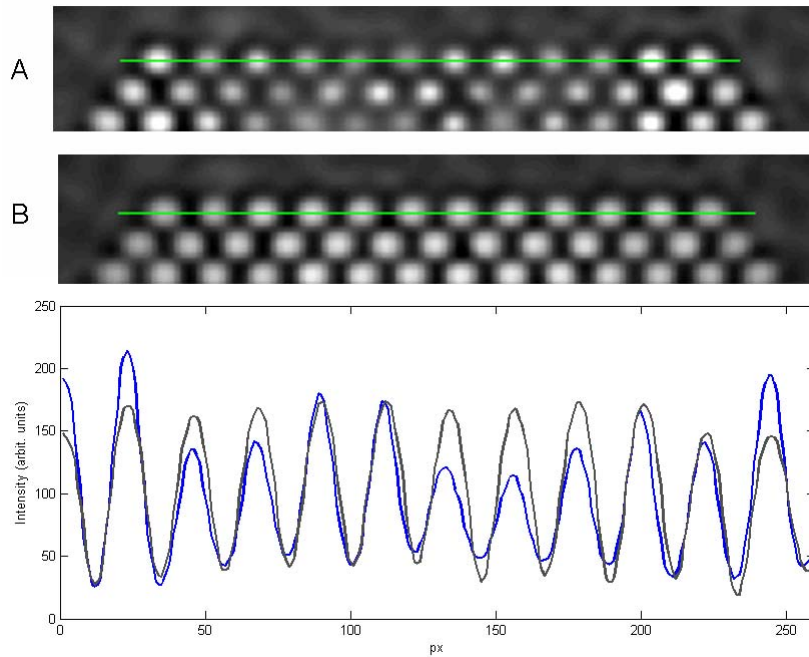


Figure 5.7: a) part of simulated image without tilt. The direction of line scan is indicated with green solid line. The width of line scan was equal to 5px. The pixel intensities were integrated within width of linescan. b) the same area of simulated image with tilt (15 mrad). Below two linescans are imposed one on another. The blue line correspond to linescan A. The brown line to linescan B. The difference between maxima of intensities i.e. phase contrast become smaller by small tilting

nanoparticle. One can see relative big deviations of fitted maxima from projected atomic columns positions. These deviations can originate from amorphous material. In order to check this idea the simulations of the same nanoparticle but without „supporting“ amorphous film were carried out. In this case all simulations parameters and also parameters of lattice points determination remained the same. The same part of simulated phase image is presented on the picture 5.9

The qualitative analysis of simulated images shows that deviations decrease when simulations are performed without amorphous film. Only for atomic columns close to the (110)-edge the deviations are still relatively big. They can originate from comparatively low contrast due to only several atoms in these atomic columns. To analyze quantitatively these deviations the interplane distances for (111) - planes were measured. The interplane distances were measured in the same way as for

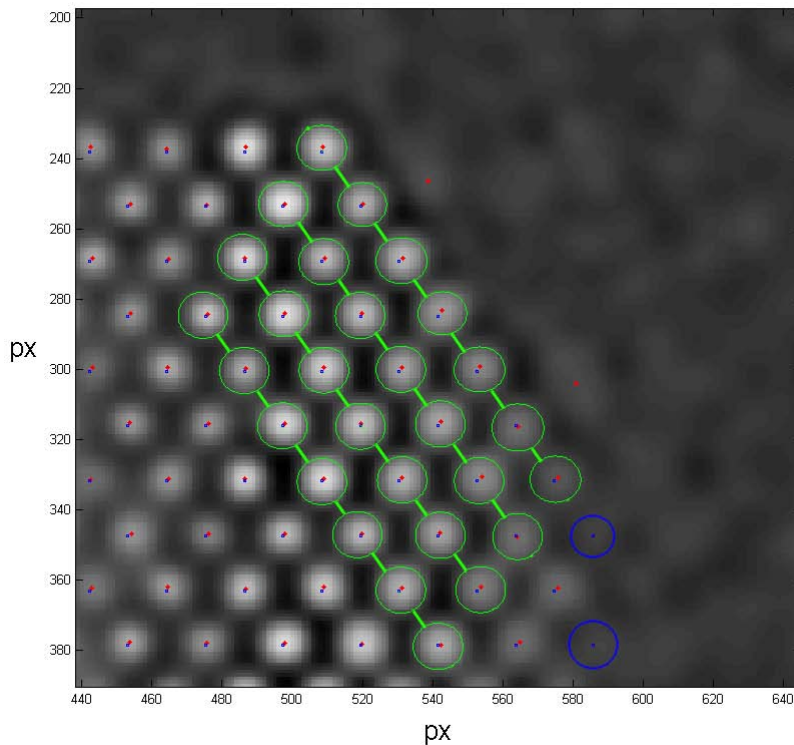


Figure 5.8: The part of simulated phase image zoomed in near the edge of nanoparticle. Red points correspond to maxima of intensity. Blue points are positions of atomic columns projected on the plane perpendicular to electron beam propagation. Green solid lines show (111)-planes used for analysis of interplane distances. The program did not recognize some bright „blobs“ as valid atomic columns because of low signal-to-noise ratio. These positions are highlighted with blue circles

experimental phase images. On the figure 5.10 one can see plane spacings for three (111) - layers including the outmost layer.

Afterwards the calculated interplane distances were compared with theoretical one. The largest deviation was observed for the second layer and was estimated to 2.8%.

By analysis of simulated phase image I have also paid attention on one interesting phenomena. By peaks determination the program could not recognize some bright spots as valid atomic columns. The maximum intensity of these spots was below estimated threshold value and comparable with background signal. In order to see

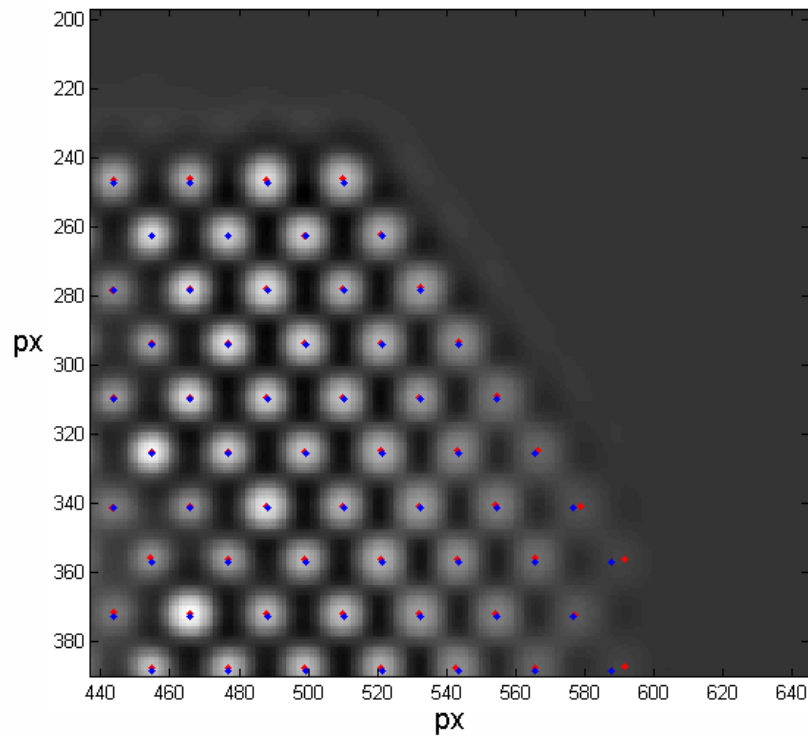


Figure 5.9: The part of the phase image simulated without amorphous carbon

this effect more clear the contrast of simulated image was enhanced (see figure 5.11). The atoms at some places seem to be „ missed“ . In literature this effect is known as missing-row reconstruction of $\{110\}$ planes [37]. Under this reconstruction the $\{110\}$ surface obtains so called „saw-tooth“ structure. However the contrast of atoms on the edge can be enhanced by changing defocus conditions. Only after analysis of focus-series it's possible to make some conclusion about atomic structure of the surface. In the current model the atomic columns on (110) -edge of nanoparticle consist only from one atom (see figure 5.1) and therefore the phase contrast is quite low. From the physical point of view this situation seems to be very unrealistic. These atoms should possess low coordination number which makes them very unstable.

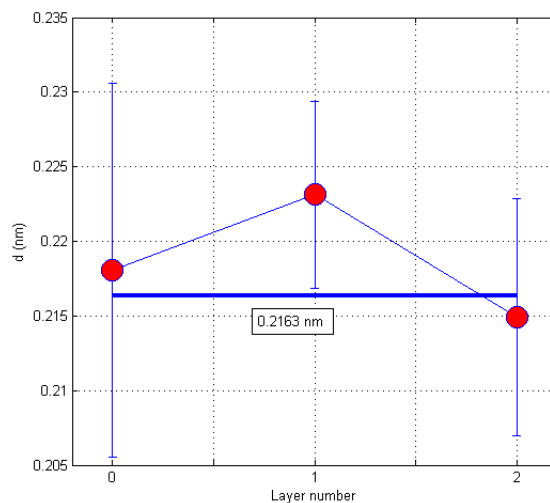


Figure 5.10: Plane spacings measured for first three outmost layers. The solid blue line is theoretical value for (111) plane spacing ($a_{111} = a/\sqrt{3}$)

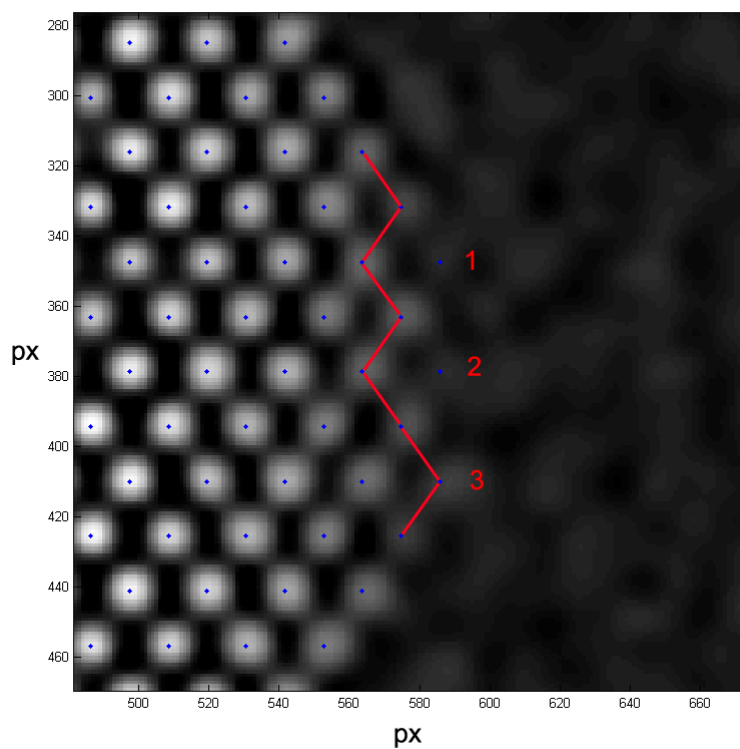


Figure 5.11: Part of simulated phase image with enhanced contrast. The atoms on the edge of nanoparticle are enumerated. Solid red line connects the points recognized as valid atomic columns

6 Analysis of morphology and structure of gold nanoparticles

6.1 Analysis of HRTEM and phase images of gold nanoparticles

As it was already mentioned I investigated Au nanoparticles by means of HRTEM and EWR through focal-series. The EWR was carried out on small Au nanoparticles with mean diameter of 5 nm. The focal-series was acquired on *Titan 80 – 300 TEM* under optimum imaging conditions and sufficiently small thermal drift. However small Au nanoparticles are quite unstable under electron beam. Even at small acquisition time the nanoparticles begin to rotate and change their position. The local structure due to surface diffusion of gold atoms changes as well. In general 11 exit-wave reconstructions were carried out. From them only one was successful. Also HR-STEM experiments did not give any satisfactory results. One possible way out to stabilize the nanoparticles would be to cover them with a thin layer of amorphous carbon. In such a way the nanoparticles will be sealed between amorphous layers. Unfortunately due to time limitation these experiments have not been done in frame of my diploma work.

Figure 6.1 shows the HRTEM image of multitwinned Au nanoparticle. This twinning structure with five-fold symmetry is typical for nanosized noble materials like Au, Ag and Pt and their alloys. Si and Ge nanoparticles also possess often multitwinned morphology. In literature this structure is known as decahedron structure. It consists of five tetrahedron parts with fcc - structure. This arrangement of atoms can be explained by the highest possible packing density by filling of space with tetrahedrons [38]. However the five - fold symmetry is not crystallographic because

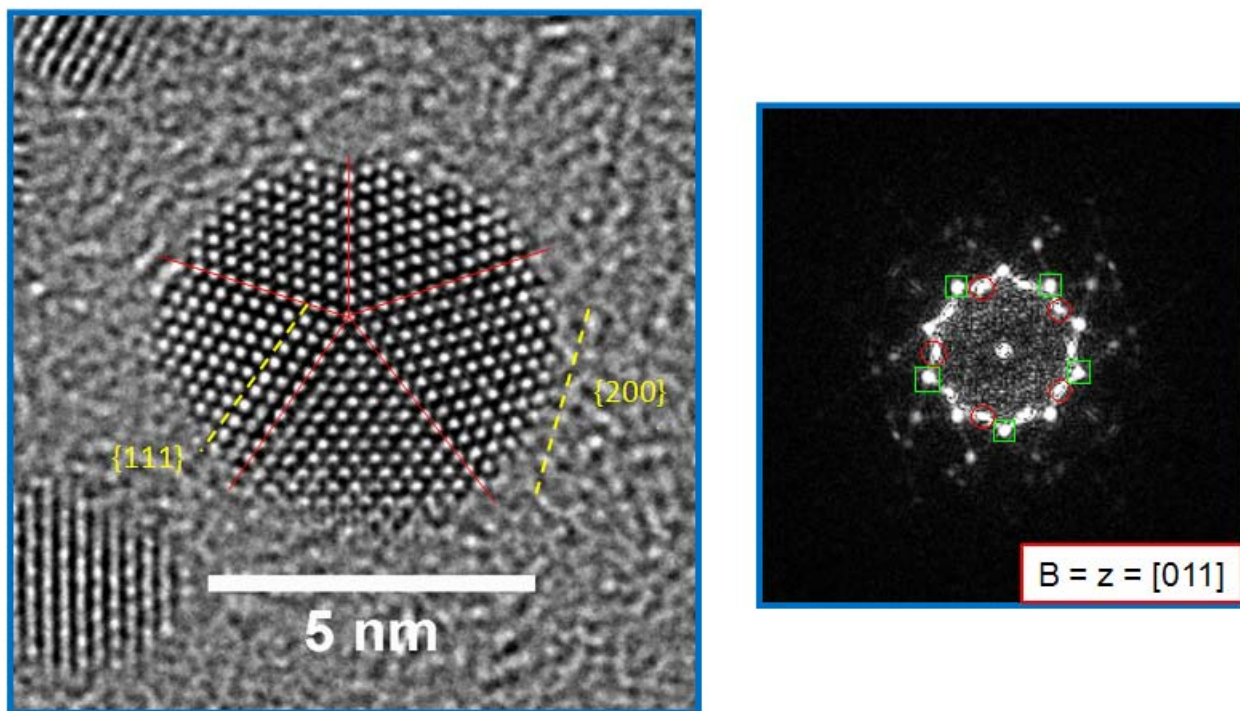


Figure 6.1: Left HRTEM image of a typical 5 nm Au nanoparticle with multitwinned structure. The twinning planes are displayed with red lines. The particle owns five-fold symmetry. The particle is viewed along five-fold symmetry axis $[011]$ which is congruent with a crossover of the $\{111\}$ twinning planes. Right the Fourier transform of the HRTEM image is shown. The five-fold symmetry can be easily recognized. The reflexes labeled by green squares belong to the $\{200\}$ - planes. The reflexes labeled by red circles correspond to the $\{111\}$ - planes. The equivalent planes are also schematically shown on the HRTEM image.

one can not cover the plane with regular pentagons. The mismatch becomes apparent in difference between angles of crystallographic planes. In fcc - structure the angle between adjacent $\{111\}$ faces is 70.53° . For decahedron this angle equals 72° which results in 1.47° solid-angle deficiency. It leads to intrinsic strain and distortion of the lattice [39]. As it was shown in PhD - thesis of Olga Dmitrieva [40] that the distance between neighboring atoms in $\{200\}$ planes is $\approx 5\%$ greater in comparison with the perfect fcc-structure.

The interplane distances were measured according to the method described in the previous chapters. First of all the nanoparticle image was divided into five non-

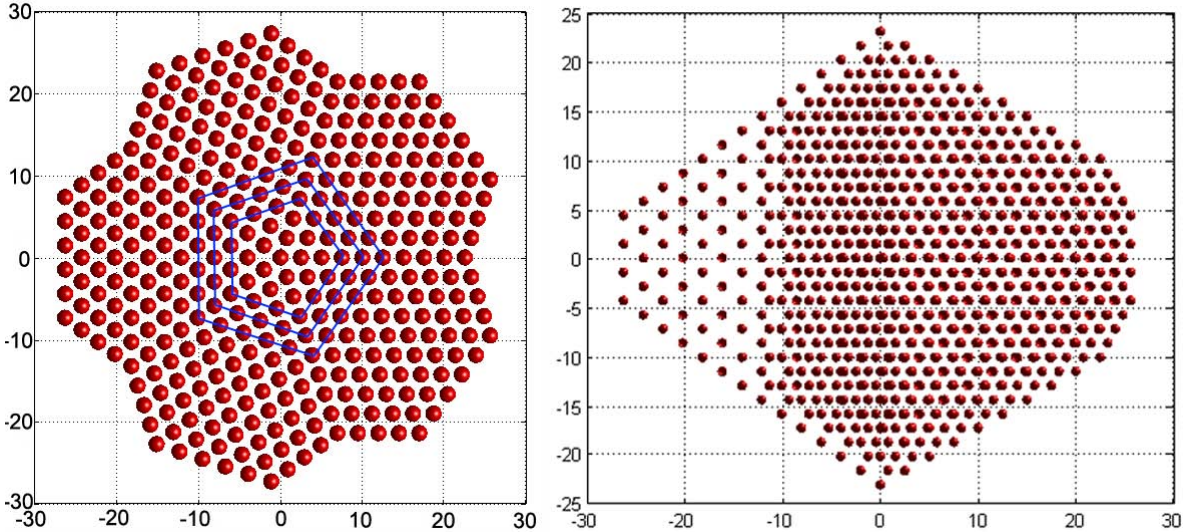


Figure 6.2: The model of Marks-Decahedron used for simulations. View along the five-fold symmetry axis (left) and profile view (right). The shell structure of decahedron is shown with blue lines. The axes are calibrated in Angstroms.

twinned parts. The measurement of interplane spacing and neighboring atomic distances were performed separately for each part and then the result was averaged. The $\{200\}$ plane spacing was measured from the center towards the edges of nanoparticle. One gets $d_{200} = (0.2073 \pm 0.0039)nm$. The lattice parameter is a double of this value $a = (0.4146 \pm 0.0078)nm$. This value is comparable with those for the bulk gold ($a_{bulk} = 0.4078nm$) within the error bar. However one group reported quite opposite results: for $\{220\}$ -planes and $\{422\}$ - planes one observes contraction of lattice for gold nanoparticles in the size range from 30 to 400 Å [41]. In my case the decahedron nanoparticles are oriented mainly along $\langle 110 \rangle$ crystallographic axis. In this orientation named planes are not visible to confirm these results. Moreover the interplane spacing for $\{422\}$ planes is close to the information limit of the microscope and can not be resolved. The average distance between neighboring atomic columns within (200) planes amounts $d = (0.3012 \pm 0.0040)nm$. From here the recalculated lattice parameter equals to $a = (0.4259 \pm 0.0056)nm$, $a = \sqrt{2}d_{neighbor}$. As one can see the lattice is expanded in this direction by 4.4% in comparison with bulk. It corresponds to the results achieved earlier for decahedron nanoparticles. The measurement of plane spacing for outmost layers does not reveal any surface relaxation for gold nanoparticles.

The structure of gold nanoparticles was also analyzed based on image simulations. The atomic model used for simulations is displayed on figure 6.2. For multislice simulations I considered the model of Marks - Decahedron [42]. This structure is typical for small nanoparticles with a diameter less than 50 nm. It has shell structure but differs from the general model of regular Decahedron. In the case of Marks - Decahedron the edges ((100) - facets) as well as pentagon vertices ((111)-facets) are truncated. By ino-type of Decahedron only edges ((100) - facets) are truncated. The following parameters were used for modeling: N = 17 (number of atoms in the central column), M = 13 (number of shells), K = 10 (number of atomic columns on twin boundary). These parameters were chosen based on the experimental image. For simulations the bonding length for the bulk material was used ($d_{bond} = 2.885 \text{ nm}$, [43]). For decahedron structure the bonding length is the distance between atoms in atomic columns through [011] - direction.

Figure 6.3 shows the resultant simulated HRTEM image. In general the simulated image repeats the atomic structure of the model. The positions of bright spots only slightly deviate from the real atomic positions. On the edge of nanoparticle the diffraction fringes due to delocalization can be recognized. But the most striking feature is contrast reversal from the edges to the center of nanoparticle. As it was already discussed in the previous chapter this contrast reversal can originate from the extinction behaviour of the electron wave because of thickness gradient from the center to the edge of the nanoparticle. The experimental HRTEM image of Au nanoparticle shows no contrast reversal [Fig. 6.1]. All atomic columns have almost the same intensity. There can be two possible explanations of this behavior. The nanoparticle can be tilted by a small angle from the zone-axis. The tilting extends the kinematic range of scattering and prevents the contrast reversal for this thickness range (up to 5nm). Another possibility is morphological modification of the nanoparticles. Since the edge and especially corner atoms possess a high energy, it is reasonable to assume that decahedral nanoparticles are truncated along [011] direction. The last idea was carefully examined in the framework of my diploma work.

Following this idea the initial model of Marks - decahedron was modified. From the sharp bottom and top parts of decahedron (011) - planes were removed. The model is

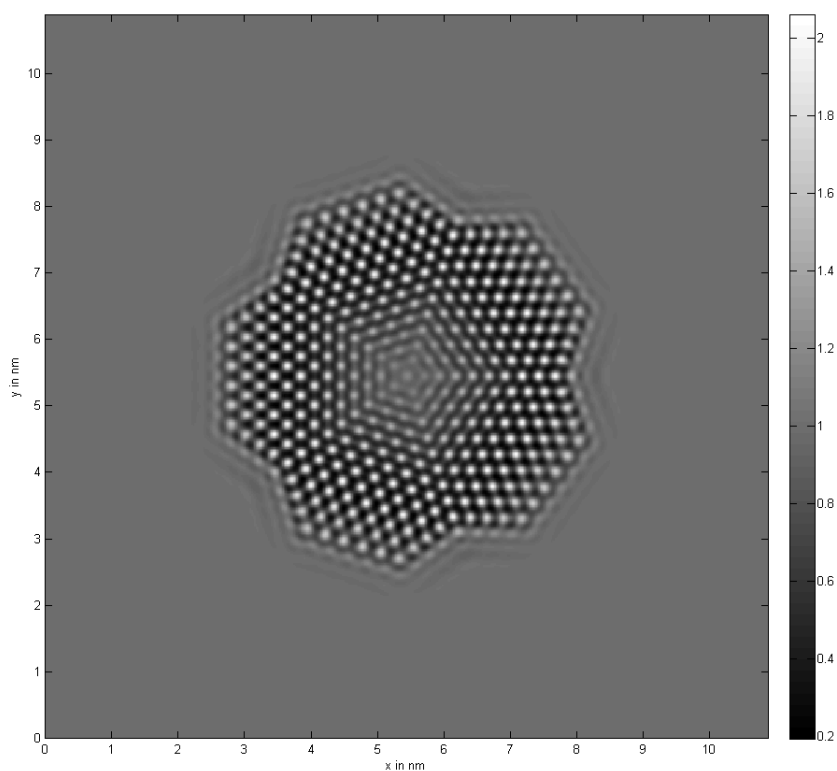


Figure 6.3: Simulated high resolution TEM image of a decahedral Au nanoparticle. The optimum defocus value was estimated through simulated focal-series giving the best coincidence with the experimental image.

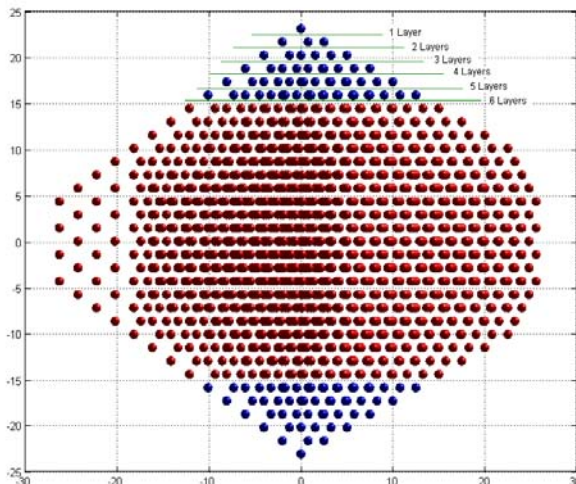


Figure 6.4: Truncation of decahedron along $[011]$ - direction.

illustrated in figure 6.4. The simulations with different degree of truncations (number of truncated planes) were performed. Afterwards the contrast of the simulated images was compared with the contrast of experimental image. For qualitative analysis the intensities of atomic columns were averaged over each shell. The corresponding graphs are shown on the figure 6.5.

Figure 6.5 shows simulated images and also atomic column intensity analysis. The images were simulated for the decahedral particle with a different number of truncated planes. The experimental image with the corresponding intensity analysis is also shown. Intensity of atomic columns of the experimental image (Fig. 6.5a) are nearly the same for inner 11 shells and rapidly drops for the outmost five layers. For the regular decahedron one can observe completely different behavior (Fig. 6.5b). The intensities of inner shells drop down. The contrast of the central column is even lower than that of the nanoparticle edge. The best coincidence can be achieved when 7 layers in the model are truncated (Fig. 6.5c). In this case the theoretical dependence qualitatively repeat the experimental one. Also another interesting point should be underlined. The intensity profile of the simulated image close to the nanoparticle edge does not repeat experimental one. The experimental profile looks more curved in contrast to the theoretical dependence. It can be explained by larger thickness gradient. In theoretical model the thickness of particle decreases layerwise from the

core to the edge by one atom. It seems that for outmost layers this dependence is not fulfilled.

The degree of truncation can be quantitatively estimated in the following way. The icosahedron-type of decahedron can be imaginary divided into three parts: top and bottom pentagonal pyramids and the middle flat section (see fig. 6.10). Since truncation is applied only to pyramids the degree of truncation R equals to the ratio of total number of $\{110\}$ planes and the number of cut off planes. For completely truncated decahedron R is equal to 1. For big nanoparticles the number of planes can be replaced by the thickness. For the current model $R = \frac{7}{13} \cdot 100\% \approx 54\%$.

From the physical point of view the truncation to $[110]$ - direction seems to be quite unusual. The morphology of nanoparticle is defined by crystallographic facets. Moreover the appearance of different facets is determined by their surface energies. For face-centered-cubic (fcc) structure following sequence is hold: $\gamma_{111} < \gamma_{100} < \gamma_{110}$, [44]. It means that $\{110\}$ surface possesses the highest surface energy in comparison with $\{111\}$ and $\{100\}$ surfaces and appears very rarely in crystals. However in the case of Au nanoparticles one observes completely different behavior. More systematic studies together with molecular dynamical simulations are required to verify these results.

In order to confirm this idea about truncated decahedrons I have also investigated the reconstructed phase image by using linescans. The phase and amplitude images are shown in the figure 6.6 and also corresponding linescans in the figure 6.7. The linescans were made along $\{200\}$ (linescans 1,3 Fig. 6.6) and $\{111\}$ (linescan 2 Fig. 6.6) planes. If one considers theoretical model without truncation then for linescan 1 and 3 the difference between maxima of phase should correspond to 2 atoms. For linescan 2 this difference is 1 atom. Surprisingly linear dependence is observed for 5 (linescan 1) and 6 (linescan 2 and 3) outmost shells. Close to the center of nanoparticle this dependence is either constant (linescan 2) or falls down (linescan 1 and 3). From here one can make conclusion that the central flat region exhibits strong roughness due to small size of nanoparticle. I also want to pay attention on one interesting detail. Figure 6.7 shows the deviations of phase maxima from the regression line. The deviations of some maxima have different sign but almost the same magnitude. This behavior can be explained by atom „deficiency“ or „redundancy“ in

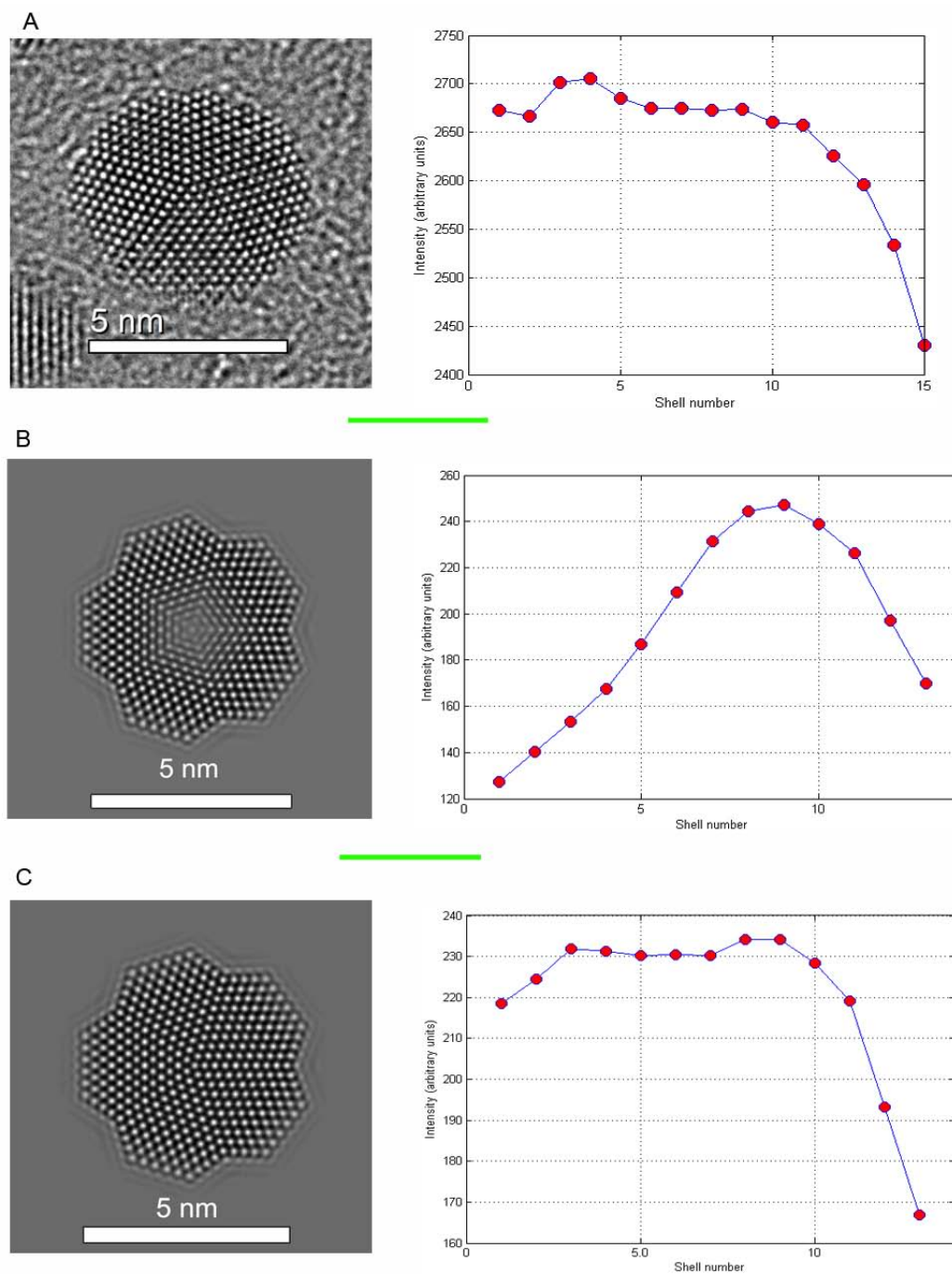


Figure 6.5: Intensity profiles of experimental and simulated images averaged over the shells of decahedron Au nanoparticle. The intensities of atomic columns were calculated as maxima of fitting function. The averaged intensity is plotted against the shell number. Shell number 1 corresponds to the central atomic column. Experimental image with averaged intensity profile (A). The simulated image for regular decahedron with corresponding intensity profile (B). The simulated image for decahedron with 7 truncated (110) layers from top and bottom (C).

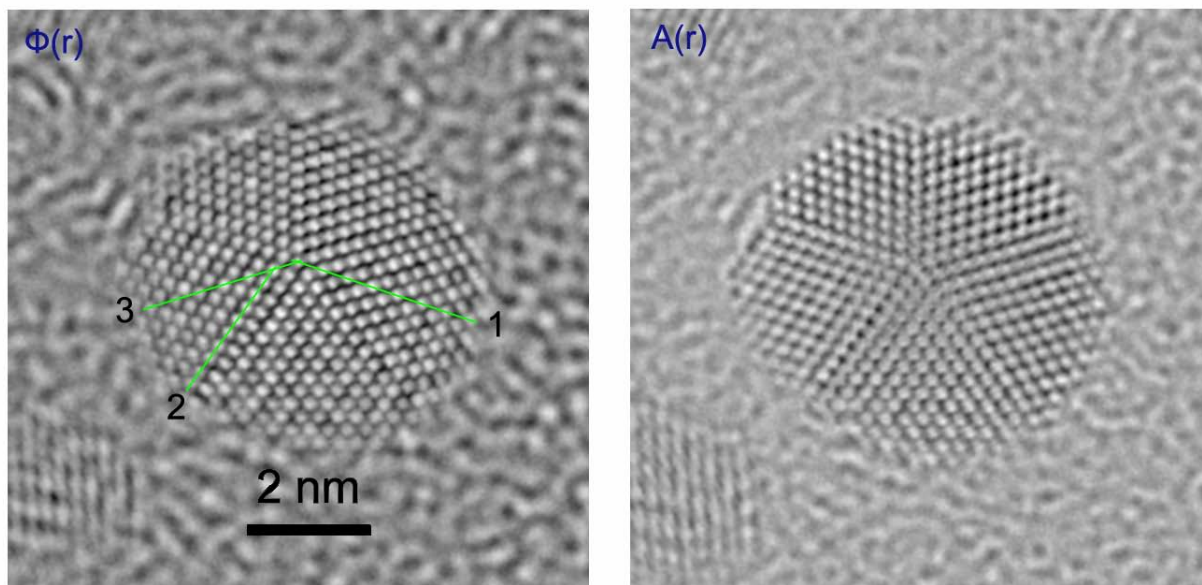


Figure 6.6: Phase (left) and amplitude (right) images of reconstructed wave-function from ser-37. Linescans are shown with colored lines.

atomic columns. It should develop into additional roughness of $\{111\}$ - facets. However the error in phase estimated from amorphous background ($\approx 50\text{mrad}$) allows only speculate about this fact.

6.2 Tilting experiments with gold nanoparticles

Since the majority of decahedron nanoparticles were oriented with five-fold symmetry axis perpendicular to the substrate the best way to check if some $\{110\}$ planes are absent or not is to make tilting experiments or better tomography. Tilting experiments with small nanoparticles is a complicated task since they are quite mobile and can be damage by long electron irradiation.

Multitwinned nanoparticles with icosahedron and decahedron shapes are the most intensively studied nanoparticles. The structure of decahedron nanoparticles was studied for a broad range of sizes: from 30 nm up to several micrometers [45]. Most of them has a regular structure without any truncation. For small nanoparticles with a diameter less than $\leq 20\text{ nm}$ the truncation becomes more apparent. Several types of structures as Ino-, Marks- and Star decahedron can be recognized. Also rounded

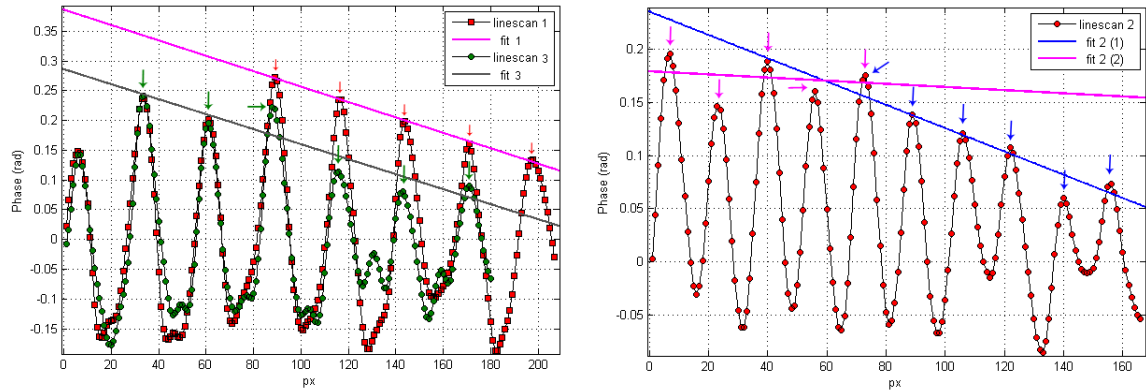


Figure 6.7: To analysis of linescans of phase image from ser-37. The width of linescan was equal 10 px. Linear fitting is shown with solid colored lines. Maxima of contrast used for fitting are indicated with arrows. Maxima correspond to the bright spots on phase image. Intermediate maxima arise from the integration of intensities over the linescan width. Some neighboring atomic columns can contribute into calculation.

form of decahedron appears quite frequently. At this point the following idea was proposed. If this new type of truncation described above relates to the size effect or not.

Two different types of solutions with Au nanoparticles were prepared. (see „Experimental techniques“). Afterwards the samples M184 and M150 were prepared. The nanoparticles from the solution M184 have a size from 10 up to 20 nm. In order to estimate the degree of truncation tilting experiments were carried out. Figure 6.8 shows a series of images of one nanoparticle acquired at different tilting angles. The truncated plate-like shape of a decahedron is observed. The degree of truncation R was estimated to be 0.34. This value is lower than that for smaller nanoparticles.

The results of tilting experiment on the larger particles (solution M150) are displayed on figure 6.9. In the first image by tilting angle of 15° the pentagonal shape of nanoparticle can be seen. One of the facets in the second image (-30°) has a dark contrast therefore it is in the Bragg condition. The facet possesses clear triangular shape and that presumes a regular shape of the nanoparticle.

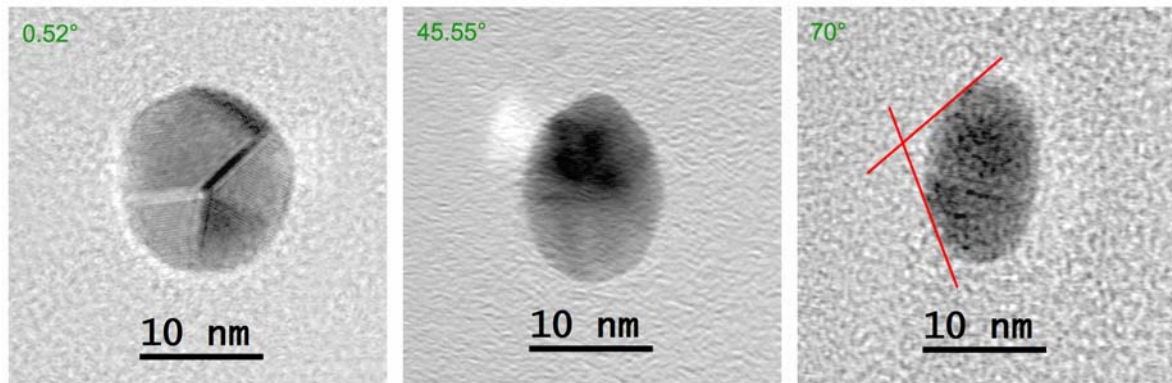


Figure 6.8: Images at some angles from tilting series made on the sample M184. The tilt angle range included both negative and positive values. The tilting was made with tomography holder (tilt angle range: -75° .. 75°). The tilting axis is vertical. The image by 0.52° situates close to the zone axis. The lattice structure for each tetragonal part of decahedron can be recognized. The bright contrast near the nanoparticle on the second picture is „ghost“ reflex due to defocusing. On the third picture the missing „head“ of decahedron is marked with solid red lines.

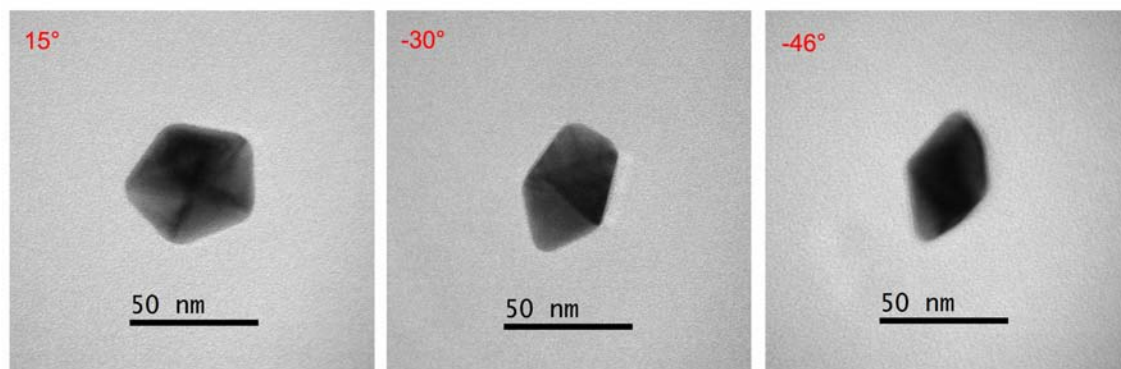


Figure 6.9: Images from a tilting series made on sample M150. The tilting experiment was done at CM12 microscope using standard single-tilt TEM holder. (tilt range: -45° .. 45°)

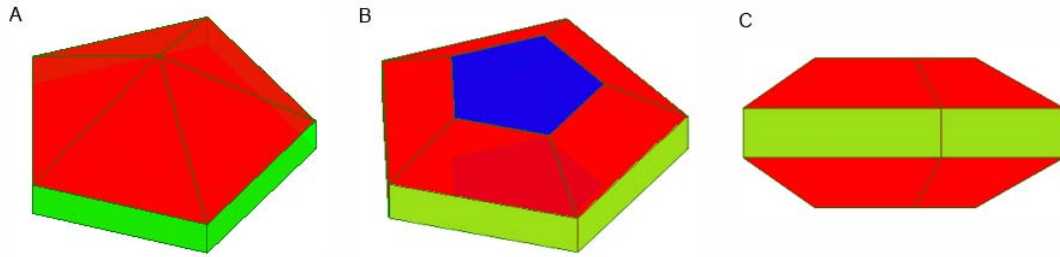


Figure 6.10: Models of icosahedron (A) and Decahedron truncated perpendicular to five-fold symmetry axis (B and C). Green, blue and red planes correspond to the $\{100\}$, $\{110\}$ and $\{111\}$ facets respectively.

6.3 Dynamical structural transformations of gold nanoparticles under electron beam

Figure 6.11 shows the process of aggregation and recrystallization at two Au nanoparticles caused by prolonged exposure to high energy (200 keV) electron beam irradiation in the electron microscope. From the FFT analysis one can conclude that initially the big nanoparticle had a decahedron multitwinned structure. The small neighboring nanoparticle owned some disordered structure and random orientation. Both nanoparticles were observed for approximately 20 minutes. During this time the damage of carbon film happens. The small nanoparticle begin to recrystallize in order to match the crystal lattices. Finally, a large elongated NP of non-regular shape is formed. One can clearly distinguish five twinning planes as a legacy of decahedral structure of the initial nanoparticle. The smaller particle seems to adjust its structure to the more stable decahedral particle.

Another example of a nanoparticles aggregation caused by the electron beam irradiation is shown in figure 6.12. In this case the electron energy was 300 keV. Both nanoparticles are viewed along their symmetry axis. On the first image the small nanoparticle seems to be slightly tilted. Both nanoparticles have irregular decahedral shapes and finally „stick“ together edge-by-edge along $\{100\}$ planes. The distances between the centers of nanoparticles were estimated to be: 7.951 nm (Image A), 8.016 nm (Image B) and 7.206 nm (Image C). The distance between edges of nanoparticles for image 2 is equal to 1.068 nm. Also the number of $\{200\}$ planes

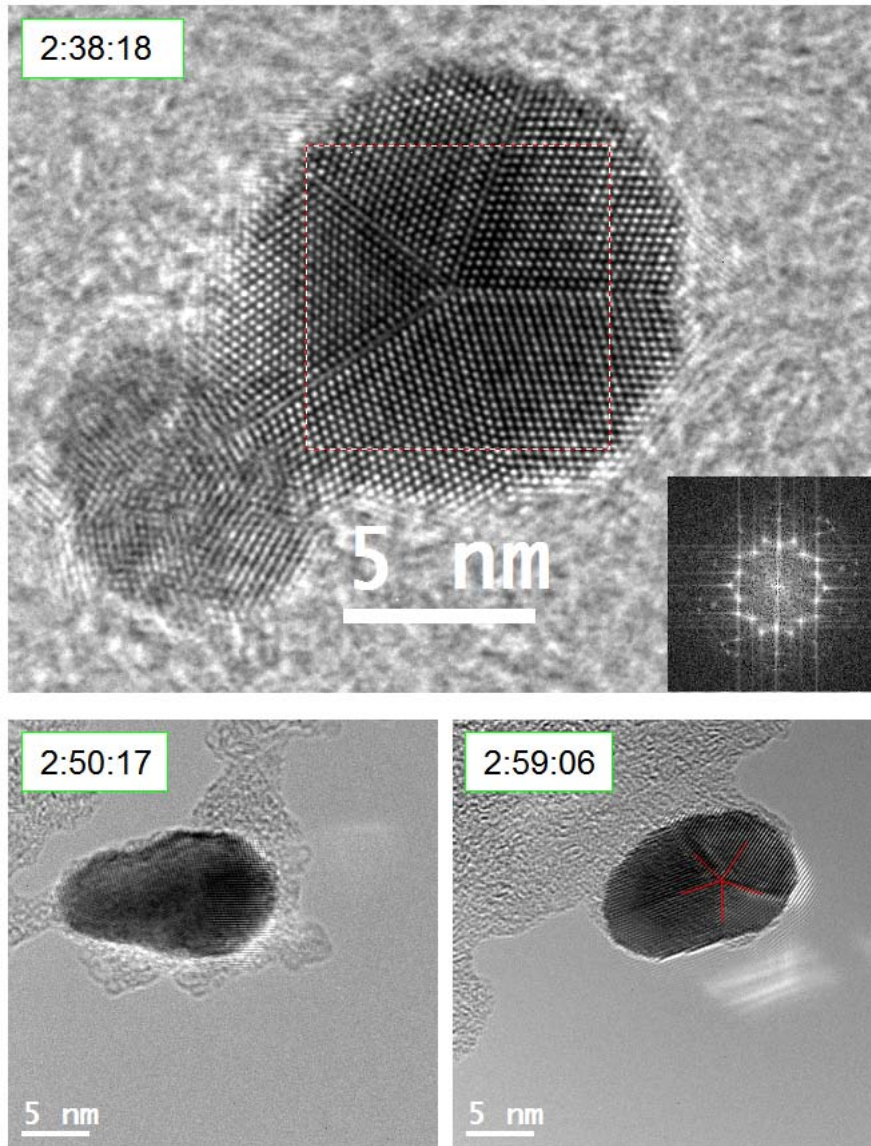


Figure 6.11: Effect of electron irradiation inside TEM on the group of Au nanoparticles. The experiment was done using *Tecnai F20* microscope (the electron energy 200 keV). The inset is FFT of the central area of a big nanoparticle. The acquisition time is shown in the left corner of the images.

perpendicular to the line connecting the centers was calculated. Before collision one has: 10 planes for small nanoparticle and 21 for big one. After collision the overall number of planes equals to 31. After adhesion one can observe big strain resulting from the angle discrepancy between (111) planes of 4.56° . From the calculated values one can conclude that there is no bridge grown between small and big nanoparticles

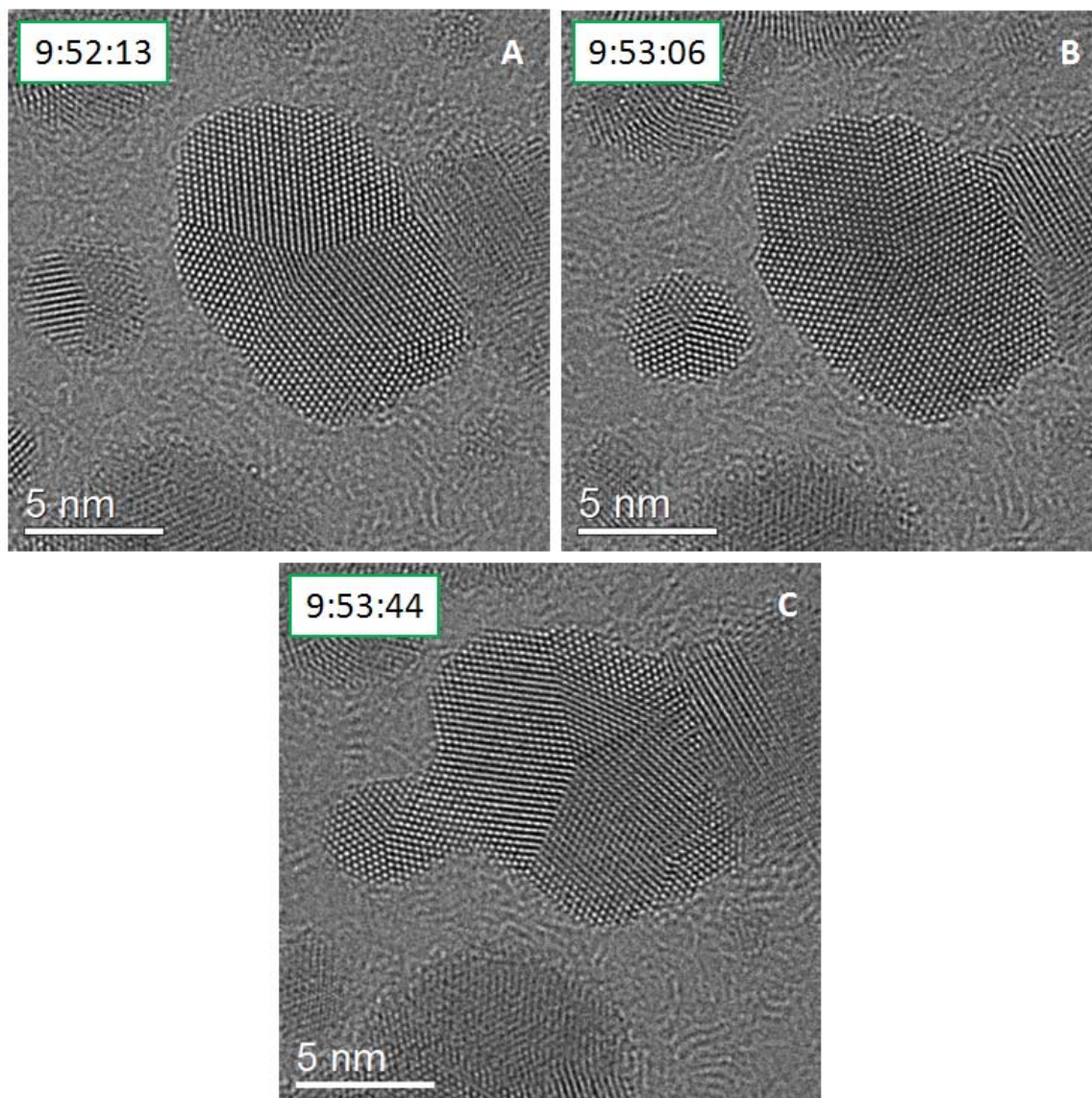


Figure 6.12: The process of „consuming“ of Au nanoparticles inside the TEM. The images were acquired with *Titan 80 – 300 TEM* microscope at different times as indicated in the upper left corner of every image.

due to the diffusion of surface atoms. The nanoparticles are moving to each other during this process. The inelastic strain results in the stretching of outmost layers. So far the reason of this attraction and recrystallization is not clear. For sure the electron beam should somehow contribute to this phenomena. The charge effect due to the electron beam can result only in repulsive interaction between the nanoparticles. Also the reorientation of the small nanoparticle according to the crystal lattice

of the big nanoparticle at some distance of 1-2 nm lives room for guesses. The observed phenomena can be explained from energetic point of view. Most probably the surface energy contribution is very large for Au nanoparticles. Therefore the big nanoparticles are more preferable because of low surface to volume ratio. At the beginning some small nanoparticles can be in metastable state. The electron beam can provide some energy to: 1) move the nanoparticle to each other and 2) to leave them from metastable state towards an energetically lower state (from the private communications with Dr. J.Barthel).

7 Conclusion

In summary, using the exit-wave reconstruction (EWR) method in high-resolution transmission electron microscopy (HRTEM) I investigated the atomic structure of magnetic alloy *FePt* and noble metal *Au* nanoparticles (NPs). The advantage of the EWR method over normal single-shot HRTEM method is that the obtained phase contrast maxima can be directly interpreted as atom column positions, which enable us to study the atomic variations of small particle, especially the atoms at the surface, which otherwise are very difficult to distinguish using single-shot HRTEM image due to the strong delocalization effect. In my diploma work, I used aberration-corrected TEM to carry out HRTEM image acquisition and then used exit-wave reconstruction method to retrieve the phase information of small particles. The hardware aberration-corrected TEM as well as the software aberration-corrected EWR method allows us to investigate the detailed atomic structure with a resolution of $0.8nm$.

To obtain high quality HRTEM images for EWR, I prepared clean TEM samples using plasma to reduce the hydrocarbon contamination. During the high-resolution image acquisition, the stability of the nanoparticle under electron beam irradiation is important. I used special TEM grids with ultrathin supporting carbon film. For the EWR I used the TrueImage package implementing a maximum-likelihood method to iteratively retrieve the exit-wave function using through-focus images. For the detailed structure examination I used the Peak-Pairs Analysis (PPA) to pinpoint the atom columns in phase images of NPs with a sub-pixel precision. After the identification of atom columns the lattice planes were fitted with linear functions in order to measure accurately the lattice plane spacings. By plotting the lattice spacings as a function of atomic planes from outmost plane to inner part of the particles, I evaluated the lattice variations of surface planes of *FePt* and *Au* NPs.

Additionally the image simulations of small particles are carried out to compare qualitatively the experimental results with theoretical structural prediction. I have written special program to construct atomic models of NPs of various types of structures, including cuboctahedral, icosahedral and decahedral. Taking the real experimental environment into account, I built the model of thin carbon film [35] and performed the HRTEM simulations.

The expansion of lattice parameter for $Fe_{45}Pt_{55}$ NPs for outmost layers is confirmed. As was observed in [40] for NPs with cuboctahedral shape expansion happens presumably only for first surface layer. The fitting of lattice relaxation with exponential function as in [32] did not give any good match. It can be explained with strong chemical disorder close to the surface. Besides $\{111\}$ and $\{100\}$ facets show the same value of surface relaxation. The overall expansion of lattice parameter achieves 4.4% in comparison with bulk. However this value is definitely higher as those measured by N. Friedenberger [28] for gas-phase prepared nanoparticles.

Additionally for verification of results image simulations were carried out. The parameters of simulations were taken from experimental conditions. Further the simulated phase image was thoroughly compared with experimental one. The comparison shows the mismatch up to 2.8% between measured interplane distances with theoretical values. This disparity can be explained by background signal from amorphous carbon. Furthermore the simulations were performed for untilted and by small angles tilted nanoparticles. It was shown that the tilting decreases the Z-contrast of phase image.

The structure of small decahedral *Au* nanoparticles was analyzed by means of EWR and image simulations. The analysis of contrast shows that the nanoparticles should be truncated perpendicular to five-fold symmetry axis. Consequently it results in appearance of additional $\{110\}$ crystallographic facets. It is unusual since for fcc-structure the mentioned planes possess the highest surface energy. In addition the tilting experiments were carried out on nanoparticles of different sizes. Most probably one deals with size effect since for bigger nanoparticles the truncation becomes smaller. In any case for consistent answer the energy of different atomic configurations should be compared by molecular dynamics simulations.

Also the structural transformations of *Au* nanoparticles under electron beam were presented. The origin of observed phenomena is so far unclear. More systematic studies with controlled parameters are required.

A Appendix

A.1 Generator - software

On the figure A.1 one can see graphical interface of Generator software. In this section I'm going to explain how to build different particles of different morphologies and also meaning of different parameters. First of all you need to choose the morphology of particle. On the panel „Model“ one can find list of different possibilities. So far it's possible to built model of Mackay-Icosahedron, Mackay-Icosahedron with core-shell structure, regular Decahedron, Ino-Decahedron, Marks-Decahedron and Cuboctahedron particles. These are common morphologies which can be observed in HRTEM studies of metallic nanoparticles. However new structures will be added in future.

After selecting the structure of interest you need to set some parameters of this model. For Icosahedron only one parameter N is available. Since Mackay-Icosahedron has layer structure, N is number of layers surrounding the central atom which situates in the origin of coordinate system. For Icosahedron with core-shell structure there are two different parameters. The first parameter N is still number of shells of the particle. The second parameter M is a number of outmost layers contributing to the shell of the particle. The right-hand standing parameter in Generator has always priority to left-hand standing parameter. So non-realistic situations like number of outmost layers bigger than overall number of layers in the particle are avoided. The regular Decahedron is also characterized only with one parameter. This parameter correspond to the number of atoms in the central atomic column which is congruent with five-fold symmetry axis of the Decahedron. One can build Ino-Decahedron from the Decahedron by truncating the edges with planes perpendicular to $\langle 200 \rangle$ - directions of the particle. So that's why the second parameter of this structure

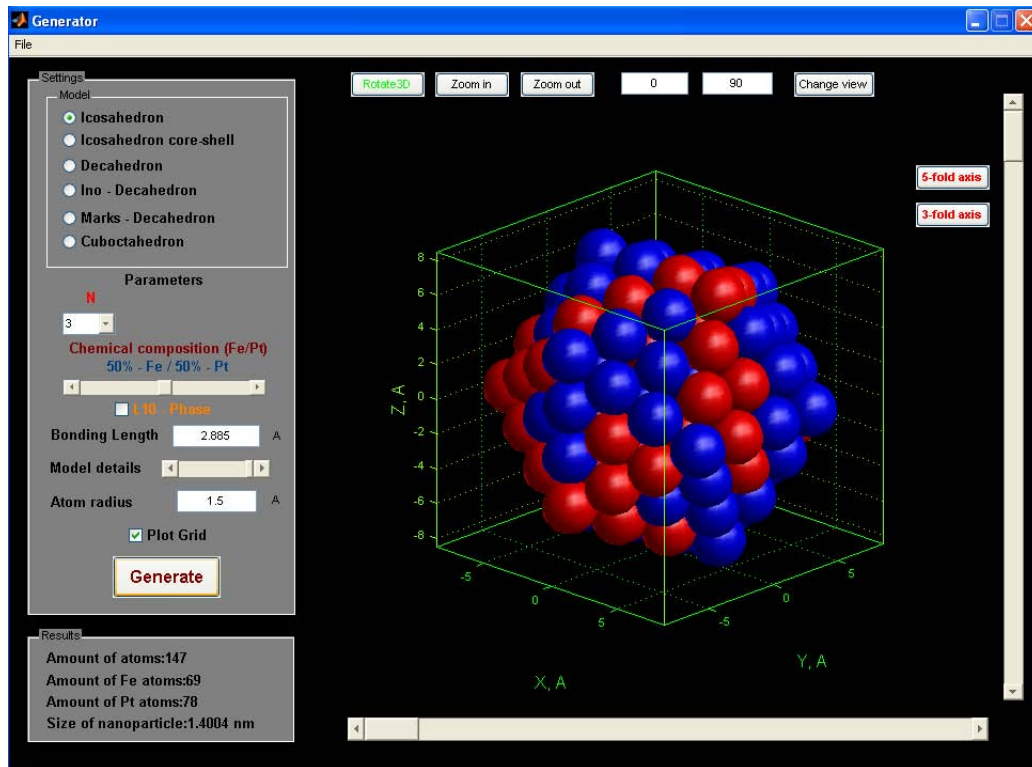


Figure A.1: Screenshot of Generator - software with model of Icosahedron particle

equals to the number of $\{200\}$ - planes along the $\langle 200 \rangle$ - directions of the particle. In this program it's even possible to create so called „nanorods“ with decahedral five-fold symmetry. In this case the first parameter of Ino-Decahedron should be much bigger than the second one. The Marks-Decahedron has more complicated structure than Ino-type. In this structure $\{200\}$ - planes as well as $\{111\}$ - planes near the vertices are truncated. For building of this structure I have introduced the third parameter which is equal to the number of atomic columns along twin boundary of the particle. The Cuboctahedron model has two different parameters. The first parameter is number of unit cells of fcc-cluster along three reciprocal perpendicular directions commensurate with the lattice parameter. The second parameter governs the truncation of the fcc-cluster by planes perpendicular to the $\langle 111 \rangle$ equivalent crystallographic directions.

After setting some parameters it's possible to set relative composition of two different species in the particle. You can change the relative composition by dragging corresponding slider. So far it's possible to choose only between two different

chemical elements: iron and platina. In the future version of Generator I consider the possibility to include the multiple choice between several kinds of atoms. Different atoms in the final model are represented with different colors. By selecting „L10-phase“ checkbox the program generates the particle in L10-phase. The particle in L10-phase consists of alternating layers of two different elements. The „bonding length“ parameter is the distance between neighboring atoms in the particle. In the case of Icosahedron and Decahedron structures it's the distance between atoms in the atomic column corresponding to the axis of 5-fold symmetry. The parameter „Model details“ sets number of polygons used for rendering of atoms represented with spheres. The meaning of other parameters is clear from their titles.

In „Results“ - section the program calculates the whole number of atoms (so called magic number), number of iron and platina atoms and also approximate size of the structure. After visualisation of the particle it's possible to rotate it and view along different directions. For fine tilting of the particle one can use corresponding sliders. The horizontal slider changes azimuth angle and vertical slider the polar angle of the view. The tilting angle step is equal to 0.5° .

After generating of structure it's possible to save atomic coordinates in file. Following formats are available:

1. *.msi for cerius2 simulation package,
2. *.cfg for QSTEM simulation software and also AtomEye atomistic configuration viewer,
3. *.txt saves type of element and three vectors with atomic coordinates.

The program was written and compiled as stand-alone application in MATLAB 7.1. However in order to run it one needs to install MATLAB Component Runtime Library MCRInstaller.exe. On the pictures below one can see the particles of different morphologies built by Generator.

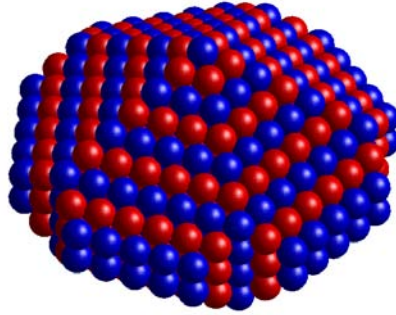


Figure A.2: „Onion“ -structure of Marks-Decahedron in L10-phase

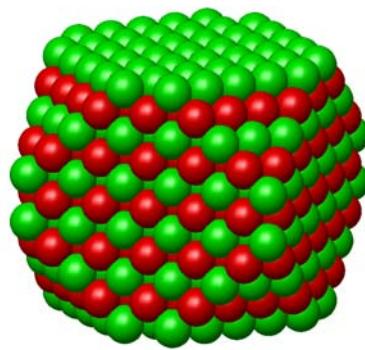


Figure A.3: Cuboctahedron in L10-phase

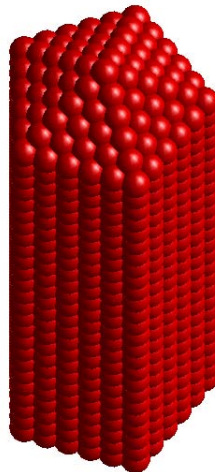


Figure A.4: Nanorod with five-fold symmetry as particular case of Ino-Decahedron structure

A.2 cfg - format

The example of cfg - data file with short description of parameters is given in the figure A.5.

```

Number of particles =25329 ← number of atoms in supercell
Å = 1.0 Angstrom (basic length-scale) ← the unit of the length for basic vectors of supercell
HO(1,1) = 92.8018 Å
HO(1,2) = 0 Å
HO(1,3) = 0 Å
HO(2,1) = 0 Å
HO(2,2) = 92.8018 Å
HO(2,3) = 0 Å
HO(3,1) = 0 Å
HO(3,2) = 0 Å
HO(3,3) = 92.8018 Å

.NO_VELOCITY. ← we do not make any molecular dynamics simulations with this config
entry_count = 3 ← number of information elements for each atom, 3 if one defines only coordinates,
4 if one includes Debye-Waller Factor, 5 and 6 if one includes occupancy and the ionic charge

55.8 ← atomic mass of the element
Fe ← symbol of the element (do not make any mistake here!)
0.4714 0.4304 0.4513
0.4857 0.4506 0.4371 ← X,Y and Z coordinates of the atom

195.084
Pt
0.5000 0.4708 0.4228
0.5000 0.5111 0.4228

12.011
C
0.0108 0.0134 0.1145
0.0249 0.0179 0.1294

```

Figure A.5: cfg - format

Important note: before writing the data into this format atomic coordinates should be normalized on dimension of supercell!

A.3 Microscope Titan 80-300 TEM

Titan 80-300 TEM is field-emission gun microscope equipped with spherical aberration corrector for objective lens and also post column energy filter. The whole column of the microscope and also holder section is protected with special cover to prevent thermal influences. The microscope is equipped with Gatan 2k slow-scan CCD for image acquisition.

Parameter	Quantity
Acceleration voltage U	300kV
Wavelength of electrons λ	1.96876 pm
Information limit $\rho = \frac{1}{g_{max}}$	80 pm
Semiconvergence angle a	0.2 mrad
Defocus spread D	2.44/2.92nm*
Chromatic aberration C_c	1.28 mm
Optimum spherical aberration $C_{s,opt}$	-12.7233 μ m
Lichte defocus Z_{opt}	5.78 nm
Delocalisation R	47.4 pm

Table A.1: General Instrumental and Calculation Parameters for Titan 80-300 TEM (* - these value were estimated by using two different software packages)

A.4 Microscope Tecnai F20 Supertwin

Parameter	Quantity
Acceleration voltage U	flexible 120 - 200kV
Wavelength of electrons λ	2.50793 pm
Information limit $\rho = \frac{1}{g_{max}}$	90 pm
HRTEM:Point resolution	0.23 nm
HRTEM:line resolution	0.11 nm
HAADF-STEM:point resolution	0.18 nm
Semiconvergence angle a	0.15 mrad
Chromatic aberration C_c	1.2 mm
Spherical aberration C_s	1.2mm

Table A.2: General Instrumental and Calculation Parameters for Tecnai F20 Supertwin

Tecnai F20 Supertwin microscope is Windows 2000/XP operated. The data transfer is accomplished through FireWire. The microscope is equipped with schottky

FEG with high beam current. With tomography holder it's possible to achieve high ranges of tilting angles up to 75° degrees. The microscope can operate in HRTEM as well as HAADF-STEM mode. The microscope is also equipped with EDX and EELS systems for analytical measurements. In the table A.2 some main characteristics of this microscope are listed.

Bibliography

- [1] Andreas Thust: *Theory and applications of focal-series reconstruction in HRTEM*. Microscopy and Microanalysis **11**, 602-603 (2005).
- [2] Yanyun Ma, Jie Zeng, Weiyang Li, Maureen McKiernan, Xie Zhaoxiong, and Younan Xia: *Seed-mediated synthesis of truncated gold decahedrons with a AuCl/Oleylamine complex as precursor*. Advanced materials **22**, 1-5 (2010).
- [3] Rajesh Sarder, Alison M. Funston, Paul Mulvaney, and Royce W. Murray: *Gold nanoparticles: past, present and future*. Langmuir **25(24)**, 13840-13851 (2009).
- [4] Marek Grzelczak, Jorge Perez-Juste, Paul Mulvaney, and Luis M.Liz-Marzan: *Shape control in gold nanoparticle synthesis*. Chemical Society Reviews **37**, 1783-1791 (2008).
- [5] David B. Williams and C. Barry Carter: *Transmission Electron Microscopy*. Plenum Press, (1996).
- [6] F. Ernst and Manfred Rühle: *High-resolution imaging and spectrometry of materials*. Springer-Verlag, Berlin Heidelberg, (2003).
- [7] P.W. Hawkes and E. Kasper: *Principles of electron optics*. Academic Press, (1989).
- [8] Edington Jeffrey William: *Practical electron microscopy in material science*. TechBooks, (1991).
- [9] J. Barthel: *Measuring aberrations and assessing resolution*. Advanced Electron Microscopy School, Copenhagen (2009).
- [10] CTF Explorer, URL: www.maxsidorov.com/ctfexplorer/.

-
- [11] ElmiX: Electron microscopy software for data analysis and education, URL: www.elmix.org .
- [12] K. Urban: *Hochauflösende Elektronenmikroskopie*. Phys. Blätter. 46, Nr 3, P. 77-84 (1990).
- [13] M.A. O'Keefe: *Interpretation of HRTEM images by image simulations: an introduction to theory and practice*. MSA Tutorial III47-50 (1994).
- [14] Markus Lentzen: *Progress in aberration-corrected high-resolution transmission electron microscopy using hardware aberration correction*. Microscopy and Microanalysis **12**, 191-205 (2006).
- [15] Corrected electron optical systems GmbH, URL: www.ceos-gmbh.de .
- [16] F. Thon: Z. Naturforschung **21a**, 476 (1966).
- [17] J.M. Cowley and A.F. Moodie: *The scattering of electrons by atoms and crystals. A new theoretical approach..* Acta Cryst. (1957).
- [18] P. Goodman and A.F. Moodie: *Numerical evaluation of N-beam wave functions in electron scattering by the multislice method..* Acta Cryst. (1974).
- [19] Earl J. Kirkland: *Image Simulation in Transmission Electron Microscopy*. Applied and Engineering Physics, Cornell University (2006).
- [20] Min Chen, Jaemin Kim, J.P. Liu, Hongyou Fan, and Shouheng Sun: *Synthesis of FePt nanocubes and their oriented self-assembly*. JACS Communications **128**, 7132-7133 (2006).
- [21] Nikhil R. Jana, Latha Gearheart, and Catherine J. Murphy: *Wet chemical synthesis of high aspect ratio cylindrical gold nanorods*. J. Phys. Chem. B **105**, 4065-4067 (2001).
- [22] Daeha Seo, Choong Il Yoo, Im Sik Chung, Seung Min Park, Seol Ryu, and Hyun-joon Song: *Shape adjustment between multiply twinned and single-crystalline polyhedral gold nanocrystals: decahedra, icosahedra and truncated tetrahedra*. J. Phys. Chem. C **112**, 2469-2475 (2008).

- [23] 38th IFF Spring School 2007: *Probing the nanoworld - microscopies, scattering and spectroscopies of the solid state*. Forschungszentrum Jülich, (2007).
- [24] Pedro L. Galindo, Slawomir Kret, and Ana M. Sanchez: *The Peak Pairs Algorithm for strain mapping from HRTEM images*. Ultramicroscopy **107**, 1186-1193 (2007).
- [25] A. L. Mackay: *A dense non-crystallographic packing of equal spheres*. Acta Crystallographica **15**, 916-918 (1962).
- [26] X. Wu, W. Cai, and X. Shao: *A dynamic lattice searching method with rotation operation for optimization of large clusters*. Chemical Physics **363**, 72-77 (2009).
- [27] Quantitative TEM and STEM Simulations, URL: <http://www.mf.mpg.de/en/organisation/hsm/koch/stem> .
- [28] Nina Friendenberger: *Layer resolved lattice relaxation in magnetic FePt_{1-x} nanoparticles*. Diplomarbeit, Department of physics, university Duisburg-Essen (2007).
- [29] Phillipe-Andre Buffat: *Identification of nano-phases: relative merit of local analysis techniques*. 1st Stanislaw Gorczyca Summer School on Advanced Transmission Electron Microscopy, Krakow (2003).
- [30] J.A. Ascencio, C. Gutierrez-Wing, M.E. Espinosa, M Marin, S Tehuacanero, C. Zorrilla, and M. Jose-Yacamán: *Structure determination of small nanoparticles by HREM imaging: theory and experiment*. Surface Science **396**, 349-368 (1998).
- [31] M. Jose Yacamán, R. Herrera, S Tehuacanero, A Gomez, and L. Beltran Del Rio: *Surface roughness studies in small particles using HREM*. Ultramicroscopy **33**, 133-141 (1990).
- [32] R.M. Wang, O. Dmietrieva, M. Farle, G. Dumpich, H.Q. Ye, H. Poppa, R. Kilbas, and C. Kisielowski: *Layer resolved structural relaxation at the surface of magnetic FePt icosahedral nanoparticles*. Physical review letters **100**, 017205 (2008).

-
- [33] R. Theissmann: *Private discussions*. (2010).
- [34] M. Grüner: *Private discussions*. (2009).
- [35] K. Du, F. Ernst, M.C. Pelsozy, J. Barthel, and K. Tillmann: *Expansion of interatomic distances in platinum catalyst nanoparticles*. *Acta Materialia* **58**, (2009).
- [36] Welcome to the world of carbon: the allotropes of carbon, URL: <http://invsee.asu.edu> .
- [37] Z.L. Wang, R.P. Gao, B. Nikoobacht, and M.A. El-Sayed: *Surface reconstruction of unstable 100 surface in gold nanorods*. *J. Phys. Chem. B* **104**, 5417-5420 (2000).
- [38] Michael Engel: *Volle Packung*. *Physik Journal* **9 Jahrgang**, (Juli 2010).
- [39] Craig L. Johnson, Etienne Snoeck, Manex Ezcurdia, Benito Rodríguez-González, Isabel Pastoriza-Santos, Luis M. Liz-Marzán, and Martin J. Hÿtch: *Effects of elastic anisotropy on strain distributions in decahedral gold nanoparticles*. *Letters* **7**, 120-124 (2008).
- [40] O. Dmtrieva: *Strukturelle und magnetische Eigenschaften von FePt-Nanopartikeln aus der Gasphase*. Dissertation, Fachbereich Physik, Universität Duisburg-Essen, (2007).
- [41] C. Solliard and M. Flueli: *Surface stress and size effect on the lattice parameter in small particles of gold and platinum*. *Surface Science* **156**, 487-494 (1985).
- [42] The group of Prof. Jian-Min Zuo: *Modeling of icosahedron and decahedron particles*. University of Illinois at Urbana Champaign.
- [43] Ch. Kittel: *Einführung in die Festkörperphysik*. Oldenbourg Verlag München, 14 Auflage, (2005).
- [44] Z.L. Wang: *Transmission Electron Microscopy of shape controlled nanocrystals and their assemblies*. *J. Phys. Chem. B* **104**, 1153-1175 (2000).

-
- [45] Alvaro Mayoral, Hector Barron, Ruben Estrada-Salas, Alma Vazquez-Duran, and Miguel Jose-Yacaman: *Nanoparticle stability from the nano to the meso interval*. *Nanoscale* **2**, 335-342 (2010).

Acknowledgements

I appreciate all people who supported me during my diploma work.

First of all I want to thank my supervisor Herr M. Farle for very interesting themas and giving me the possibility to work in his group.

For learning how to operate microscope and hours spent in discussions of achieved results my special thank is dedicated to Dr. Zi-An Li.

I'm especially grateful to Dr. M. Spasova for guiding during my diploma work and a lot of helpful advices.

I want to thank M. Comesana-Hermo for solution preparation and nice talks in the office.

For technical assistance by operating the microscope in FZ Jülich with posterior discussions of results I want to thank Dr. K. Tillmann, Dr. J. Barthel, Dr. Lothar Houben and M. Heidelmann.

I want to thank M. Grüner for ideas about modeling of nanoparticles.

I'm also very grateful to H. Zähres and R. Theissmann for technical advises and some interesting ideas.

Most of all I want to thank my parents who made my study in Germany possible.

Declaration

I assure that I composed this work independently and did not use any other assistants as only presented here.

Duisburg, 2.08.2010